# State-space model building and validation by comparison with non-linear models and performing SSA

## Universitat Politécnica de Catalunya

July 3, 2023

**Author:** Zongshang Li
**Director:** Eduardo Prieto Araujo
**Co-director:** Onur Alican

ETSEIB
Escola Tècnica Superior
d'Enginyeria Industrial de Barcelona

# Abstract

The level of penetration of renewables and power electronics in the grid is increasing, and in the future, it may even be possible to have a 100 % converter-based transmission system[1]. In such a future, methods for analyzing the stability of the grid with high penetration of power electronics and renewable energy sources are essential. However, due to the increased penetration of power electronics in power systems and the instability of renewable energy sources, the stability analysis of power systems can be very complex. In this paper, GFOL(Grid following system) and GFOR(Grid forming system) are modeled and verified using the state-space equation, and then the stability of the system is analyzed based on the data from the matrix of the state-space equation.

This thesis first describes the working principles, advantages and disadvantages, key components, and key technologies of GFOL(Grid following system) and GFOR(Grid forming system). The system components are described and modeled. Control schemes are described, the basic necessary control modules are detailed and simulation results are provided to illustrate the control methods described.

This thesis then investigates the application of state-space modeling to the modeling of circuits and control elements. The linearisation of non-linear equations is introduced and the state-space equation of state models for GFOL and GFOR are constructed and validated using small signal disturbance analysis.

Finally, the stability of the GFOR and GFOL systems was assessed and analyzed through indicators such as eigenvalues and participation coefficients. This paper provides a simple and reliable example for analyzing the stability of modern power systems by modeling, verifying, and analysing the state-space equations of power systems.

# Contents

# List of Figures

# 1 Introduction

## 1.1 Background and Motivation

Today's environment is facing the global challenge of energy evolution, as developed and emerging countries need more energy to drive their economic growth, while energy resources are limited and unevenly distributed. At the same time, climate change due to greenhouse gas emissions is driving every country to prefer more climate-friendly renewable energy sources, such as hydro, solar, or wind [5].

Power electronics are an enabling technology for converting conventional power systems into smart grids because they can control bus voltage within milliseconds. In particular, alternating current-direct current(AC-DC) converters with bi-directional power capability are a key factor for microgrids and distributed generation systems [6]. Variable-speed wind turbines of different configurations require a power converter architecture based on two AC-DC converters. Each converter requires active and reactive power control capabilities to extract the optimal power from the wind turbine while exchanging the appropriate reactive power with the grid. Similarly, a photovoltaic system requires an AC-DC converter to inject the generated power into the grid. Battery-based storage systems also require bidirectional AC-DC converters to charge batteries or inject power into the grid. A variety of converter typologies exist to connect renewable energy generation or microgrid units to the main grid [7].

The use of related power electronic inverters is usually divided into two types, as shown in Fig. 1 : (a) grid-following type (GFOL) and (b) grid-forming type (GFOR). The grid-forming type inverter controls the voltage on the AC side to help form a voltage source grid. It synchronizes with the rest of the grid through frequency drop control (e.g. P-$\omega$ drop, VSM, dVOC, etc), which is similar to the control of synchronous generators [8]. In contrast, a grid-following inverter controls the AC-side current and follows the phase angle of the existing grid voltage through a phase-locked loop (PLL) [9]. Grid-following inverters have been widely used to integrate wind and solar energy into the grid due to their simple control structure, proven phase-locked-loop technology, and the characteristic of operating at a prescribed current (matching the maximum power point or dispatch point of the resource). In the grid-following mode, the storage side or generation side operates by inputting and outputting power from the electric utility grid, ensuring energy and power control balance and supporting the grid with a range of ancillary services, such as voltage and frequency control regulation, dispatch services and operational reserve capacity, and other functions depending on load and generation conditions [10]. Ideally, the microgrid is always interconnected with the utility so that any excess energy from the microgrid is sent to the main grid, as well as any energy losses from the microgrid are provided by the utility [11]. However, phase-locked loops have a negative impact on the stability of the system, especially when the grid becomes weaker due to large grid impedance [12]. In recent years, attention has therefore turned to grid-forming inverters because of their synchronous generator-like characteristics and their black-start capability.

Nowadays, with the increasing penetration of renewable energy sources, the requirements for the use and control of power electronic converters in power grids are increasing, as are the requirements for the stability of the grid system for residential and industrial electricity use. This paper presents first state-space representation of electrical circuits and then, linearized state-space models of GFOL and GFOR. Also, performs a small-signal analysis based on the eigenvalue and participation factor approach. In order to study the stability of linear systems,

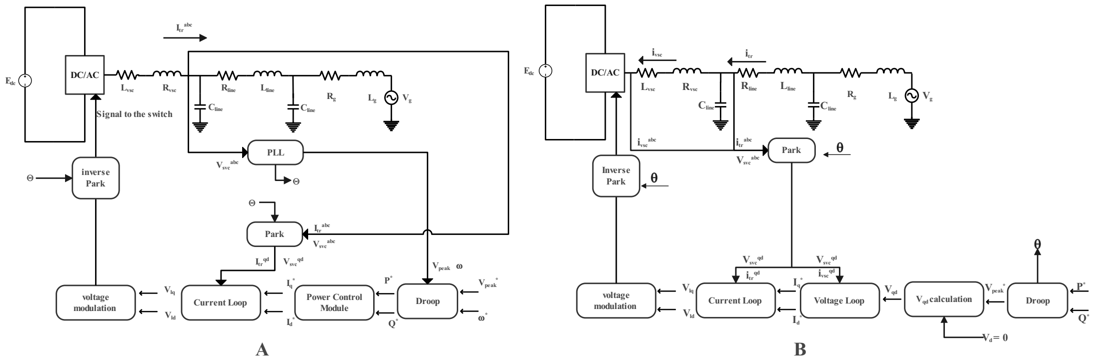

Figure 1: (A)**Grid-following inverter with PLL,** (B)**Grid-forming inverter with frequency droop control**

the eigenvalue evaluation method is the more common approach [13]. For nonlinear systems, this paper uses the method of linearizing them according to the Taylor formula expansion and constructing the state-space equation for their analysis, and this paper also investigates the small signal stability analysis (SSSA) of power electronics. According to [13], state-space modeling and eigenvalue studies are well-established methods for studying the stability of power systems. The main parts of the rest of the paper are summarized as follows.

## 1.2 Objective

- Understanding of the operation, principles, advantages, and disadvantages of GFOL and GFOR. Understanding of key components and key techniques such as PLL, rotation matrix, current control, P, Q control, and droop control and their application in subsequent modeling

- Study the application of state-space equations in modelling of circuits and control elements. Understand and master the linearisation of non-linear equations and evaluate system stability by using eigenvalues and participation factor. Use state-space to build and validate small models such as RL, RLC with PI controller, Thevenin-PI line-varying load, etc.

- Modeling GFOL and GFOR respectively and building state-space equations for them.

- Evaluation and analysis the stability of the system by means of indicators such as eigenvalues and participation coefficients..

## 1.3 Approach

First, each small branch of the system is modeled, then their state-space equations are built, and finally, the results are verified. Systems such as GFOL and GFOR are then modeled. In the modeling process PLL, droop, and current loop control schemes are designed for the system. Then they are modeled and linearized using the state-space equation and the results are verified. All simulations and validations are carried out in the Simulink software.

# 2 Power System Stability

Power system stability can be broadly defined as the property of a power system that allows it to maintain a state of operational equilibrium under normal operating conditions and to regain an acceptable state of equilibrium after a disturbance [2].

The instability of a power system may manifest itself in many different ways, depending on the system configuration and mode of operation. Traditionally, stability issues have been a problem in maintaining synchronous operation. Since power systems rely on synchronous machines to generate electricity, a necessary condition for satisfactory system operation is that all synchronous machines remain synchronized. This aspect of stability is influenced by the dynamic relationship between the rotor angle and the power angle of the generator, as well as by other factors [2].

Instability can be encountered without loss of synchronization. For example, a system consisting of synchronous generators supplying an induction motor load through a transmission line becomes unstable due to a collapse of the load voltage. In this case, maintaining synchronization is not an issue; instead, the concern is voltage stability and control. This form of instability can also occur with loads supplied by large systems covering a wide area [2].

Instability in power systems can take different forms and can be influenced by a variety of factors. Stability can be classified into appropriate categories based on the following considerations [2].

- The physical properties that lead to instability.
- The magnitude of the disturbance under consideration.
- The equipment, process, and time span must be considered in order to determine stability.
- The most appropriate method for calculating and predicting stability.

The specific classification is shown in Fig. 2.

In the assessment of stability, the concern is the behavior of the power system when subjected to transient disturbances. Disturbances may be small or large. Small disturbances in the form of load changes occur constantly, and the system adjusts itself to the changing conditions. The system must be able to operate satisfactorily under these conditions and successfully supply the load.

This paper focuses on the stability problems caused by the penetration of power electronic converters in power grids and aims to analyze and optimize the stability of power grids through state-space equation modeling. The study encompasses various application scenarios of power electronic converters in power grids.

The world is striving to decarbonize electric energy, and some systems that previously ran on fossil fuels now sometimes produce more than half of their production from renewable energy sources [14]. In order to reach higher renewable energy penetration rates, a number of planning and operational challenges must be faced [15]. Many of these challenges are related to the uncontrollable nature of wind and solar resources, but others are related to the inverters used

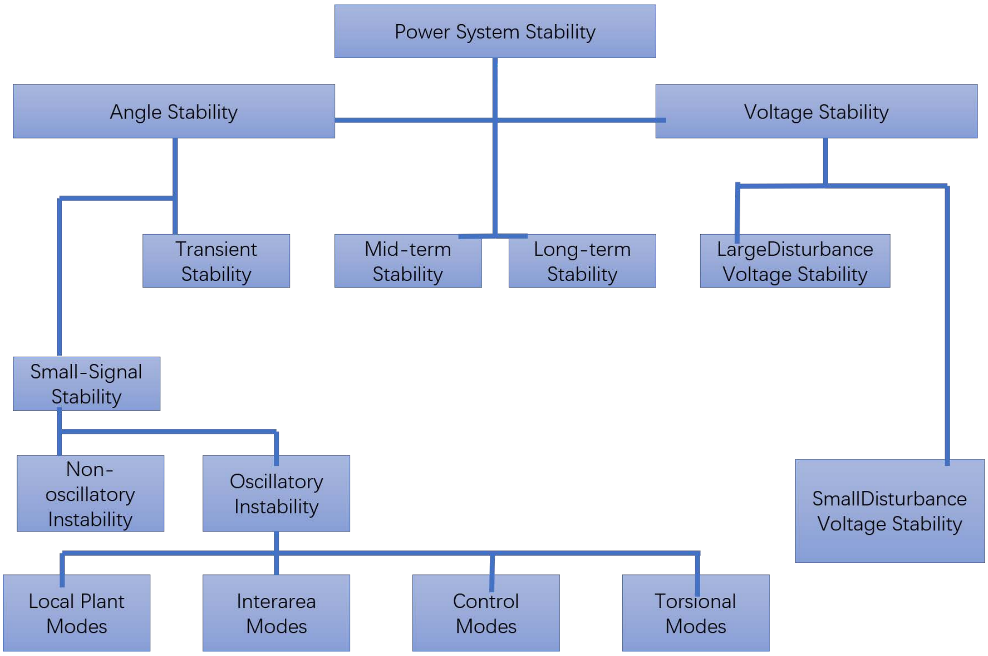

Figure 2: **Classification of power system stability** [2]

to connect wind, solar, and battery systems to the grid [16]. These are referred to as inverter-based resources (IBR).

As the number of inverters in power systems increases, concerns about changes in system dynamics and stability also increase [17]. There have been some reports that inverters are associated with threats to system stability. A particular problem is the instability of the phase-locked loops (PLLs) of the grid following (GFL) converters in weak grids [18]. Some system operators have reported poorly damped oscillation patterns for certain operating conditions when inverters dominate an area, and stability challenges may become more important in the future.

With inverter-based grid stability studies one of the main difficulties is the lack of intrinsic behavior and standard models. The physical form of the inverter has almost no intrinsic functional characteristics, and almost all of them are determined by its control algorithm. The control functions are arranged in a hierarchical structure. At the bottom level, which is also the fastest, is the modulation of semiconductor switches to synthesize a voltage that is further controlled to achieve the highest level. At the top level, there are two broad options. The first option is to output regulated power according to the available resources and demand target. In this case, the inverter is synchronized with the local grid voltage, and a current vector is injected. This inverter is usually referred to as a GFOL inverter [19]. The second option is a grid-forming (GFOR) inverter [20]. The voltage is a free-running oscillator, except that its frequency decreases in proportion to the power drawn from the source. This frequency drop gives the voltage source the ability to lock onto the grid and operate synchronously. GFOR can be compared to conventional generators because they synchronize and regulate power in a similar way [21], although GFOR inverters may behave very differently in short circuits due to their lack of overcurrent capability. The main difference between GFL and GFOR is that they need to be current or voltage source through different control methods, and this difference also brings about variations in their synchronization methods and in the priority of grid or resource conditions when setting up power delivery.

## 2.1 Small-signal stability assessment of power-electronic-dominated systems

Due to the increased penetration of power electronic converters, the stability, operation, and control of power networks are being challenged. New instabilities have emerged due to the interaction of power converter controllers with other power network components, including other power converters. Small-signal tools have proven effective in identifying and mitigating stability problems, but their development is still in progress.

Small and large signal analysis can be used to study the stability of electrical systems [13]. Small-signal modeling analysis extracts the linear dynamic behavior of the system and applies standard control engineering tools to evaluate stability and dynamic performance. The small signal analysis provides an accurate stability assessment only near the linearization point. The large signal analysis considers a single system model valid for a variety of operating points that may include nonlinearities. Although large-signal analysis appears to be more convenient than small-signal analysis, the mathematical complexity of the model and the stability assessment tools make this approach difficult to apply in everyday engineering practice.

Small-signal studies of classical power networks dominated by synchronous generators (SGs) have been used to identify sources of instability using techniques such as eigenvalues and participation factors (PFs). These models are typically developed using a state-space representation of the network, where generic models of different power system components have been widely used [2]. Frequency domain techniques have also been used for conventional power systems to identify oscillatory instabilities. In particular, the frequency scan technique and the complex torque coefficient method were used for subsynchronous oscillations involving SGs [22]. As the penetration of power electronic converters increases, it is crucial to develop small-signal models of these converters [23].

Although small signal analysis is limited to linear or linearised models around the operating point, this method can be used in conjunction with state-space models and other stability assessment techniques. Single synchronous reference frame (SSRF) qd frame or Synchronous reference frame $\alpha\beta$-frame models are commonly used to analyze stability.

Small signal stability analysis tools can be divided into two main categories: state-space and frequency domain tools. In state-space analysis, eigenvalues and PFs are the main tools for analyzing stability and identifying problem patterns. Although these methods are used for traditional power systems, their application in power electronics-based systems is also considered.

However, in power electronics based systems, additional frequency domain tools have been developed in recent years. In particular, impedance-based methods serve as a convenient solution for manufacturers and system operators to share information about converter and network dynamics without affecting their IP.

Small signal stability tools should be able to provide more information about the origin or mechanism of instabilities than just assessing stability conditions. Although state-space techniques provide more details about instabilities, information about all power components is necessary. In cases where the information is not perfect, frequency domain techniques can be considered as an alternative. However, this frequency domain technique must be able to provide details of instabilities with limited information about the system [24].

This paper focuses on the use of state-space modeling and small signal analysis for the stability assessment of typical power grids.

# 3 State-Space Modelling

In control engineering, a state-space representation is a mathematical model of a physical system specified as a set of inputs, outputs, and variables associated by first-order (no second-order derivatives involved) differential equations or difference equations. These variables are called state variables and evolve over time, depending on their values at any given instant and on the values of externally imposed input variables. The values of the output variables depend on the values of the state variables. The state-space or phase space is a geometric space in which the variables on the axes are state variables. The state of the system can be represented as a vector, the state vector, in the state-space. If the dynamical system is linear, time-invariant, and finite-dimensional, then the differential and algebraic equations can be written in matrix form. The state-space representation provides a convenient and compact method for modeling and analyzing systems with multiple inputs and outputs. Unlike frequency domain methods, the use of state-space representations is not limited to systems with linear components and zero initial conditions. State-space models can be applied to disciplines such as economics, statistics, computer science, electrical engineering, and neuroscience [25].

In this section, the analysis starts with a state-space representation of electrical circuits such as RL circuit and PI line and compares the results with those of circuits run in the Matlab/Simulink environment.

## 3.1 Linear and nonlinear components in the state-space equation

A linear circuit is a circuit whose parameters are constant over time and do not vary with voltage or current, and the circuit follows Ohm's Law. A non-linear circuit is a circuit whose parameters vary with voltage or current and the circuit does not obey Ohm's Law.

In linear circuits, the circuit can be solved with simple techniques. The response of the various network elements is linear with respect to the excitation applied to them. Non-linear circuits are more complex than linear circuits, have more data, and require more information to solve non-linear circuits, and their networks do not follow the law of superposition. The responses of the various elements are not linear with respect to their excitations.

Resistive, inductive, and capacitive components are linear elements. On the other hand, nonlinear circuits are diodes, transformers, iron cores, inductors, and transistors.

The modeling of each part of the power system by the state-space equation is also classified according to linear and nonlinear components. For example, resistors, constant inductors, and constant capacitors are linear components that can be modeled directly by circuit analysis. However, power calculations, variable loads, as well as the rotation matrix used between the circuit and the control system in the space-state equation are all non-linear elements. These components need to be linearised and transformed into state-space equations by means of Taylor expansions. In this section, the modeling of the state-space equations for each of these two types of components is described.

## 3.2 RL Circuit

The RL circuit diagram is shown in Fig. 3.

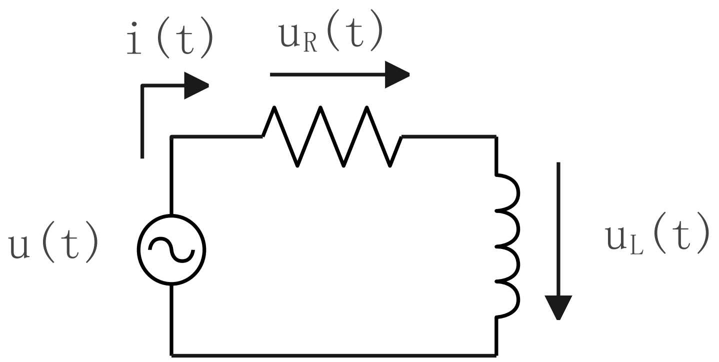

Figure 3: **RL Circuit**

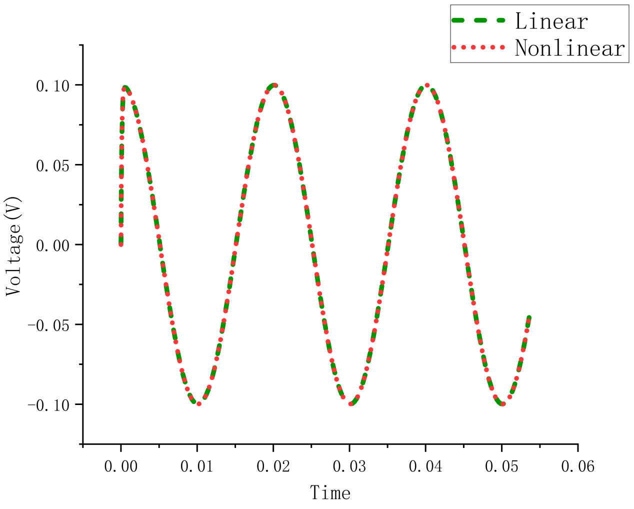

Figure 4: **Comparison of Linear and linear state-space model of RL Circuit**

Using Kirchhoff's voltage law (KVL) for RL circuits, the following Eq. (1) can be obtained.

$$u(t) = R \times i(t) + L \times \frac{di(t)}{dt} \tag{1}$$

Rearranging the equation and putting the part with the derivative to the left of the equal sign, we get Eq. (2) as follows

$$\frac{di(t)}{dt} = \frac{u(t) - Ri(t)}{L} \tag{2}$$

$$\frac{di(t)}{dt} = -\frac{R}{L}i(t) + \frac{1}{L}u(t) \tag{3}$$

The state-space model is defined by the following equation:

$$\frac{dx(t)}{dt} = Ax(t) + Bu(t) \tag{4}$$

By comparing with Eq. (4) the parameters needed for the form in the state-space equation can be obtained. It can be seen that the state variable is i(t). The matrices are Eq. (5) and (6), respectively.

$$A = [-R \times \frac{1}{L}] \tag{5}$$

$$B = [\frac{1}{L}] \tag{6}$$

Here the output variables can be selected as needed, for example, C=[1] and D=[0] when i(t) is selected as the output variable. As shown in Eq. (7) and (8).

$$i(t) = 1 \times i(t) + 0 \times u(t) \tag{7}$$

$$y(t) = Cx(t) + Du(t) \tag{8}$$

After obtaining the above data, the state-space results can be obtained by inputting the voltage as an input variable to the state-space module in Siumlink software and comparing them with the results obtained from the circuit model built directly in Siumlink.

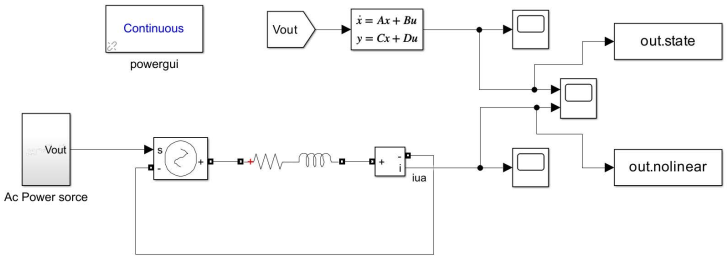

Figure 5: **The Simulink model used for RL circuits**

The structure of the Simulink model and the comparison results obtained are shown in the Fig. 5 and4, where it can be seen that the nonlinear and linear results are identical, indicating that the validation of the model is successful.

## 3.3 Thevenin PI line

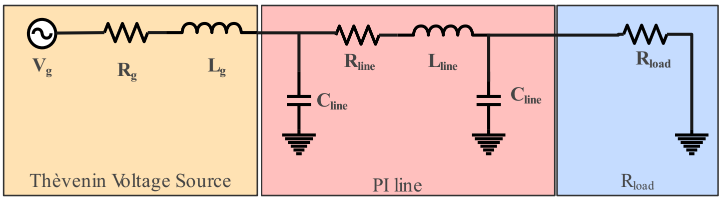

Figure 6: **Thevenin PI line circuits**

The circuit diagram of the Thevenin PI line is shown in Fig. 7.

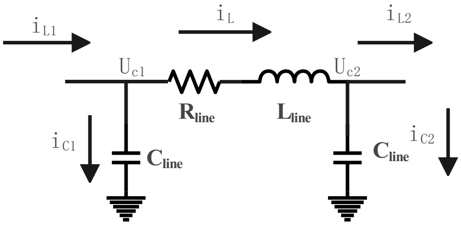

Figure 7: **Thevenin PI line circuits**

For Fig. 7 using KCL and KVL formulas for analysis and rearrangement the following formulas can be obtained.

$$\frac{di_L}{dt} = -\frac{R}{L} \times i_L + \frac{U_{c1}}{L} - \frac{U_{c2}}{L} \tag{9}$$

$$\frac{dU_{c1}}{dt} = -\frac{i_L}{C_a} + \frac{i_{L1}}{C_a} \tag{10}$$

$$\frac{dU_{c2}}{dt} = \frac{i_L}{C_a} - \frac{i_{L2}}{C_a} \tag{11}$$

The matrix form of the associated state-space equation can be obtained according to Eq. (9)-(11), and here $i_{C1}$ and $i_{C2}$ are set as the output quantities.

$$\begin{bmatrix} \frac{di_L}{dt} \\ \frac{dU_{c1}}{dt} \\ \frac{dU_{c2}}{dt} \end{bmatrix} = \begin{bmatrix} -\frac{R}{L} & \frac{1}{L} & -\frac{1}{L} \\ -\frac{1}{C_a} & 0 & 0 \\ \frac{1}{C_a} & 0 & 0 \end{bmatrix} \times \begin{bmatrix} i_L \\ U_{c1} \\ U_{c2} \end{bmatrix} + \begin{bmatrix} 0 & 0 \\ \frac{1}{C_a} & 0 \\ 0 & -\frac{1}{C_a} \end{bmatrix} \times \begin{bmatrix} i_{L1} \\ i_{L2} \end{bmatrix} \tag{12}$$

$$\begin{bmatrix} i_{C1} \\ i_{C2} \end{bmatrix} = \begin{bmatrix} -1 & 0 & 0 \\ 1 & 0 & 0 \end{bmatrix} \times \begin{bmatrix} i_L \\ U_{c1} \\ U_{c2} \end{bmatrix} + \begin{bmatrix} 1 & 0 \\ 0 & -1 \end{bmatrix} \times \begin{bmatrix} i_{L1} \\ i_{L2} \end{bmatrix} \tag{13}$$

After obtaining the above data, the linearized results can be obtained by inputting the current as an input variable to the state-space module in Siumlink software and comparing them with the results obtained from the circuit model built directly in Siumlink.

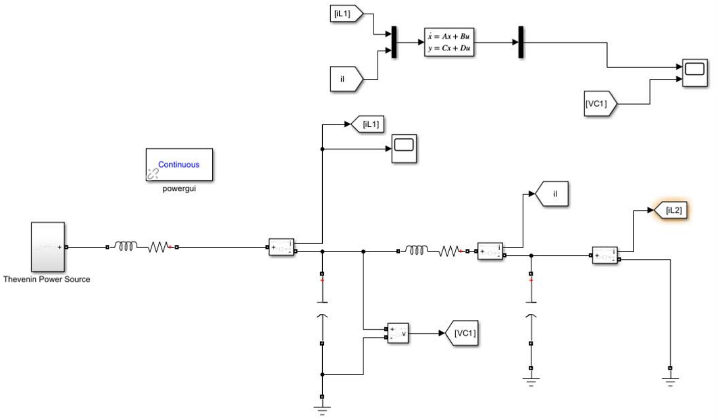

Figure 8: **The Simulink model used for PI line circuits**

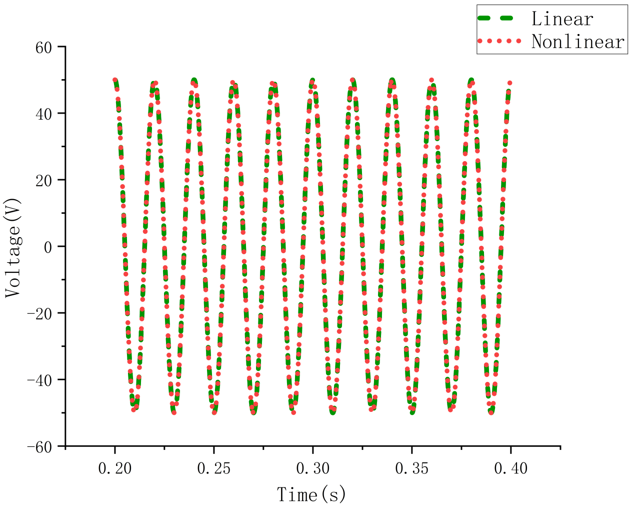

Figure 9: **Comparison of linear and linear state-space of PI Circuit**

The structure of the Simulink model and the comparison results obtained are shown in the two Fig 8 and 9, where it can be seen that the linear and linear state-space results are identical, indicating that the validation of the model is successful

## 3.4 Modelling of the state-space equation for the Thevenin PI line with a fixed load in the qd reference system

### 3.4.1 Park Transformation

The quantities in $\alpha\beta0$ are useful in many applications but have the same oscillatory nature as the quantities in the ABC frame. For the design of the controller, it is useful to have constant quantities. This can be achieved by using the Park transformation and the so-called synchronous reference frame [26].

The principle of Park Transformation is:

$$[x_{qd0}] = [x_{abc}] \times [T_{qd0}] \tag{14}$$

where the $T_{qd0}$ matrix is:

$$T_{qd0} = \frac{2}{3} \times \begin{bmatrix} cos(\theta) & cos(\theta - \frac{2\pi}{3}) & cos(\theta + \frac{2\pi}{3}) \\ sin(\theta) & sin(\theta - \frac{2\pi}{3}) & sin(\theta + \frac{2\pi}{3}) \\ \frac{1}{2} & \frac{1}{2} & \frac{1}{2} \end{bmatrix} \tag{15}$$

### 3.4.2 PI line

Converting the model in Fig. 7 to the qd frame system gives us Fig. 10. Based on the model in Fig. 10 using KVL and KCL the following equations can be obtained. The model in Fig. 10 is based on qd as the reference coordinate system.

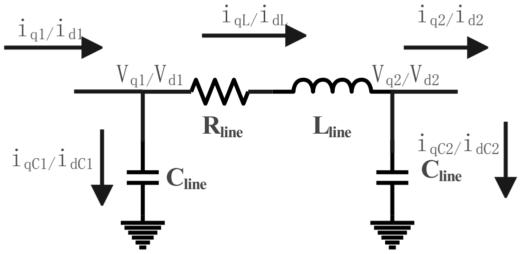

Figure 10: **PI line in q coordinate system**

$$i_{q1} - i_{qL} = C_1 \times \frac{dv_{1q}}{dt} + w \times C_1 \times V_{1d} \tag{16}$$

$$i_{d1} - i_{dL} = C_1 \times \frac{dv_{1d}}{dt} - w \times C_1 \times V_{1d} \tag{17}$$

$$i_{qL} - i_{q2} = C_2 \times \frac{dv_{q2}}{dt} + w \times C_2 \times V_{2d} \tag{18}$$

$$i_{dL} - i_{d2} = C_2 \times \frac{dv_{d2}}{dt} - w \times C_2 \times V_{2q} \tag{19}$$

$$V_{1q} - V_{2q} = R \times i_{qL} + L \times \frac{di_{qL}}{dt} + w \times L \times i_{dL} \tag{20}$$

$$V_{1d} - V_{2d} = R \times i_{dL} + L \times \frac{di_{dL}}{dt} - w \times L \times i_{qL} \tag{21}$$

Organizing the above equation into the matrix form of the state-space equation yields the following matrix

$$\begin{bmatrix} \frac{dV_{q1}}{dt} \\ \frac{dV_{d1}}{dt} \\ \frac{dV_{q2}}{dt} \\ \frac{dV_{d2}}{dt} \\ \frac{di_{qL}}{dt} \\ \frac{di_{dL}}{dt} \end{bmatrix} = \begin{bmatrix} 0 & -w & 0 & 0 & -\frac{1}{C_1} & 0 \\ w & 0 & 0 & 0 & 0 & -\frac{1}{C_1} \\ 0 & 0 & 0 & -w & \frac{1}{C_2} & 0 \\ 0 & 0 & w & 0 & 0 & \frac{1}{C_2} \\ \frac{1}{L} & 0 & -\frac{1}{L} & 0 & -\frac{R}{L} & -w \\ 0 & \frac{1}{L} & 0 & -\frac{1}{L} & w & -\frac{R}{L} \end{bmatrix} + \begin{bmatrix} \frac{1}{C_1} & 0 & 0 & 0 \\ 0 & \frac{1}{C_1} & 0 & 0 \\ 0 & 0 & -\frac{1}{C_2} & 0 \\ 0 & 0 & 0 & -\frac{1}{C_2} \\ 0 & 0 & 0 & 0 \\ 0 & 0 & 0 & 0 \end{bmatrix} \times \begin{bmatrix} i_{q1} \\ i_{d1} \\ i_{q2} \\ i_{d2} \end{bmatrix} \tag{22}$$

### 3.4.3 Thèvenin Voltage Source

The Thèvenin Voltage Source in Fig. 6 is shown specifically in Fig. 11.

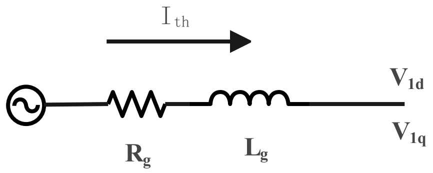

Figure 11: **Thèvenin Voltage Source**

Based on the model in Fig. 11, using KVL and KCL, the following matrix can be obtained.

$$\begin{bmatrix} \frac{dI_{qth}}{dt} \\ \frac{dI_{dth}}{dt} \end{bmatrix} = \begin{bmatrix} -\frac{R_g}{L_g} & -w \\ w & -\frac{R_g}{L_g} \end{bmatrix} \times \begin{bmatrix} I_{qth} \\ I_{dth} \end{bmatrix} + \begin{bmatrix} \frac{1}{L_g} & 0 & \frac{1}{L_g} & 0 \\ 0 & \frac{1}{L_g} & 0 & -\frac{1}{L_g} \end{bmatrix} \times \begin{bmatrix} V_{qth} \\ V_{dth} \\ V_{1q} \\ V_{1d} \end{bmatrix} \tag{23}$$

### 3.4.4 Resistive load

The Resistive load in Fig. 6 is shown specifically in Fig. 12.

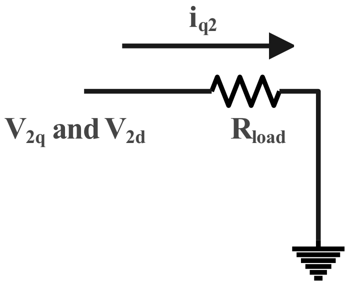

Figure 12: **Resistive load**

Equating the state-space of the resistive load part of the Fig. 6 leads to the following matrix

$$\begin{bmatrix} i_{2q} \\ i_{2d} \end{bmatrix} = \begin{bmatrix} \frac{1}{R_{load}} & 0 \\ 0 & -\frac{1}{R_{load}} \end{bmatrix} \times \begin{bmatrix} V_{2q} \\ V_{2d} \end{bmatrix} \tag{24}$$

For this part, because there is no integral or differential term in the formula, there are no state variables, only input and output quantities.

### 3.4.5 Integration and validation

The above components are integrated and modeled in Simulink, and each matrix is integrated into Matlab using the connect function to obtain the ABCD matrix of the state-space equations for the whole system.

The model used in Simulink and the verification results are shown below.

In this model, the voltages $V_{thq}$ and $V_{thq}$ on Thèvenin Voltage Source are set as inputs while $i_{q2}, i_{d2}, V_{2q}$ and $V_{2d}$ are set as outputs. In order to evaluate the capability of the state-space model in capturing dynamics, the voltage level of the Thèvenin Voltage source was increased by one-third in the first second.

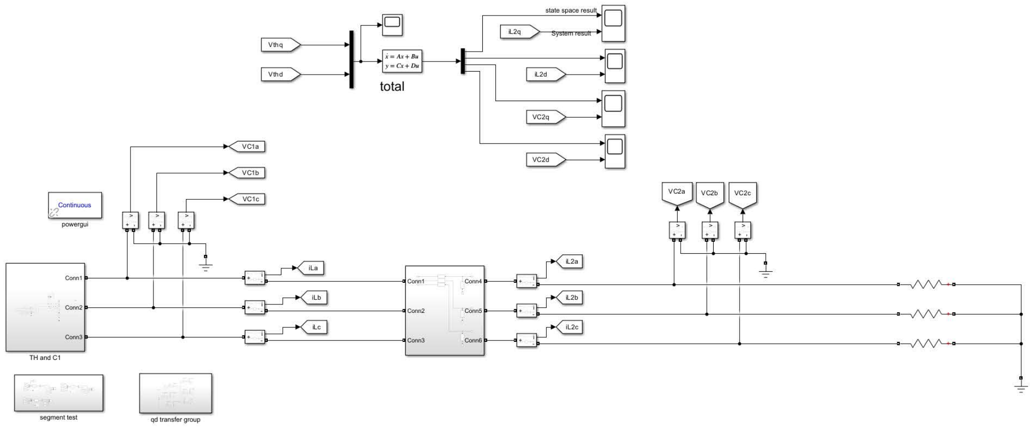

Figure 13: **The Simulink model used for Thevenin PI line circuits with resistive load in qd frame**

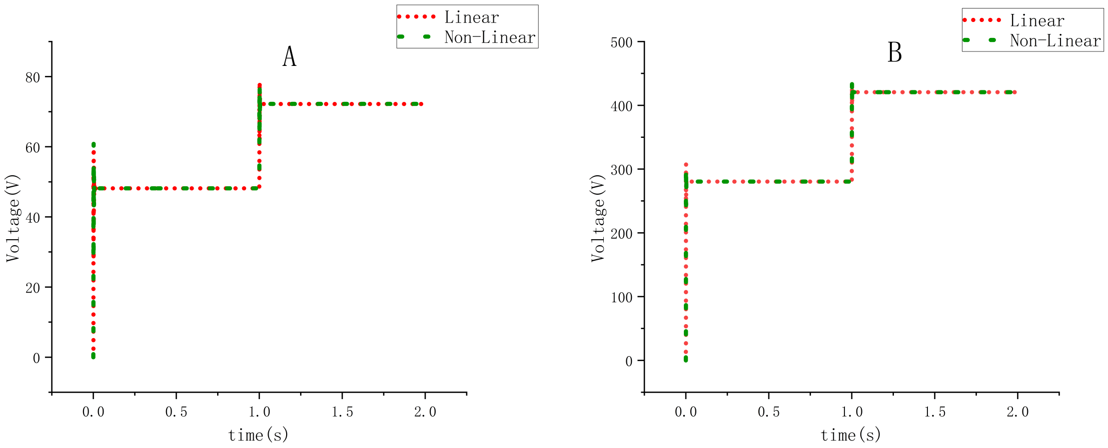

Figure 14: **Comparison of linear state-space and linear circuit of Thevenin PI line circuits with constant load in qd frame(A)**$V_{2d}$,**(B)**$V_{2q}$

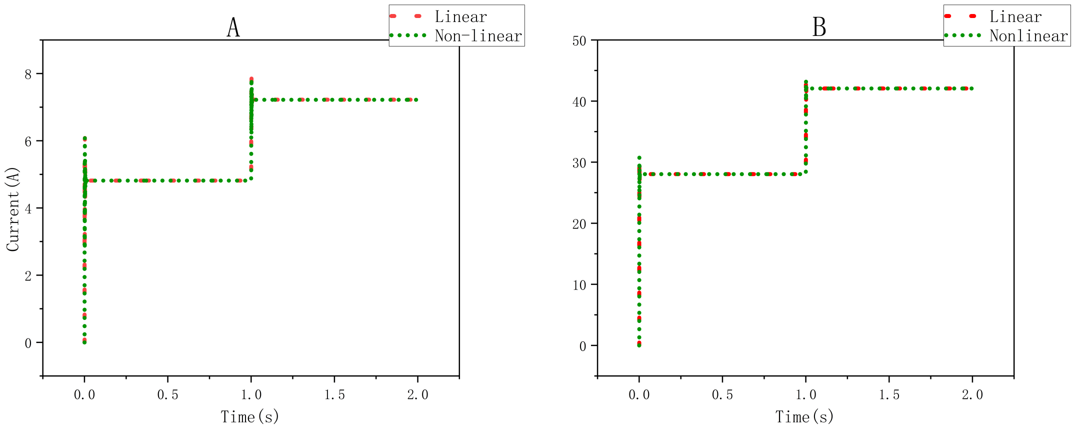

Figure 15: **Comparison of linear state-space and linear circuit of Thevenin PI line circuits with constant load in qd frame(A)$I_{2d}$,(B)$I_{2q}$**

As can be seen in Fig. 14 and15, the linear results obtained from the state-space equation and the linear results obtained from the system simulation are the same, and the verification results are correct and as expected.

# 4 Linearization

## 4.1 Linearization via Taylor Series

The behavior of a dynamic system, such as an electric power system, can be described by a system of n first-order non-linear ordinary differential equations of the following form:

$$\dot{x_i} = f_i(x_1, x_2, ..., x_n; u_1, u_2, ..., u_r) i = 1, 2, ..., n \tag{25}$$

where n is the order of the system and r is the number of inputs. This can be written in the following form by using vector-matrix notation:

$$\dot{X} = f(X, U) \tag{26}$$

Of which:

$$X = \begin{bmatrix} x_1 \\ x_2 \\ ... \\ x_n \end{bmatrix} \tag{27}$$

$$U = \begin{bmatrix} u_1 \\ u_2 \\ ... \\ u_n \end{bmatrix} \tag{28}$$

The equilibrium points are those where all derivatives are zero at the same time. The system is accordingly at rest because all the variables are constant and do not change with time. So the result of Eq. (29) is 0.

In order to linearise a general non-linear system, a Taylor series function is used to expand it. The linearization of the equations proceeds as follows: let $X_0$ be the initial state vector and $U_0$ be the input vector corresponding to the equilibrium point about where the small signal performance will be investigated. Since when X = $X_0$, there is $\dot{X}$ = 0 (i.e., the system reaches equilibrium at $X_0$). The following formula can be obtained.

$$\dot{X} = f(X_o, U_0) = 0 \tag{29}$$

The addition of perturbations gives the following equation:

$$X = X_o + \triangle X \tag{30}$$

$$U = U_o + \triangle U \tag{31}$$

where the $\triangle$ represents a small disturbance. Substituting Eq. (30) and (31) into Eq. (29) yields Eq. (32).

$$\dot{X} = \dot{X_0} + \triangle\dot{X} = f[(X_0 + \triangle X)]), (U_0 + \triangle U)]) \tag{32}$$

Eq. (33) is obtained by using a Taylor expansion for Eq. (32) and ignoring the second and higher-than-second terms.

$$\begin{aligned} \dot{x_i} &= \dot{x_{i0}} + \triangle x_{i0} = f_i[(X_0 + \triangle X)]), (U_0 + \triangle U)] \\ &= f_i(X_0, U_0) + \frac{\partial f_i}{\partial x_1} \triangle x_1 + ... + \frac{\partial f_i}{\partial x_n} \triangle x_n \\ &+ \frac{\partial f_i}{\partial u_1} \triangle u_1 + ... + \frac{\partial f_i}{\partial u_r} \triangle u_r \end{aligned} \tag{33}$$

where $f_i[(X_0, U_0)]$ is 0. So Eq. (34) is obtained:

$$\triangle\dot{x_i} = \frac{\partial f_i}{\partial x_1} \triangle x_1 + ... + \frac{\partial f_i}{\partial x_n} \triangle x_n + \frac{\partial f_i}{\partial u_1} \triangle u_1 + ... + \frac{\partial f_i}{\partial u_r} \triangle u_r \tag{34}$$

Eq. (34) can be arranged in the form of a state-space equation, as shown in Eq. (35).

$$\triangle\dot{x} = A \triangle x + B \triangle x \tag{35}$$

### 4.2 Linearization of the power equation with qd as the reference coordinate system

As previously stated, in order to achieve steady-state quantities, the angle $\theta$ used in the Park transformation represents the electrical voltage angle. By substituting $\theta$ with the electrical angle $\theta = \omega t + \phi 0$, and performing the transformation of abc voltages and currents to the qd0 frame, the resulting voltage and current phasors can be defined similarly to the Clarke transformation case. As shown in (36) and (37).

$$V^{qd} = \frac{V_q - jV_d}{\sqrt{2}} \tag{36}$$

$$I^{qd} = \frac{i_q - ji_d}{\sqrt{2}} \tag{37}$$

According to the above equation, the power of the three-phase system can be obtained as

$$S = P + jQ = 3V^{qd}I^{qd*} = 3(\frac{V_q - jV_d}{\sqrt{2}})(\frac{i_q + ji_d}{\sqrt{2}}) \tag{38}$$

According to the above equations, the equations for active and reactive power in the qd0 reference system can be obtained as:

$$P = \frac{3}{2}(v_q i_q + v_d i_d) \tag{39}$$

$$Q = \frac{3}{2}(v_q i_d - v_d i_q) \tag{40}$$

Linearizing the equations for P and Q above separately: If Eq. (39) is perturbed the following equation can be obtained. Note that parameters that have subscript 0 denote the linearization points.

$$P_0 + \triangle P = \frac{3}{2}(V_{d0} + \triangle V_d)(I_{d0} + \triangle I_d) + \frac{3}{2}(V_{q0} + \triangle V_q)(I_{q0} + \triangle I_q) \tag{41}$$

In the above equation, the product of the two small perturbations is very small and can be neglected. A Taylor expansion for the above equation yields:

$$\triangle P = \frac{3}{2}(V_{d0} \triangle I_d + I_{d0} \triangle V_d + V_{q0} \triangle I_q + I_{q0} \triangle V_q) \tag{42}$$

This gives the state-space equation of active power as:

$$\triangle P = \begin{bmatrix} \frac{3}{2}V_{d0} & \frac{3}{2}I_{d0} & \frac{3}{2}V_{q0} & \frac{3}{2}I_{q0} \end{bmatrix} \times \begin{bmatrix} \triangle I_d \\ \triangle V_d \\ \triangle I_q \\ \triangle V_q \end{bmatrix} \tag{43}$$

the same procedure can be applied to reactive power calculation as well, the state-space equation of reactive power can be derived as follows:

$$Q + \triangle Q = \frac{3}{2}(V_{q0} + \triangle V_q)(I_{d0} + \triangle I_d) - \frac{3}{2}(V_{d0} + \triangle V_d)(I_{q0} + \triangle I_q) \tag{44}$$

$$\triangle Q = \frac{3}{2}(V_{q0} \triangle I_d + I_{d0} \triangle V_q - V_{d0} \triangle I_q - I_{q0} \triangle V_d) \tag{45}$$

$$\triangle Q = \begin{bmatrix} \frac{3}{2}V_{q0} & -\frac{3}{2}I_{d0} & -\frac{3}{2}V_{d0} & \frac{3}{2}I_{q0} \end{bmatrix} \times \begin{bmatrix} \triangle I_d \\ \triangle V_q \\ \triangle I_q \\ \triangle V_d \end{bmatrix} \tag{46}$$

## 4.3 Linearization of rotation matrix

The modeling of the state-space equation of the entire power system includes the modeling of the power system components as well as the modeling of the control blocks. In the process of relating the variables in the state-space equation of the power system module to the variables in the control module's state-space equation, it is necessary to consider the disturbances of each power component in between, which cause an angular difference between the variables in the two. So here a rotation matrix is needed to rotate between the two variables to avoid this error. The formula for rotating the matrix counterclockwise is shown in Eq. (47).

$$\begin{bmatrix} X_{qc} \\ X_{dc} \end{bmatrix} = \begin{bmatrix} cos\theta & -sin\theta \\ sin\theta & cos\theta \end{bmatrix} \times \begin{bmatrix} X_q \\ X_d \end{bmatrix} \tag{47}$$

Performing a first-order Taylor expansion on Eq. (47) and then linearising it, the state-space equation of the rotation matrix can be obtained as

$$\begin{bmatrix} \triangle X_{qc} \\ \triangle X_{dc} \end{bmatrix} = \begin{bmatrix} cos\theta_0 & -sin\theta_0 & -sin\theta_0 X_{q0} - cos\theta_0 X_{d0} \\ sin\theta_0 & cos\theta_0 & cos\theta_0 X_{q0} - sin\theta_0 X_{d0} \end{bmatrix} \times \begin{bmatrix} \triangle X_q \\ \triangle X_d \\ \triangle\theta \end{bmatrix} \tag{48}$$

## 4.4 Modelling of the state-space equation for the Thevenin PI line with variable loads in the qd reference system

In order to more closely resemble a realistic power system, the fixed load in Fig. 6 is replaced by a variable load, which makes the load section a non-linear unit. Based on what was presented in the previous section, the load is linearised in this section.

Using the q reference coordinates as an example, an analysis of this part gives the following equation:

$$i_q = \frac{V_q}{R_{load}} \tag{49}$$

Expansion of the above equation according to Eq. (34) gives Eq. (50).

$$i_{q0} + \triangle i_q = \frac{V_{q0} + \triangle V_q}{R_0 + \triangle R} \tag{50}$$

Performing the Taylor expansion for Eq. (50) yields Eq. (51).

$$\begin{aligned} \frac{V_{q0} + \triangle V_q}{R_0 + \triangle R} &= \frac{\partial \frac{V_{q0}+\triangle V_q}{R_0+\triangle R}}{\partial \triangle V_q} \triangle V_q + \frac{\partial \frac{V_{q0}+\triangle V_q}{R_0+\triangle R}}{\partial \triangle R} \triangle R \\ &= \frac{\triangle V_q}{R_0 + \triangle R} + \frac{-(V_{q0} + \triangle V_q)}{(R_0 + \triangle R)^2} \\ &= \frac{\triangle V_q}{R_0} + \frac{-(V_{q0})}{(R_0)^2} \triangle R \end{aligned} \tag{51}$$

The matrix of the state-space equation for the variable load part can be obtained from the above equation:

$$D_{load} = \begin{bmatrix} \frac{1}{R_o} & 0 & \frac{-V_{q0}}{(R_0)^2} \\ 0 & \frac{1}{R_o} & \frac{-V_{d0}}{(R_0)^2} \end{bmatrix} \tag{52}$$

The other matrices in this section are all zero matrices, with the input quantities being the voltage and the variation of the load resistance and the output quantity being the current.

The matrices of the state-space equations for the other parts of the model are the same as in Section 3, still using the connect function in Matlab to link each part together. the linearized state-space model results obtained from the state-space equations are compared with the nonlinear results obtained from simulating the power system in Simulink.

Simulink's structure diagram and a comparison of the linear and nonlinear results are shown in Fig. 16 and Fig. 17.

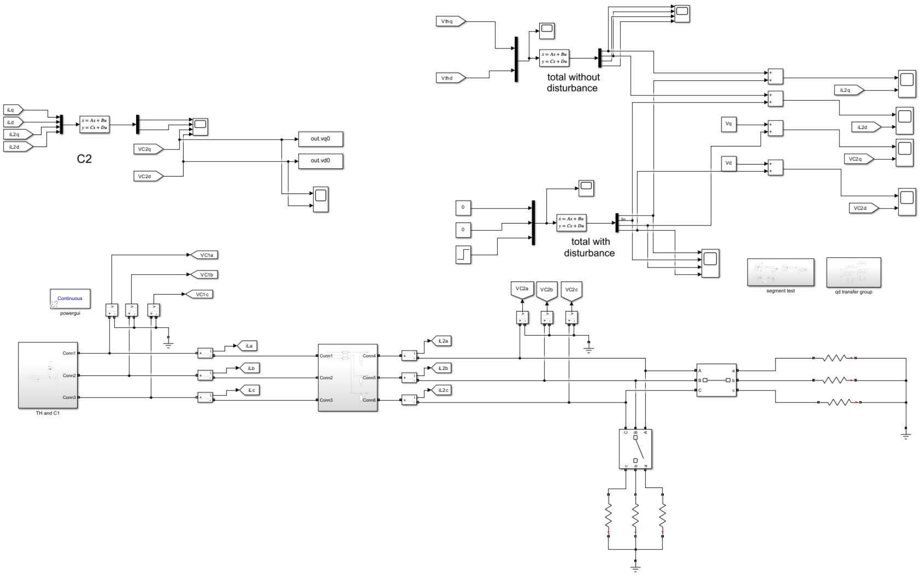

Figure 16: **The Simulink model used for Thevenin PI line circuits with active load in qd frame**

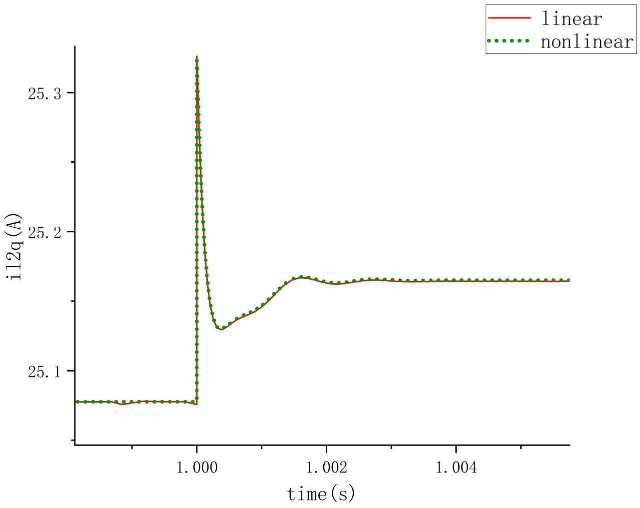

Figure 17: **Comparison of $i_{q2}$ for linear and non-linear models of Thevenin PI line circuits with variable loads in the qd framework**

As shown in Fig. 16, the power system in this section is designed to change the load of the whole system by paralleling new loads. The new load is connected at the 1 s, and it can be seen that each nonlinear variable changes suddenly at this moment, but after stabilization, it is the same as the result after linearization, which shows that the state-space equation built in this section is correct and the verification is successful.

# 5 GFOL system modeling and state-space equation modeling

The center of this chapter is the so-called two-stage voltage source converter (VSC). This section presents a comprehensive description and justification of control schemes capable of independently controlling active and reactive power. Simulation results are used to illustrate the dynamic performance of the control scheme. In the GFOL the inverter is controlled as a current source and the frequency is set by phase-locking to the existing grid. The structure is shown in Fig. 18.

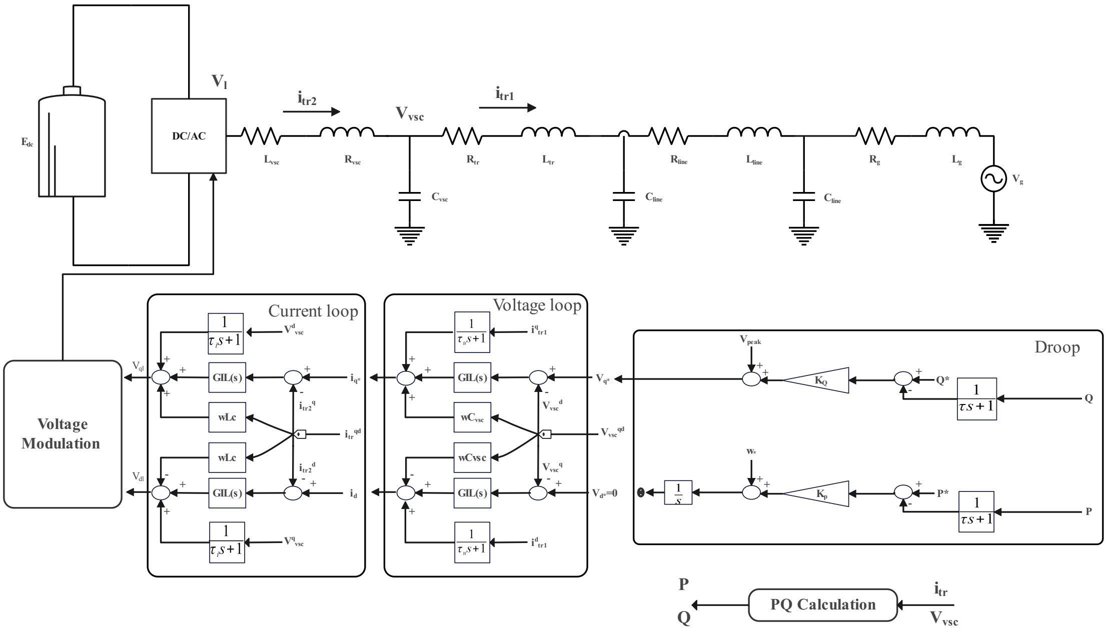

]

Figure 18: **Structure of GFOL** [3]

In this mode of operation, the utility grid regulates the network voltage amperage, frequency and phase at the point of common coupling (PCC), corresponding to the electrical connection point between the microgrid and the main grid [27]. The converter system is electronically coupled to a distributed energy source dedicated to one or a group of loads, usually acting as a voltage follower in grid-connected mode, and is classified as a networked feeder. When power electronic converters are controlled for networked feeds, they are permanently synchronized with the main grid and configured to operate as equivalent to a current source. This operation is mainly implemented on non-distributable intermittent renewable energy sources that require a maximum power point tracking (MPPT) algorithm, which is beneficial for extracting the maximum available power from the generation source [28].

A diagrammatic representation of the system investigated in this section is shown in Fig. 19. The grid under consideration is a three-phase, three-wire grid. A two-stage voltage source converter (VSC) exchanges power between the AC side and the DC side. Proper modulation of the switches can generate the desired three-phase voltages on the AC side, allowing control over active and reactive power flow.

The DC side can be modeled as a DC voltage source or as a current source connected to a shunt capacitor. The AC side can be modeled with the Thevenin equivalent of the utility grid or, in an extremely simple system, with an AC voltage source. It is worth noting that the VSC converter itself can be considered an AC voltage source, which can be connected to the grid without any problem [4].

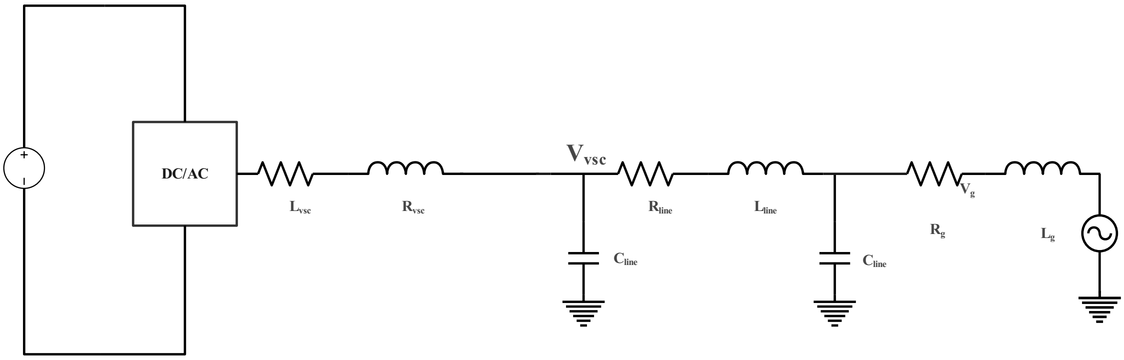

Figure 19: **System under analysis comprising the VSC converter and the three-phase utility grid** [4]

The control scheme modeled in this section accomplishes the control for both active and reactive power. The simulated object at the DC side can inject power into the grid or receive power from the grid to charge it in reverse. The specific control scheme includes energy control, current loop control, and PLL control. The reference value of the qd AC current is obtained by the power control module, while the higher-level current loop is responsible for regulating the bus voltage. Since these controllers handle the current and voltage in the qd0 reference frame, they need to be adjusted according to the grid angle therefore a phase-locked loop (PLL) is needed to track the grid angle.

The specific schematic of the control structure is shown in Fig. 18.

## 5.1 Voltage Equations in the Synchronous Reference Frame

The model mentioned above is simplified as shown in Fig. 20, and the circuit analysis is performed for this model. The circuit analysis leads to Eq. (53).

$$\begin{bmatrix} V_{za} \\ V_{zb} \\ V_{zc} \end{bmatrix} - \begin{bmatrix} V_{la} \\ V_{lb} \\ V_{lc} \end{bmatrix} - (V_{l0} - V_{z0}) \begin{bmatrix} 1 \\ 1 \\ 1 \end{bmatrix} = \begin{bmatrix} r_l & 0 & 0 \\ 0 & r_l & 0 \\ 0 & 0 & r_l \end{bmatrix} \begin{bmatrix} i_a \\ i_b \\ i_c \end{bmatrix} + \begin{bmatrix} l_l & 0 & 0 \\ 0 & l_l & 0 \\ 0 & 0 & l_l \end{bmatrix} \frac{d}{dt} \begin{bmatrix} i_a \\ i_b \\ i_c \end{bmatrix} \tag{53}$$

Where $v_{za}$, $v_{zb}$ and $v_{zc}$ are the three-phase instantaneous grid voltages in the ABC frame, $v_{la}$, $v_{lb}$ and $v_{lc}$ are the three-phase instantaneous converter voltages in the ABC frame, $i_a$, $i_b$ and $i_c$ are the three-phase instantaneous currents in the ABC frame, $r_l$ is the inductance equivalent resistance and $l_l$ is the inductance value. $v_{l0}$ -$v_{z0}$ is the voltage difference between the converter and the grid neutral. In three-phase balanced systems $v_{l0}$ -$v_{z0}$ is 0 [4].

Eq. (54) can be obtained by using the Parker transformation to Eq. (53).

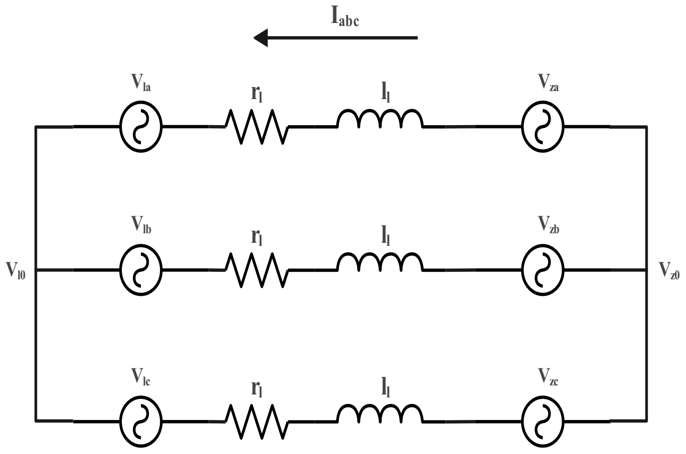

Figure 20: **Equivalent model of the AC side of a VSC convert** [4]

$$\begin{bmatrix} V_{zq} \\ V_{zd} \end{bmatrix} - \begin{bmatrix} V_{lq} \\ V_{ld} \end{bmatrix} = \begin{bmatrix} r_l & -l_l w_e \\ l_l w_e & r_l \end{bmatrix} \begin{bmatrix} i_q \\ i_d \end{bmatrix} + \begin{bmatrix} l_l & 0 \\ 0 & l_l \end{bmatrix} \frac{d}{dt} \begin{bmatrix} i_q \\ i_d \end{bmatrix} \tag{54}$$

where $v_{zq}$ and $v_{zd}$ are grid qd voltages, $v_{lq}$ and $v_{ld}$ are converter qd voltages, $i_q$ and $i_d$ are qd currents, and $w_e$ is the electrical angular velocity.

## 5.2 Droop control

Droop control is the simplest implementation of the swing equation. The main idea is to measure active and reactive power and to use the variation of the measured power flow to provide set points for voltage and current controllers. Droop control has historically been implemented in microgrids, introducing the possibility of several converters operating in parallel and forming a grid together [29].

In Fig. 21, the reference frequency represents the operating frequency of the system, which is 50Hz. In the droop control, the input frequency $\omega$ is provided by the PLL module. This frequency is first passed through a low-pass filter to eliminate high-frequency signals and then multiplied by Kp to obtain the reference active power.

The reference voltage value is measured as Vpeak at the Point of Common Coupling (PCC), while Vpoc is obtained through the PLL module. Vpoc also needs to pass through a low-pass filter first.

The state-space equation for the droop section is built from Fig. 21:

$$P_u^* = \begin{bmatrix} K_Q & -K_Q & 1 \end{bmatrix} \begin{bmatrix} w^* \\ w \\ P^* \end{bmatrix} \tag{55}$$

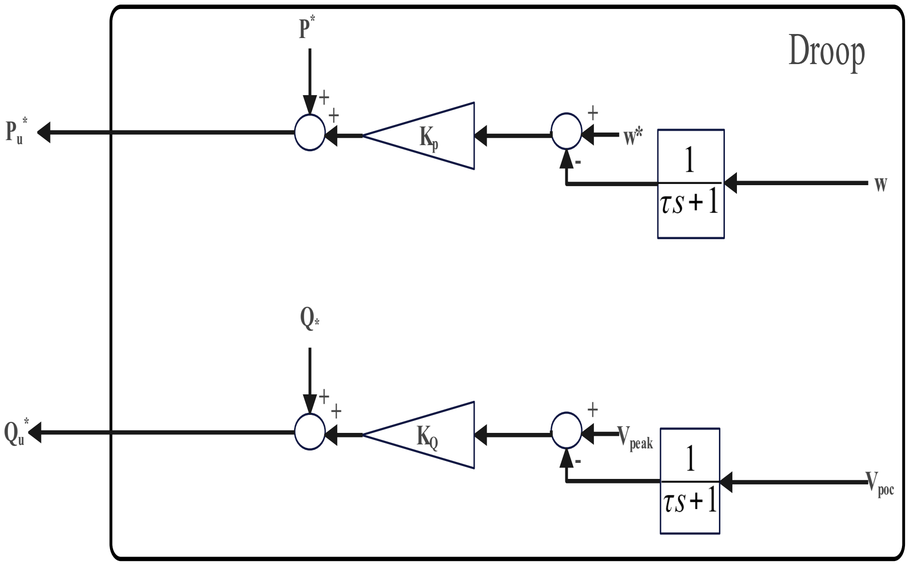

Figure 21: **Droop control module for GOLF**

$$Q_u^* = \begin{bmatrix} K_P & -K_P & 1 \end{bmatrix} \begin{bmatrix} V_{peak} \\ V_{poc} \\ Q^* \end{bmatrix} \tag{56}$$

## 5.3 Power Control Module

The phase-locked loop system not only tracks the electrical grid angle but also ensures that $v_d$ = 0 when tracking. Combining the previous equations for active and reactive power yields the following equation, which also finds that P is only related to iq and Q is only related to $i_d$. The specific relationships are shown below.

$$i_q^* = \frac{2}{3}\frac{P_*}{V_{zq}} \tag{57}$$

$$i_d^* = \frac{2}{3}\frac{Q_*}{V_{zq}} \tag{58}$$

The control structure of the power control part is shown in Fig. 22.

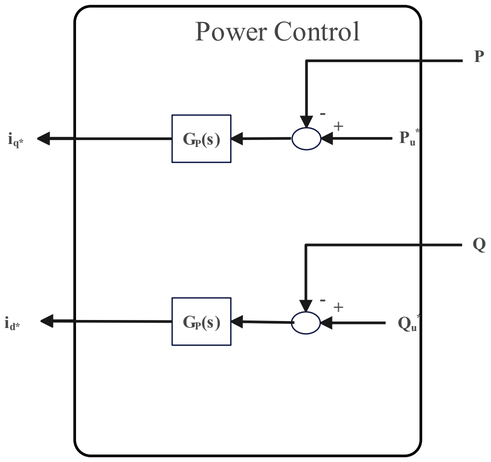

Figure 22: **Power control module for GOLF**

### 5.3.1 Power control module state-space equation

According to the structure in Fig. 22, the following equation can be obtained:

$$(P_{ref} - \triangle P) \times (K_{P_p} + \frac{K_{i_p}}{s}) = I_{ref} \tag{59}$$

where variables such as $k_{i_p}$ are obtained from the following equation, $taus$ is the time constant of the current loop, and $taup$ and $tauq$ are the time constants of the power control module.

$$k_{P_p} = 1e^{-3} * taus/tau_p \tag{60}$$

$$k_{i_p} = 1e^{-3} * 1/tau_p \tag{61}$$

$$k_{P_Q} = 1e^{-3} * taus/tau_q \tag{62}$$

$$k_{i_Q} = 1e^{-3} * 1/tau_q \tag{63}$$

Where $\triangle P$ can be further expanded according to the previously obtained Eq. (42), the results of the expansion are substituted and organized to obtain the following equation.

$$\frac{\mathrm{d}(I_{ref} - (P_{ref} - \triangle P)K_{P_p})}{\mathrm{d}t} = P_{ref} - V_{dlo} \triangle I_{d}l - V_{ql0} \triangle I_q - I_{dl0} \triangle V_{d}l - I_{ql0} \triangle V_{q}l \tag{64}$$

this equation is nonlinear and hence should be linearized by applying Taylor. This is a nonlinear system, so only a very small perturbation at a steady state is considered, and all $P_0$ here is 0. The current and voltage here are the voltage and current at the front of the filter of the converter, i.e. Represents $I_{ref} - (P_{ref} - \triangle P)$ as a $K_{pp}$.This leads to the state-space equation as Eq. (65) and (66):

$$\frac{\mathrm{d}K_{pp}}{\mathrm{dt}} = K_{pp}\begin{bmatrix}0\end{bmatrix} + \begin{bmatrix} k_{i_P} & -1.5ki_P \times I_{ql0} & -1.5k_{i_P} \times I_{dl0} & -1.5k_{i_P} \times V_{ql0} & -1.5k_{i_P} \times V_{dl0}\end{bmatrix}\begin{bmatrix}P_{ref}\\ \triangle V_q l\\ \triangle V_d l\\ \triangle I_q l\\ \triangle I_d l\end{bmatrix} \tag{65}$$

$$I_{pref} = K_{pp}\begin{bmatrix}1\end{bmatrix} + \begin{bmatrix} k_{P_P} & -1.5k_{P_P} \times I_{ql0} & -1.5k_{P_P} \times I_{dl0} & -1.5k_{P_P} \times V_{ql0} & -1.5k_{P_P} \times V_{dl0}\end{bmatrix}\begin{bmatrix}P_{ref}\\ \triangle V_q l\\ \triangle V_d l\\ \triangle I_q l\\ \triangle I_d l\end{bmatrix} \tag{66}$$

According to the same logical derivation, the state-space equation of the reactive power control module can be obtained as:

$$\frac{\mathrm{d}K_{qq}}{\mathrm{dt}} = K_{qq}\begin{bmatrix}0\end{bmatrix} + \begin{bmatrix} k_{i_Q} & -1.5ki_Q \times I_{dl0} & 1.5k_{i_Q} \times I_{ql0} & 1.5k_{i_Q} \times V_{dl0} & -1.5k_{i_Q} \times V_{ql0}\end{bmatrix}\begin{bmatrix}P_{ref}\\ \triangle V_q l\\ \triangle V_d l\\ \triangle I_q l\\ \triangle I_d l\end{bmatrix} \tag{67}$$

$$I_{qref} = K_{qq}\begin{bmatrix}1\end{bmatrix} + \begin{bmatrix} k_{P_Q} & -1.5k_{P_Q} \times I_{dl0} & 1.5k_{P_Q} \times I_{ql0} & 1.5k_{P_Q} \times V_{dl0} & -1.5k_{P_Q} \times V_{ql0}\end{bmatrix}\begin{bmatrix}P_{ref}\\ \triangle V_q l\\ \triangle V_d l\\ \triangle I_q l\\ \triangle I_d l\end{bmatrix} \tag{68}$$

## 5.4 Phase Locked Loop

A phase-locked loop (PLL) is used as a control module to determine the angle and angular velocity of the grid. The output of this controller corresponds to the angular velocity $\omega_e$ of the grid, while the integral of the angular velocity corresponds to the grid angle $\theta_e$. A typical phase-locked loop scheme is shown in Fig. 23.

The transform equation of the PLL, after simplifying, has the form shown in Eq. (69).

$$G_{pll}(s) = \frac{\hat{\theta}(s)}{\theta(s)} = \frac{2\xi w_n s + w_n^2}{s^2 + 2\xi w_n + w_2^2} \tag{69}$$

The control equation of the PLL control module is as follows:

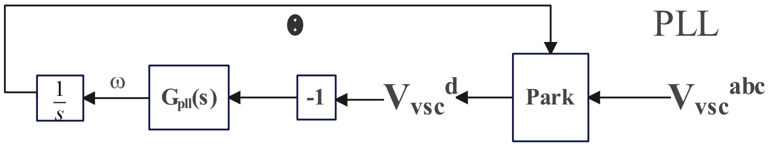

Figure 23: **Phase Locked Loop**

$$G_{pll}(s) = K_p(\frac{\frac{1}{\tau PLL} + s}{s}) \tag{70}$$

where $\tau PLL$ is the time constant. The Kp and Ki of the PLL can be calculated from the equations of the damping ratio $\xi$ and the angular velocity $w_n$. where $E_m$ is the peak voltage of the PLL tracking site.

$$w_n = \sqrt{\frac{K_p E_m}{\tau PLL}} \tag{71}$$

$$\xi = \frac{\sqrt{\tau PLL K_p E_m}}{2} \tag{72}$$

The tracking effects of the PLL outputs used for the models built in this chapter are shown in Fig. 24.

### 5.4.1 PLL state-space equation

Based on Fig. 23, the following equations can be obtained to get the state-space equation. where $k_{i_{pll}}$ and $k_{p_{pll}}$ are the control coefficients in the $G_{pll}$. $V_d$ is obtained by applying a rotation matrix to its space-state form in the power system.

$$-V_d(k_{p_{pll}} + \frac{k_{i_{pll}}}{s}) = w \tag{73}$$

$$\frac{\mathrm{d}(V_d k_{p_{pll}} + w)}{\mathrm{d}t} = -V_d k_{i_{pll}} \tag{74}$$

The state variables are expressed in a simpler form according to Eq. (75).

$$V_d k_{p_{pll}} + w = K_{PLL} \tag{75}$$

And the state-space equation can be obtained as:

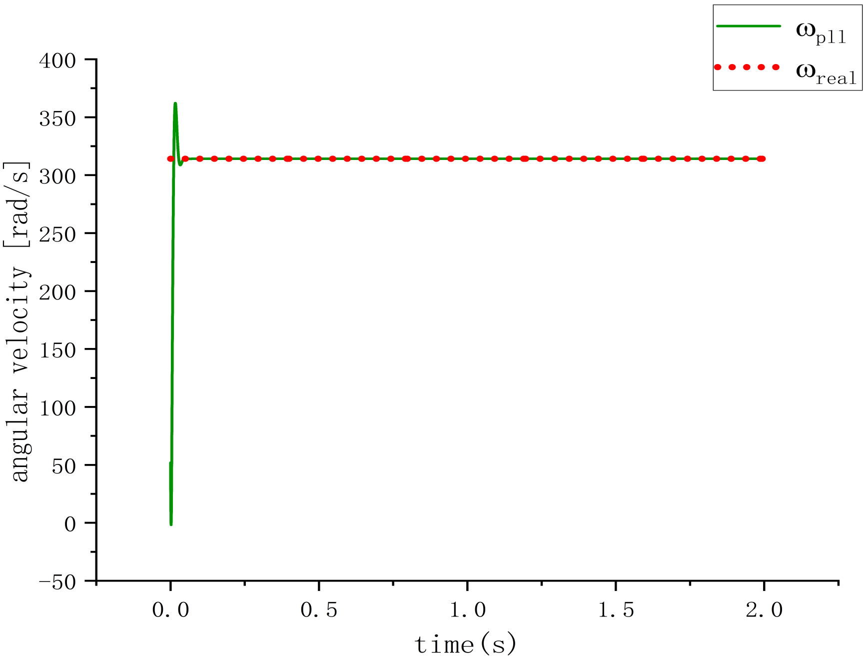

Figure 24: **Phase-locked loop tracking effect**

$$\frac{\mathrm{d}(K_{PLL})}{\mathrm{d}t} = \begin{bmatrix}0\end{bmatrix}\begin{bmatrix}V_d k_{p_{pll}} + w\end{bmatrix} + \begin{bmatrix}-k_{i_{pll}}\end{bmatrix}\begin{bmatrix}V_d\end{bmatrix} \tag{76}$$

$$w = [1][K_{PLL}] + [0][V_d] \tag{77}$$

As can be seen in Fig. 25, the linear results obtained from the state-space equation and the linear results obtained from the system simulation are the same, and the verification results are correct.

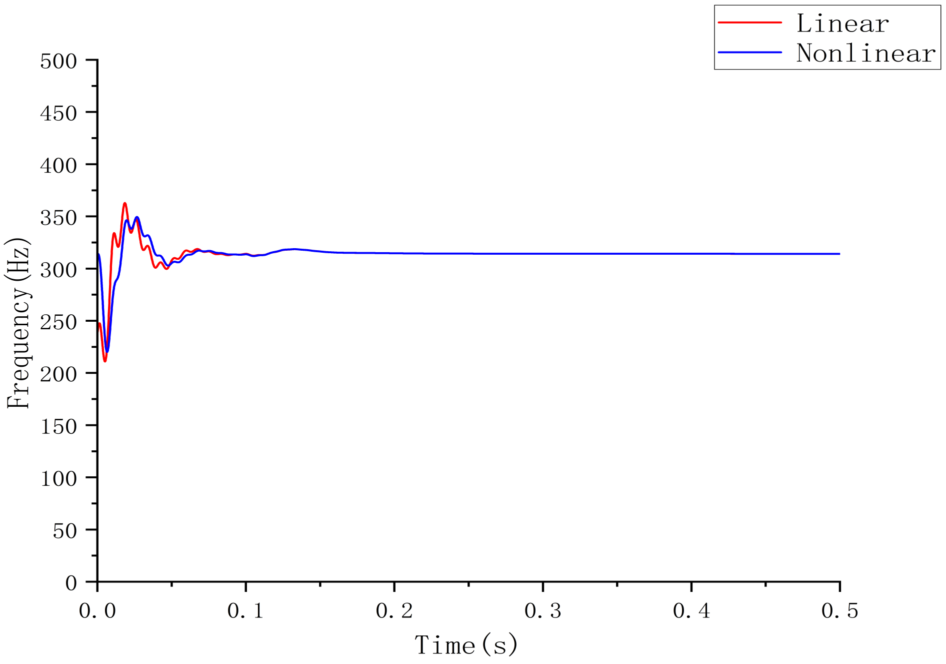

Figure 25: **Validation of PLL modules**

## 5.5 Current Loop Control

By assuming vzd = 0, equations from Eq. (54) can be written as

$$\begin{bmatrix} V_{zq} \\ 0 \end{bmatrix} - \begin{bmatrix} V_{lq} \\ V_{ld} \end{bmatrix} = \begin{bmatrix} r_l & -l_l w_e \\ l_l w_e & r_l \end{bmatrix} \begin{bmatrix} i_q \\ i_d \end{bmatrix} + \begin{bmatrix} l_l & 0 \\ 0 & l_l \end{bmatrix} \frac{d}{dt} \begin{bmatrix} i_q \\ i_d \end{bmatrix} \tag{78}$$

There is a coupling between the q and d components of the voltage and current. In order to control iq and id, the q and d components are decoupled and controlled independently.

Use Eq. (78) to decouple the q and d parts.

$$\begin{bmatrix} \hat{V_{lq}} \\ \hat{V_{ld}} \end{bmatrix} = \begin{bmatrix} -\hat{V_{lq}} + V_{zq} - l_l w_e i_{ld} \\ -\hat{V_{ld}} + l_l w_e i_{lq} \end{bmatrix} \tag{79}$$

where $\hat{V_{lq}}$ and $\hat{V_{ld}}$ are the outputs of the current controllers and vlq and vld are the voltages to be applied by the converter [4].

By substituting Eq. (79) into Eq.(78) and applying the Laplace transform, the transfer function between the controller voltage and the converter current can be derived as

$$\frac{i_q(s)}{V_{lq}\hat{}(s)} = \frac{1}{l_l s + r_l} \tag{80}$$

$$\frac{i_d(s)}{\hat{V_{ld}}(s)} = \frac{1}{l_l s + r_l} \tag{81}$$

Obtain a controller such as the following:

$$GIL(s) = \frac{K_p s + K_i}{s} \tag{82}$$

$$K_p = \frac{l_l}{\tau} \tag{83}$$

$$K_i = \frac{r_l}{\tau} \tag{84}$$

where $\tau$ is the closed-loop time constant of the electrical system. This constant must be chosen taking into account the physical limitations of the converter. It usually has to be a number of times faster than the switching frequency of the converter (e.g. 10).

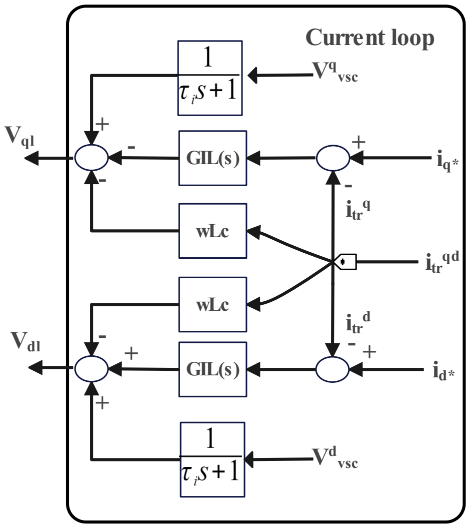

Figure 26: **Current loop of GFOL**

### 5.5.1 Current loop control state-space equation

According to Fig. 26, the following equation can be obtained:

$$v_{lq_{control}} = v_{zq_{control}} - wLI_{ld_{control}} - K_{P_{cur}}(I_{P_{ref}} - I_{lq_{control}}) - K_{i_{cur}} \int (I_{P_{ref}} - I_{lq_{control}}) \tag{85}$$

$$v_{ld_{control}} = v_{zd_{control}} + wLI_{lq_{control}} - K_{P_{cur}}(I_{Q_{ref}} - I_{ld_{control}}) - K_{i_{cur}} \int (I_{Q_{ref}} - I_{ld_{control}}) \tag{86}$$

The term "control" in the variable name indicates that the variable is obtained by applying a rotation matrix to its space-state form in the power system. $K_{P_{cur}}$ and $K_{i_{cur}}$ are control coefficients in GIL(s).

Set new variables to obtain the state-space equation more easily:$\int(I_{P_{ref}} - I_{lq_{control}}) = q_{Lq}$,$\int(I_{Q_{ref}} - I_{ld_{control}}) = q_{Ld}$.These two new variables are the state variables here.

The state-space equation of the current loop can be obtained as follows:

$$\begin{bmatrix} I_{P_{ref}} - I_{lq_{control}} \\ I_{Q_{ref}} - I_{ld_{control}} \end{bmatrix} = \begin{bmatrix} 0 & 0 \\ 0 & 0 \end{bmatrix} \begin{bmatrix} q_{Lq} \\ q_{Ld} \end{bmatrix} + \begin{bmatrix} 1 & 0 & 0 & 0 & 0 & 0 \\ 0 & 1 & 0 & 0 & 0 & 0 \end{bmatrix} \begin{bmatrix} I_{P_{ref}} - I_{lq_{control}} \\ I_{Q_{ref}} - I_{ld_{control}} \\ l_{q_{control}} \\ l_{d_{control}} \\ z_{q_{control}} \\ z_{d_{control}} \end{bmatrix} \tag{87}$$

$$\begin{aligned} \begin{bmatrix} v_{lq_{control}} \\ v_{ld_{control}} \end{bmatrix} &= \begin{bmatrix} -K_{i_{cur}} & 0 \\ 0 & -K_{i_{cur}} \end{bmatrix} \begin{bmatrix} q_{Lq} \\ q_{Ld} \end{bmatrix} \\ &+ \begin{bmatrix} -k_{p_{cur}} & 0 & -Lw & 0 & 1 & 0 \\ 0 & -k_{p_{cur}} & 0 & Lw & 0 & 1 \end{bmatrix} \begin{bmatrix} I_{P_{ref}} - I_{lq_{control}} \\ I_{Q_{ref}} - I_{ld_{control}} \\ l_{q_{control}} \\ l_{d_{control}} \\ z_{q_{control}} \\ z_{d_{control}} \end{bmatrix} \end{aligned} \tag{88}$$

As can be seen in Fig. 27 and28, the linear results obtained from the state-space equation and the results obtained from the system simulation are the same, and the verification results are correct and as expected.

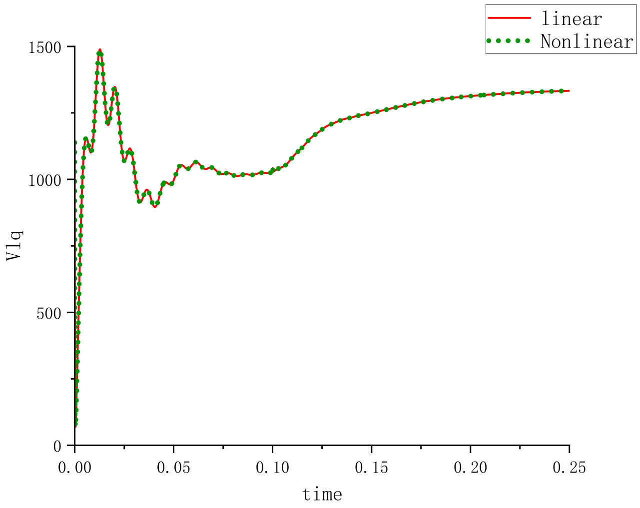

Figure 27: **Validation of Current loop**$(V_{lq})$

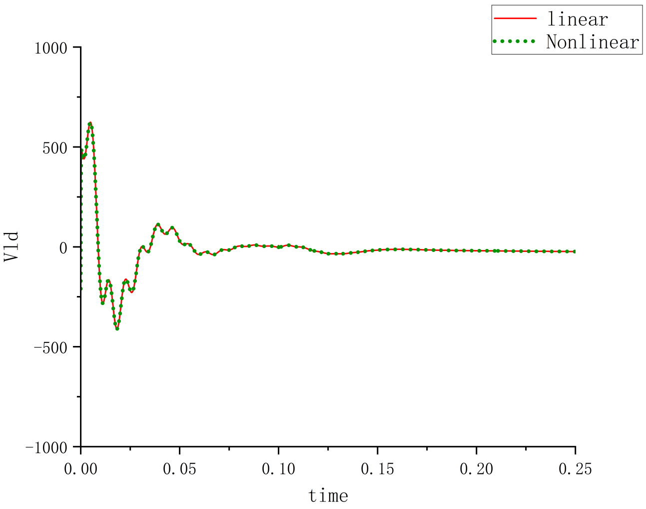

Figure 28: **Validation of Current loop**$(V_{ld})$

## 5.6 GFOL system simulation results

The system in the previous section describes a system with constant DC voltage, while the time constant $\tau$ of the current controller is set to 10 ms. The model in this section implements the control and tracking for active and reactive power, and in order to test the model performance, the reference values of active and reactive power are now set by setting the data in Table 1. The parameters of GFOL are shown in Table 2. The positive direction here is the grid feeding power to the converter side.

Table 1: Reference Active and reactive power of GFOL nonlinear systerm

| **Time instant** | **Active power [kW]** | **Reactive power [kVAr]** |
|---|---|---|
| 0 | -3 | 0 |
| 0.3 | -6 | -5 |
| 0.5 | -1 | 0 |
| 0.8 | -7 | 2 |
| 0.9 | -7 | -7 |

Table 2: GFOL System parameters

| Parameter | Value | Unit |
|---|---|---|
| Sbase | 2,75 | MVA |
| XR | 3 | ratio |
| SCR | 3 | |
| $V_{base}$ | 690 | V |
| $V_{dc}$ | 2000 | V |
| $R_{vsc}$ | 0,005 | pu |
| $L_{vsc}$ | 0,15 | pu |
| $Kp_{PLL}$ | 0,142 | |
| $Ki_{PLL}$ | 5,6817 | |
| $k_{pcc}$ | 0,8656 | |
| $Kp_{cc}$ | 0,0827 | |
| $Ki_{P/Q}$ | 0,01 | |
| $Kp_{P/Q}$ | 1,00E-05 | |
| $K_{droopP}$ | 1.7507e+05 | |
| $K_{droopQ}$ | 7.3218e+04 | |

The active power increases at t = 0.3s and t = 0.8s and decreases at t = 0.5s. The power converter can provide reactive power according to the active power. Between t = 0.3s and t = 0.5s, the system generates reactive power, and between t = 0.8s and t = 0.9, the power converter consumes reactive power.

The simulation results are shown in Fig. 29 to Fig. 36. As can be seen in Fig. 29 and 30, the model built in this section fully implements the tracking for both active and reactive power.

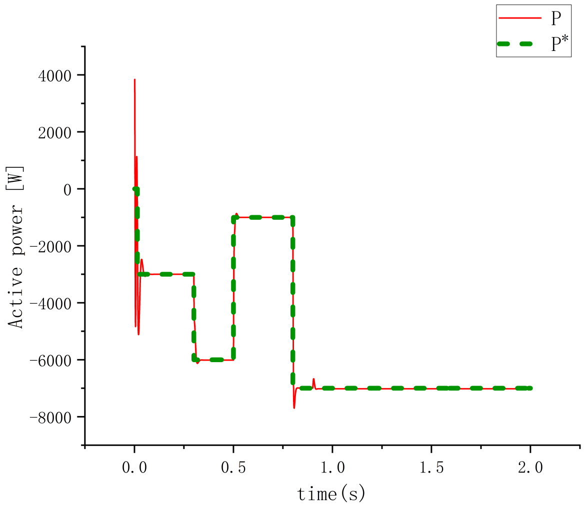

Figure 29: **Reference and measured active power P injected to the grid**

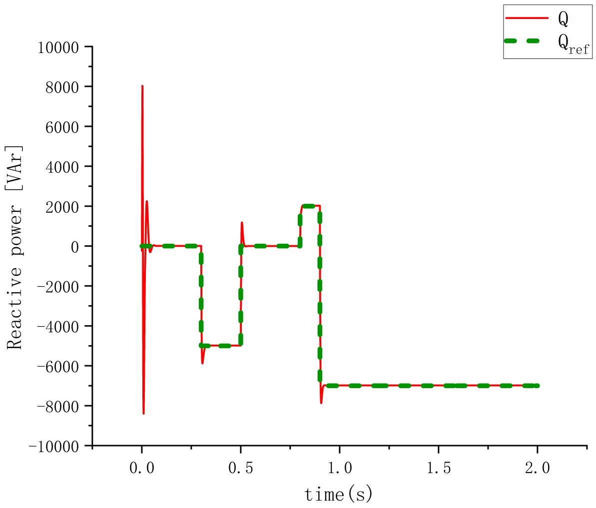

Figure 30: **Reference and measured reactive power Q injected to the grid**

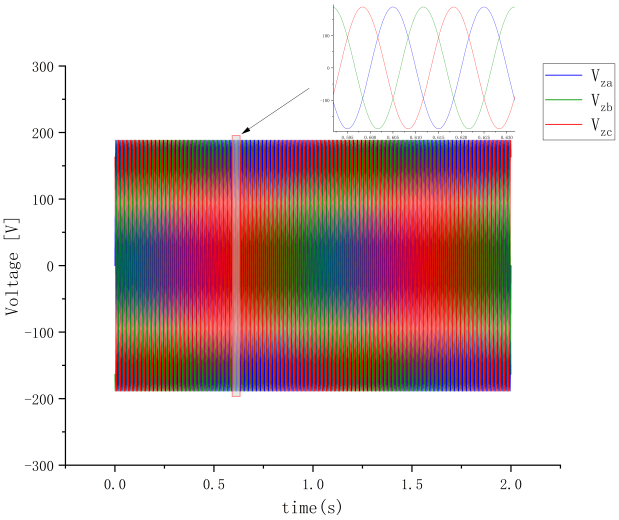

Figure 31: **Grid voltages in abc frames**

As can be seen in Fig. 32, the voltage at the power converter also increases between t=0.3-0.5s and t=0.9-1s due to the increase in the reactive power demand.

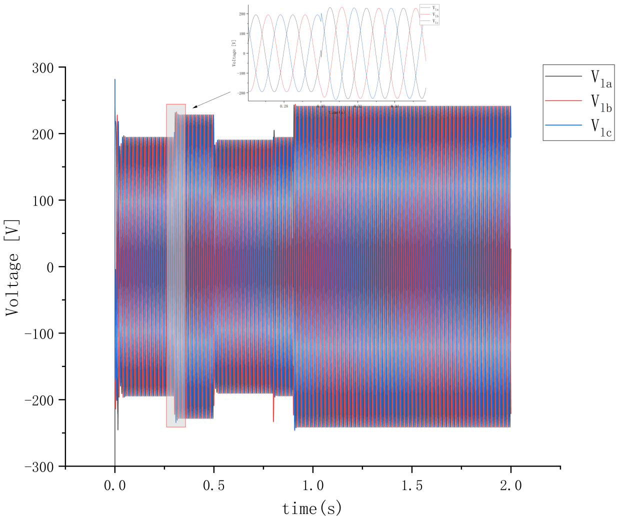

Figure 32: **Converter side voltage in abc frames**

From Fig. 33, it can be seen that the voltage at the converter changes in accordance with the law of Eq. (57) and (58), and the system changes the magnitude of iq and id in the circuit by adjusting the voltage at the converter to meet the demand of the system for active and reactive power regulation.

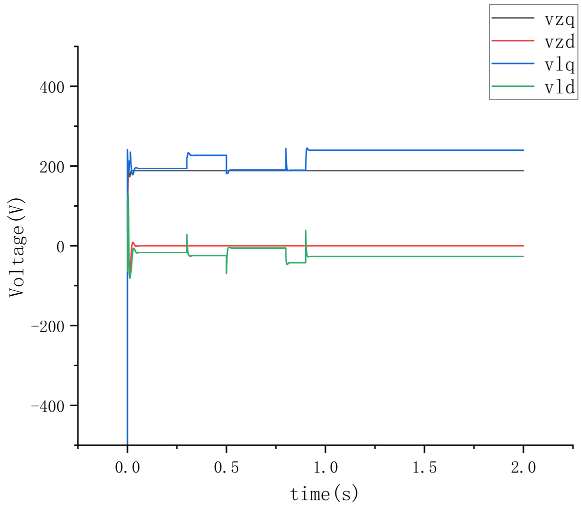

Figure 33: **Grid voltages and Converter side voltage in qd frames**

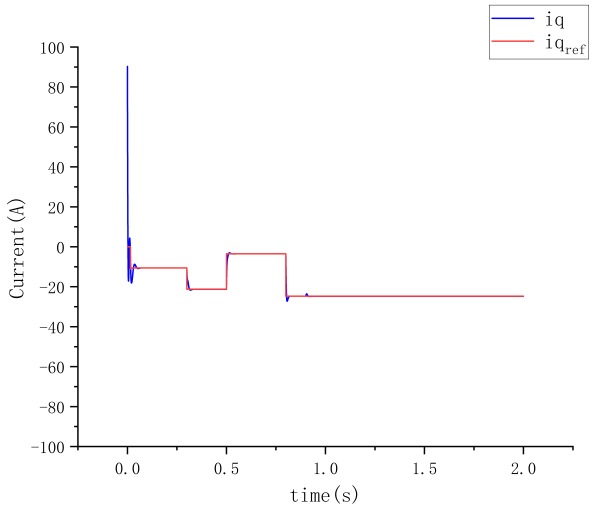

Figure 34: **Measured and reference currents in q frames**

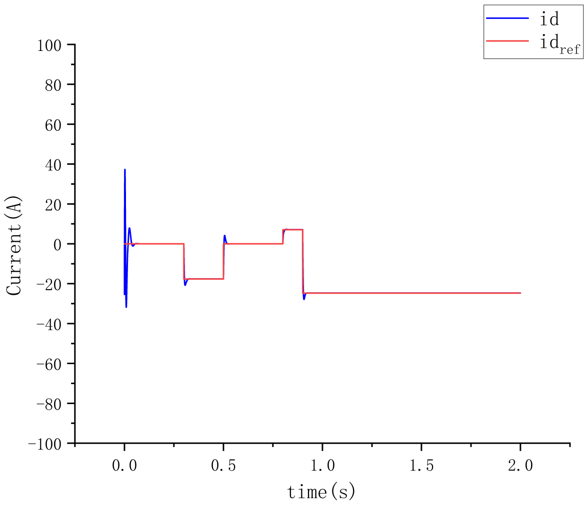

Figure 35: **Measured and reference currents in d frames**

Fig. 34and 35 show the measured and reference currents in the qd frame. The comparison between Fig. 29-30 and 34-35 shows the independent control of iq for active power and id for reactive power.

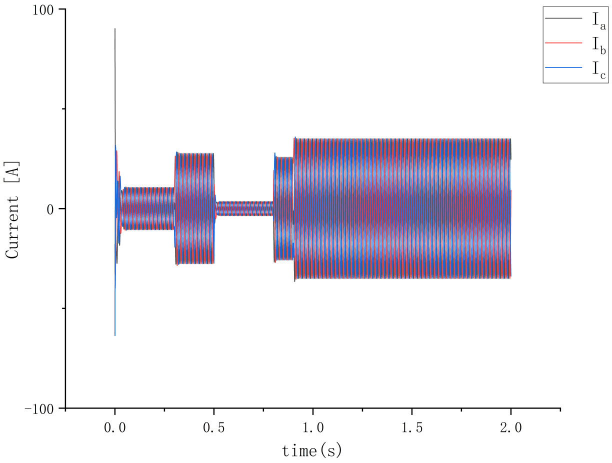

Figure 36: **Measured currents in the abc frames**

The Simulink model used to simulate GFOL is shown in Fig. 37.

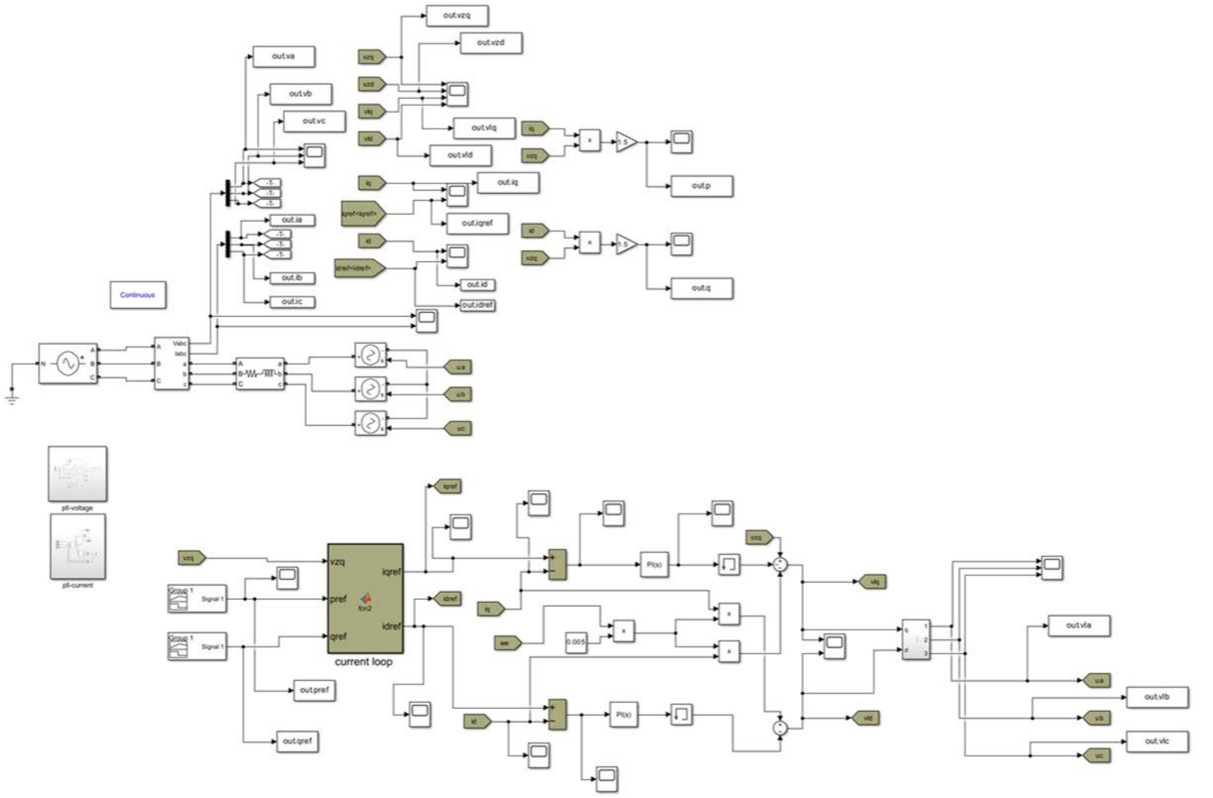

Figure 37: **Simulink model for simulating GFOL**

## 5.7 Modeling and verification of the state-space equation for components

In this section, the analysis of the linear model is discussed. In order to be able to perform follow-up stability analyses, the correctness of the linearised state-space model must be verified. In order to carry out such verification, a 1 percent Vpeak reference and a Thevenin voltage increase were applied for small signal perturbation verification, respectively, and the results are shown in Fig. 40 and 41.

After considering the state-space equations for the PI line, power supply, and each control module already available above, the state-space equations for the whole system can be constructed according to Fig. 38 to perform a small signal analysis at the end. The rotation matrix explained and derived above is used in this to compensate for the lack of consideration of electrical angles in the state-space equation. The model used for the analysis was constructed using the data in table 2.

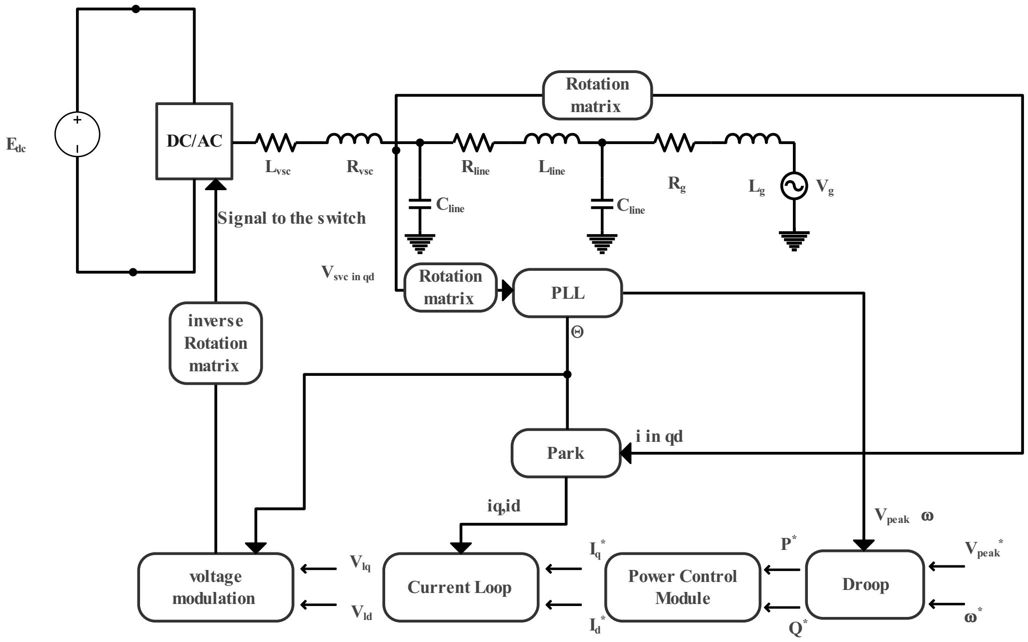

Figure 38: **GFOL linear model**

### 5.7.1 Converter

The converter and its filter can be considered as a voltage source in series with a resistor and an inductor. As shown in Fig. 39. According to this, the relevant state-space equation can be obtained.

$$\begin{bmatrix} \frac{dI}{dt} \\ \frac{dI}{dt} \end{bmatrix} = \begin{bmatrix} -\frac{R}{L} & -w \\ w & -\frac{R}{L} \end{bmatrix} \times \begin{bmatrix} I \\ I \end{bmatrix} + \begin{bmatrix} 1/L & 0 & -1/L & 0 \\ 0 & 1/L & 0 & -1/L \end{bmatrix} \times \begin{bmatrix} V_{qsource} \\ V_{dsource} \\ V_{1q} \\ V_{1d} \end{bmatrix} \tag{89}$$

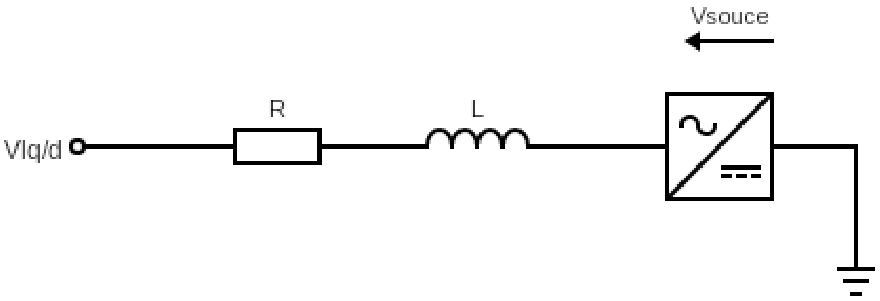

Figure 39: **Converter**

### 5.7.2 Model Validation Result

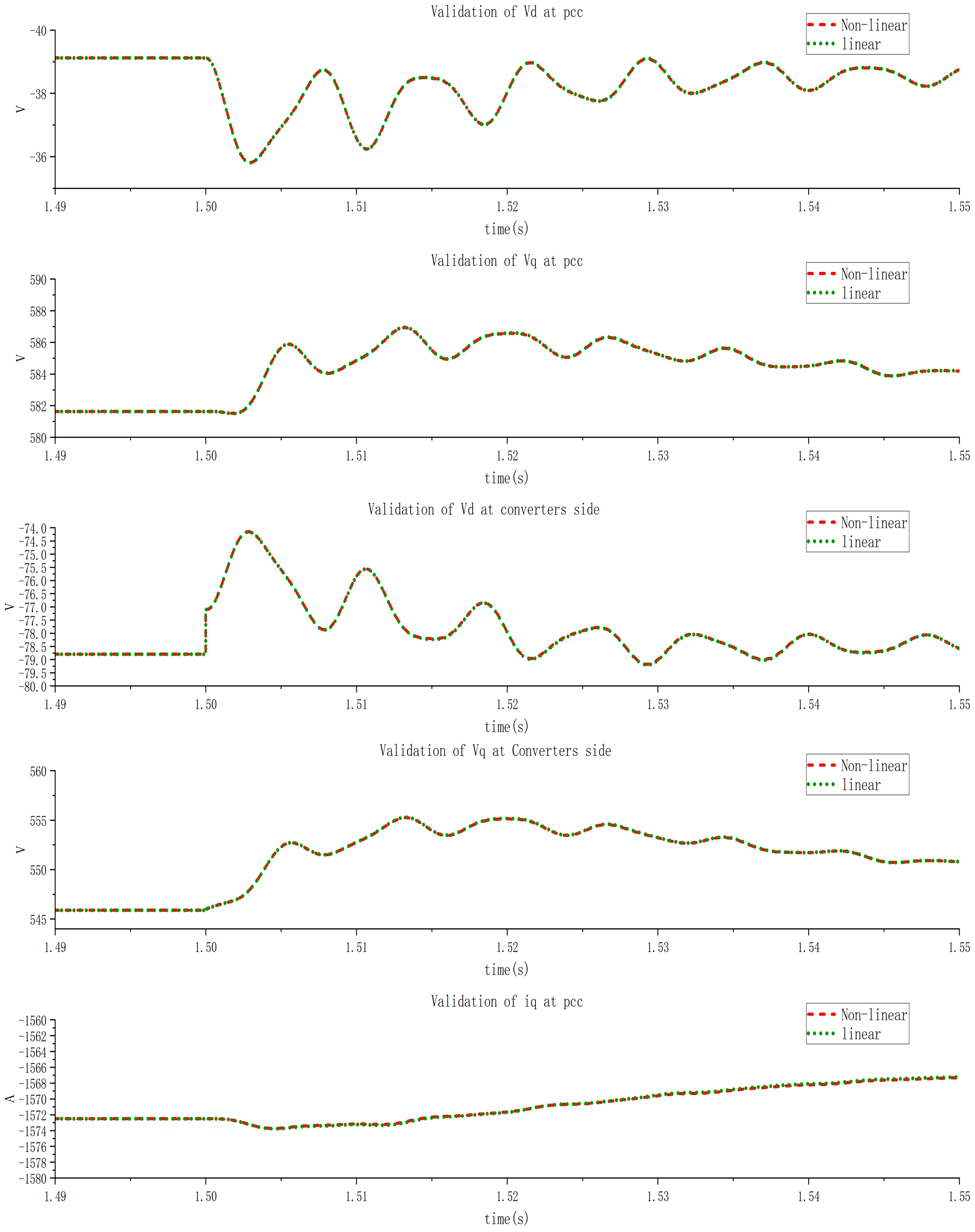

Figure 40: **Comparison of linear and nonlinear models of GFOL when 1 percent of the $V_{peak}$ variation is used as a perturbation**

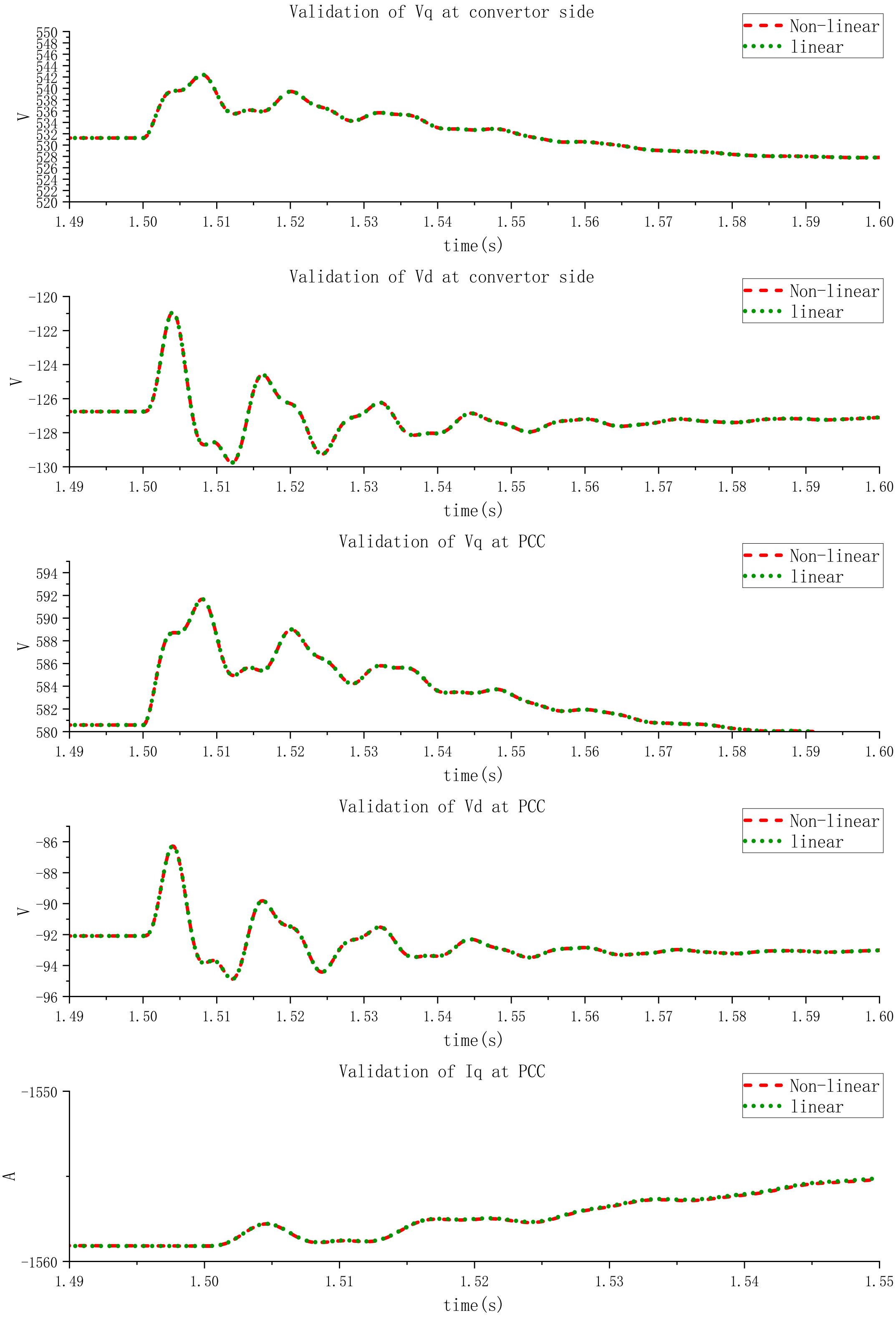

Figure 41: **Comparison of linear and nonlinear models of GFOL when 1 percent of the Thevenin voltage increment is used as a perturbation**

# 6 GFOR system modeling and state-space equation modeling

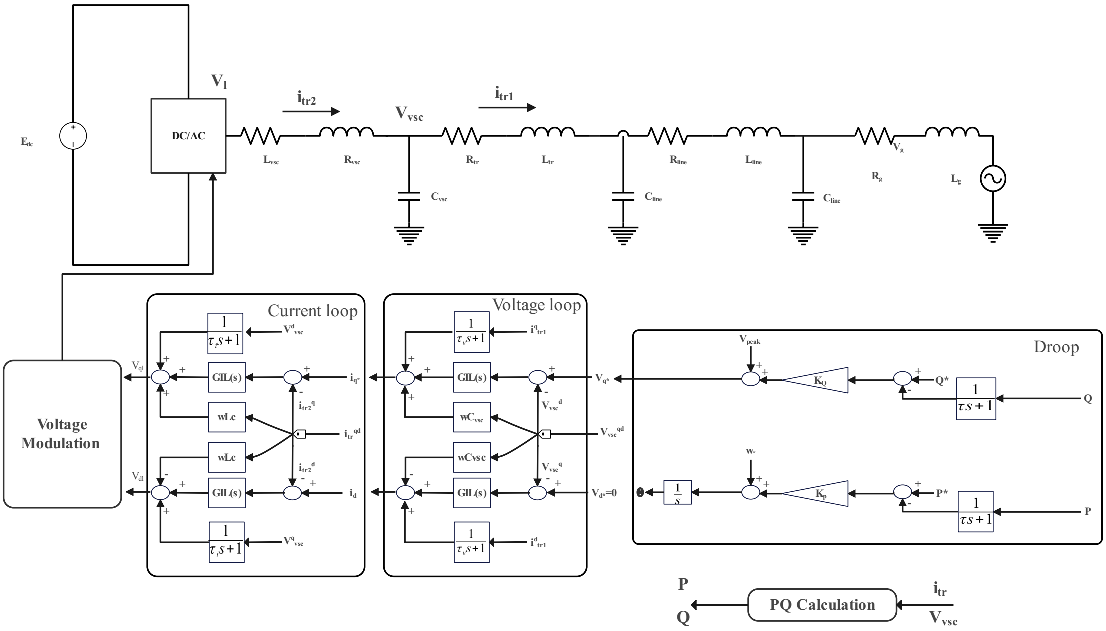

Figure 42: **Grid Forming control scheme**

Inverter-based resources (IBRs) are increasingly common in power systems. Despite the growing share of IBRs, traditional synchronous generator-based voltage, and frequency control mechanisms are still prevalent in the power industry. As a result, there is a growing need for IBRs to mimic the behavior of synchronous generators, which traditional grid-following inverters (GFOL) struggle to meet. As a solution, the GFOR concept is now emerging and it is attracting increasing interest from academia and industry [30].

## 6.1 Droop control

Droop control is the simplest implementation of the swing equation. The main idea is to measure active and reactive power and to use the variation of the measured power flow to provide set points for voltage controllers. Droop control has historically been implemented in microgrids, introducing the possibility of several converters operating in parallel and forming a grid together [30].

Synchronization is based on the droop characteristic, where the output frequency of the converter is linearly adjusted according to the active power flow. This can be expressed as

$$\omega = \omega^* - mP \tag{90}$$

where $\omega^*$ is the nominal frequency and m is the droop gain. Fig. 43 illustrates the droop behavior. If the active power transfer is zero, the reference frequency is used, but if there is a positive output power transfer, the converter frequency is reduced to reduce this power transfer and restore synchronization [31].

It is also possible to modify Eq. (90) by instead using the perpendicular gain of $P_{error}$ = $P^*$-P to obtain the following perpendicular equation

$$\omega = \omega^* - m(P^* - P) \tag{91}$$

where $P^*$ is the reference power and P is the measured power at POC or PCC. The same principle as explained above can be used for reactive power control. By adding a falling gain to the measured reactive power, the voltage amplitude can be adjusted to control the reactive power flow.

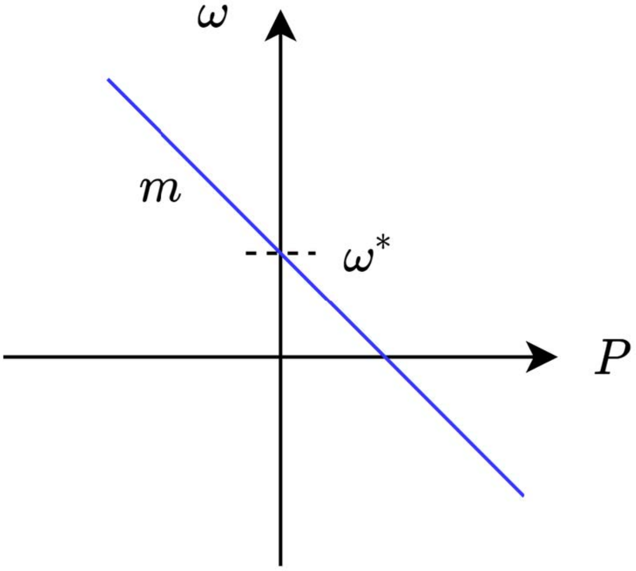

Figure 43: **Graphical representation of the droop law**

$$V_{poc} = V_{poc}^* - n(Q^* - Q) \tag{92}$$

where $V_{poc}^*$ is the nominal output voltage and n is a static droop gain. Based on the above principles, a droop control structure is built as shown in Fig. 44.

The state-space equation Eq. (93) and (94) for the droop section is built from Fig. 44:

$$V_q^* = \begin{bmatrix} K_Q & -K_Q & 1 \end{bmatrix} \begin{bmatrix} Q^* \\ Q \\ V_{peak} \end{bmatrix} \tag{93}$$

$$\omega = \begin{bmatrix} K_P & -K_P & 1 \end{bmatrix} \begin{bmatrix} P^* \\ P \\ \omega^* \end{bmatrix} \tag{94}$$

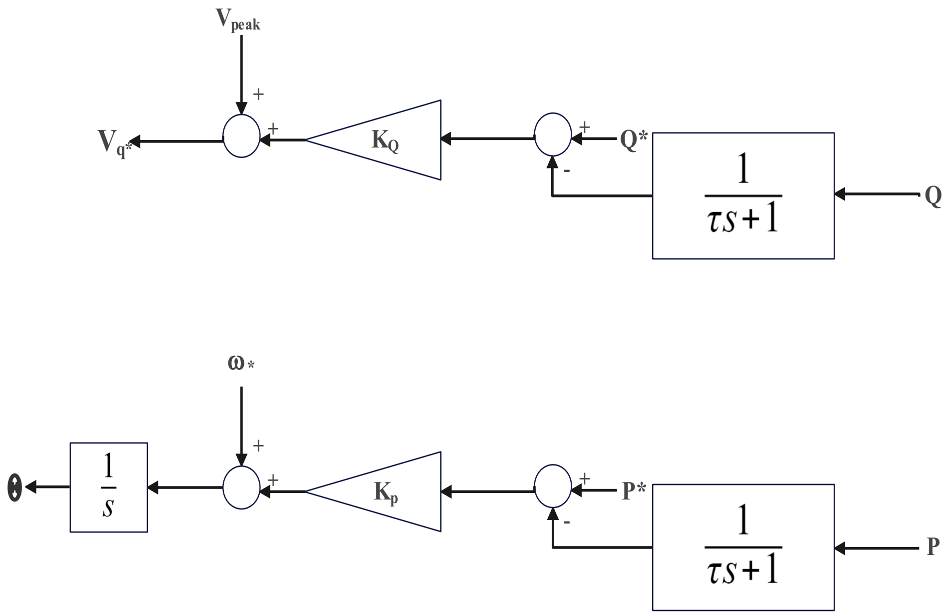

Figure 44: **GFOR's Droop control scheme**

$$\theta = [1] \times [\theta] + [0] \times [\omega] \tag{95}$$

where $V_{peak}$ and $\omega^*$ are the measured voltage and frequency at the POC, $Q^*$ and $P^*$ are the reference active and reactive power sets for the system and represent the power transferred from the converter side to the grid side. P and Q are the measured active and reactive power values of the system obtained from the energy calculation module by processing the voltage and current measured at the PCC.

## 6.2 Voltage control loop

The reference voltage values obtained above are fed into the voltage loop to obtain the corresponding reference current values. The currents and voltages used in the voltage loop are taken from the PCC point.

According to Fig. 45, the following equation can be obtained:

$$(V_q^* - V_{vsc}^d) \times (Kp_{vc} + \frac{Ki_{vc}}{s}) + wCV_{vsc}^d + i_{tr}^q = i_q^* \tag{96}$$

$$(V_d^* - V_{vsc}^q) \times (Kp_{vc} + \frac{Ki_{vc}}{s}) - wCV_{vsc}^q + i_{tr}^d = i_d^* \tag{97}$$

Eq. (98)-(103) represents the state-space equation of the voltage loop for the currents on the q and d axes respectively.

$$\triangle_{vq} = i_q^* - i_{tr}^q - wCV_{vsc}^d - (V_q^* - V_{vsc}^d) \times Kp_{vc} \tag{98}$$

$$\frac{\mathrm{d}\triangle_{vq}}{\mathrm{d}t} = [0]\,\triangle_{vq} + \begin{bmatrix} Ki_{vc} & 0 & 0 \end{bmatrix} \begin{bmatrix} (V_q^* - V_{vsc}^d) \\ V_{vsc}^d \\ i_{tr}^q \end{bmatrix} \tag{99}$$

$$i_q^* = \begin{bmatrix} 1 \end{bmatrix} \triangle_{vq} + \begin{bmatrix} Kp_{vc} & wC & 1 \end{bmatrix} \begin{bmatrix} (V_q^* - V_{vsc}^d) \\ V_{vsc}^d \\ i_{tr}^q \end{bmatrix} \tag{100}$$

$$\triangle_{vd} = i_d^* - i_{tr}^d + wCV_{sc}^q - (V_d^* - V_{vsc}^q) \times Kp_{vc} \tag{101}$$

$$\frac{\mathrm{d}\triangle_{vd}}{\mathrm{d}t} = [0]\,\triangle_{vd} + \begin{bmatrix} Ki_{vc} & 0 & 0 \end{bmatrix} \begin{bmatrix} (V_d^* - V_{vsc}^q) \\ V_{vsc}^q \\ i_{tr}^d \end{bmatrix} \tag{102}$$

$$i_d^* = \begin{bmatrix} 1 \end{bmatrix} \triangle_{vd} + \begin{bmatrix} Kp_{vc} & -wC & 1 \end{bmatrix} \begin{bmatrix} (V_d^* - V_{vsc}^q) \\ V_{vsc}^q \\ i_{tr}^d \end{bmatrix} \tag{103}$$

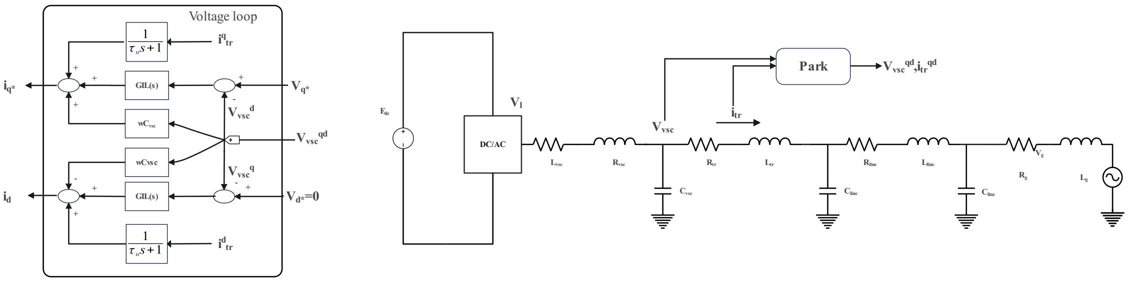

Figure 45: **GFOR's Voltage control loop control scheme**

## 6.3 Current control loop

The previously obtained reference current values are fed into the current loop to obtain the corresponding reference voltage values. The voltage used in the current loop is taken from the PCC point and the current is taken after the inductance of the converter filter.

According to Fig. 45, the following equation can be obtained:

$$\triangle_{iq} = v_q^* - v_{vsc}^q - wLtr^d - (i_q^* - i_{tr}^d) \times Kp_{cc} \tag{104}$$

$$\triangle_{id} = v_d^* - v_{vsc}^d + wLtr^q - (i_d^* - i_{tr}^q) \times Kp_{cc} \tag{105}$$

$$(i_q^* - i_{tr}^d) \times (Kp_{cc} + \frac{Ki_{cc}}{s}) + wLi_{tr}^d + v_{vsc}^q = V_{lq}^* \tag{106}$$

$$(i_d^* - i_{tr}^q) \times (Kp_{cc} + \frac{Ki_{cc}}{s}) - wLi_{tr}^q + V_{vsc}^d = V_{ld}^* \tag{107}$$

The Eq. (108)- (111) represents the state-space equation of the current loop for the voltages on the q-axis and d-axis respectively.

$$\frac{\mathrm{d}\triangle_{iq}}{\mathrm{d}t} = [0]\,\triangle_{iq} + \begin{bmatrix} Ki_{cc} & 0 & 0 \end{bmatrix} \begin{bmatrix} (i_q^* - i_{tr}^d) \\ i_{tr}^d \\ V_{vsc}^q \end{bmatrix} \tag{108}$$

$$V_{lq}^* = \begin{bmatrix} 1 \end{bmatrix} \triangle_{iq} + \begin{bmatrix} Kp_{cc} & wL & 1 \end{bmatrix} \begin{bmatrix} (i_q^* - i_{tr}^d) \\ i_{tr}^d \\ V_{vsc}^q \end{bmatrix} \tag{109}$$

$$\frac{\mathrm{d}\triangle_{id}}{\mathrm{d}t} = [0]\,\triangle_{id} + \begin{bmatrix} Ki_{cc} & 0 & 0 \end{bmatrix} \begin{bmatrix} (i_d^* - i_{tr}^q) \\ i_{tr}^q \\ V_{vsc}^d \end{bmatrix} \tag{110}$$

$$V_{ld}^* = \begin{bmatrix} 1 \end{bmatrix} \triangle_{id} + \begin{bmatrix} Kp_{cc} & -wL & 1 \end{bmatrix} \begin{bmatrix} (i_d^* - i_{tr}^q) \\ i_{tr}^q \\ V_{vsc}^d \end{bmatrix} \tag{111}$$

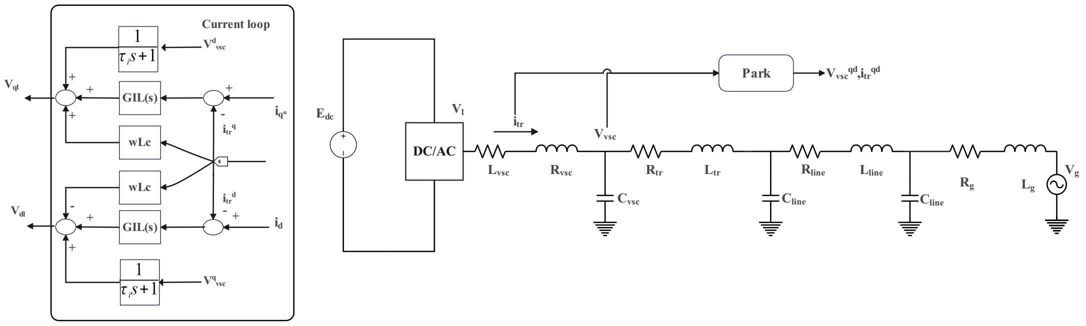

Figure 46: **GFOR’s Current control loop concept drawing**

## 6.4 GFOR system simulation results

The objective of this section is to test the accuracy of the GFOR model, and for this purpose, the reference active power increases at t = 2s, and the reference reactive power increases at t = 1s.

The simulation results are shown in Fig. 47 to Fig. 50. As can be seen in Fig. 47, the model built in this section fully implements the tracking for active power.

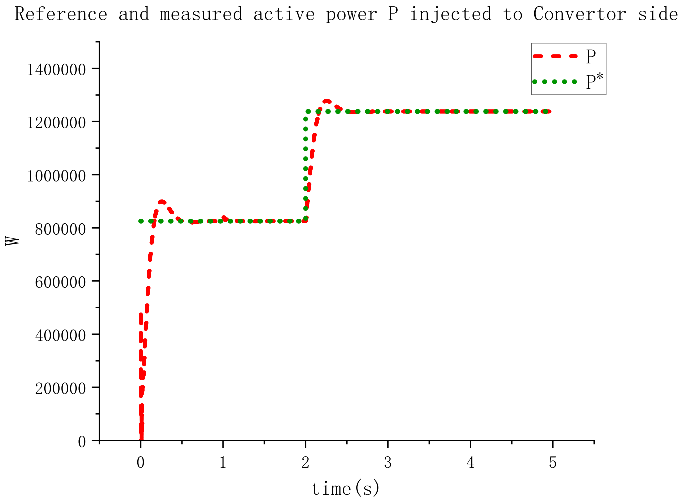

Figure 47: **Reference and measured active power P injected to convertor side**

Fig. 48 and 49 show the measured and reference currents in the qd frame.

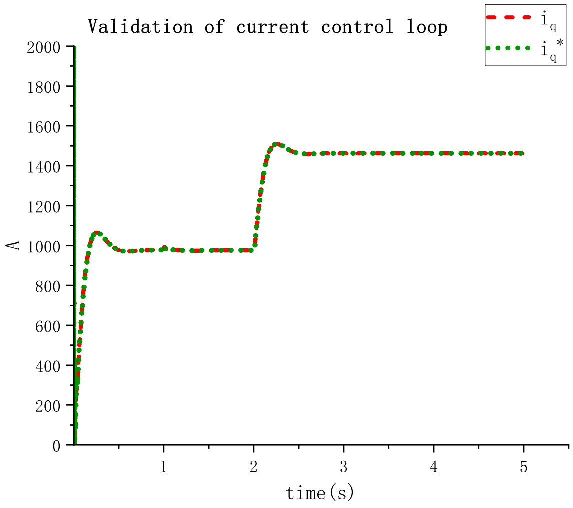

Figure 48: **Measured and reference currents in q frames**

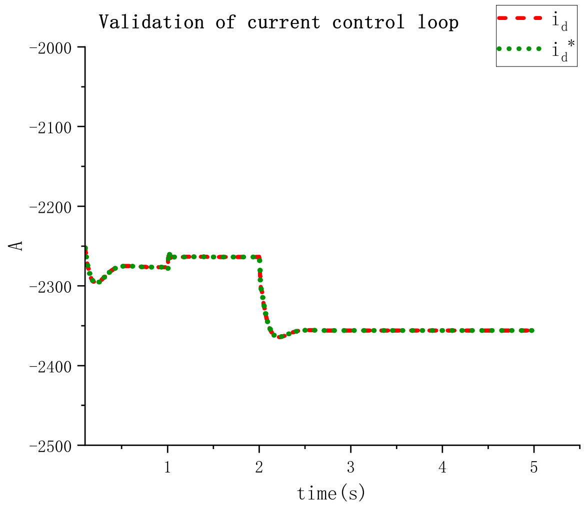

Figure 49: **Measured and reference currents in d frames**

Fig. 50 show the measured and reference voltage in the q frame.

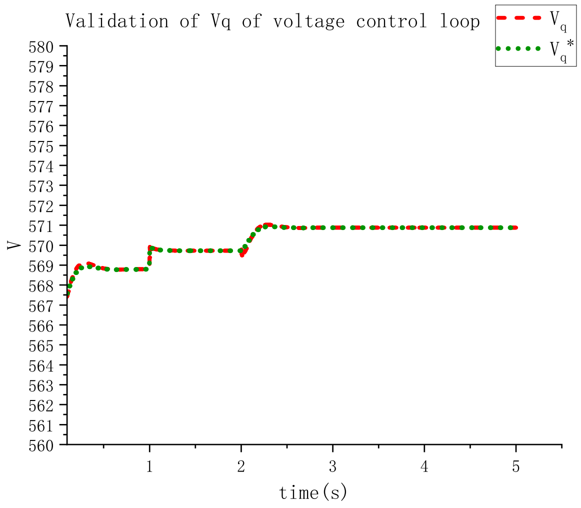

Figure 50: **Measured and reference voltage in q frames**

The Simulink model used to simulate GFOR is shown in Fig. 51.

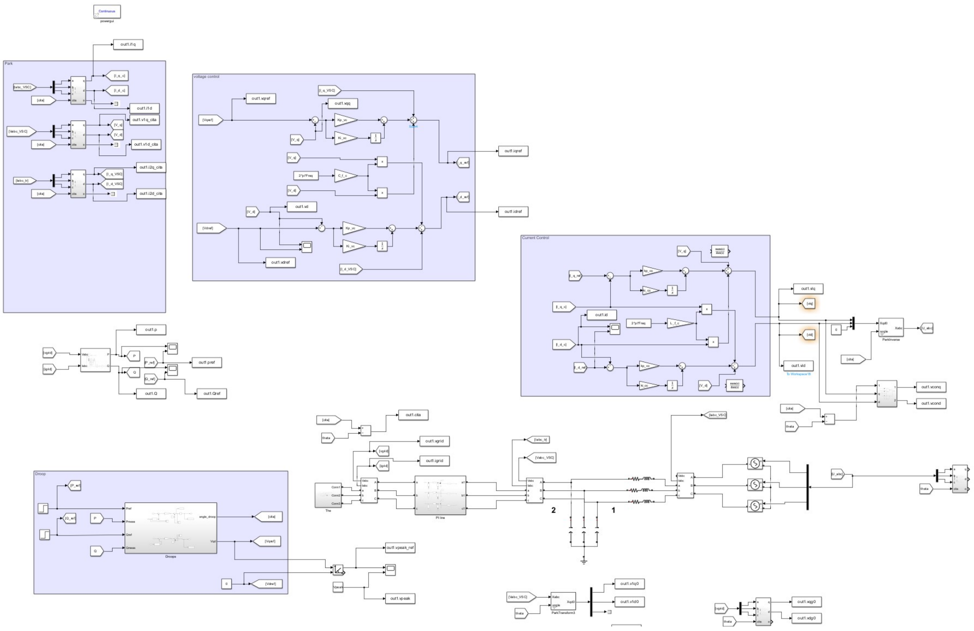

Figure 51: **Simulink model for simulating GFOR**

## 6.5 Modeling and verification of the state-space equation for components

In this section, the analysis of the linear model is discussed. In order to be able to perform follow-up stability analyses, the correctness of the linearised state-space model must be verified. In order to carry out such verification, a 1 percent power reference and a Thevenin voltage increase were applied for small signal perturbation verification, respectively, and the results are shown in Fig. 53 and 54.

The whole system can be constructed according to Fig. 52 to perform a small signal analysis at the end. The rotation matrix explained and derived above is used in this to compensate for the lack of consideration of electrical angles in the state-space equation. The model used for the analysis was constructed using the data in table 3.

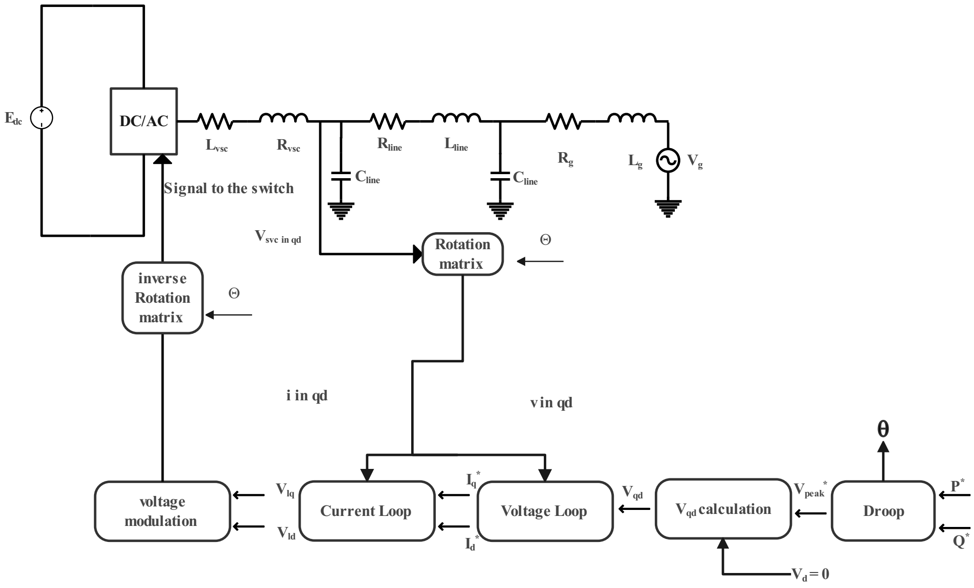

Figure 52: **GFOR Linear Model**

Table 3: GFOR System parameters

| Parameter | Value | Unit |
|---|---|---|
| Sbase | 2,75 | MVA |
| XR | ratio | 3 |
| SCR | 3 | |
| $V_{base}$ | 690 | V |
| $V_{dc}$ | 2000 | V |
| $R_{vsc}$ | 0,005 | pu |
| $L_{vsc}$ | 0,15 | pu |
| $R_{tr}$ | 0,0005 | pu |
| $L_{tr}$ | 0,015 | pu |
| $Kp_{vc}$ | 4.789 | |
| $Ki_{vc}$ | 42.05 | |
| $k_{pcc}$ | 0,8656 | |
| $Kp_{cc}$ | 0,0827 | |
| $Ki_{P/Q}$ | 0,01 | |
| $Kp_{P/Q}$ | 1,00E-05 | |
| $Kp_{P/Q}$ | 1,00E-05 | |
| $K_{droopf}$ | 1,14E-06 | |
| $K_{droopu}$ | 1,37E-05 | |

### 6.5.1 Model Validation Result

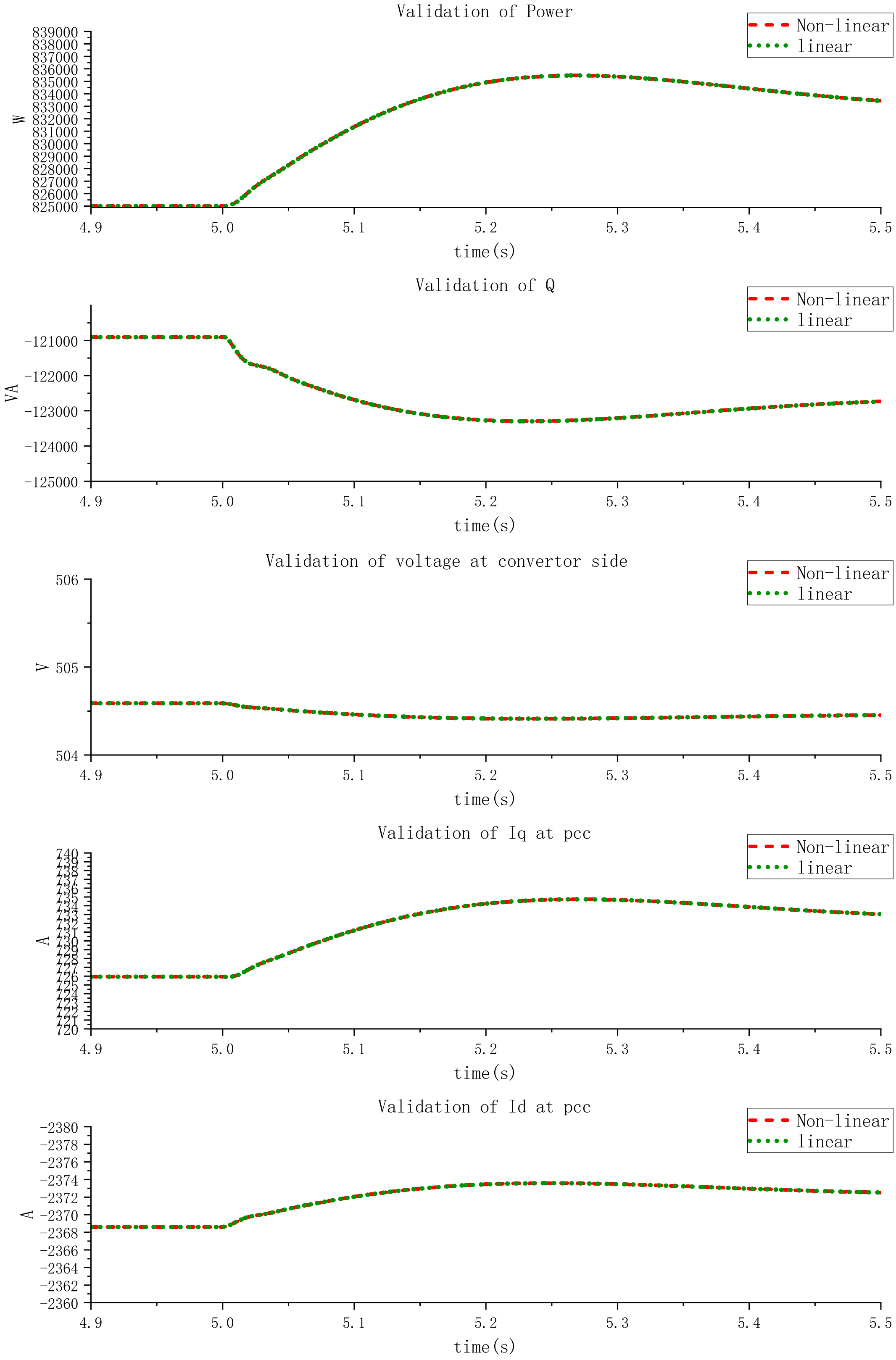

Figure 53: **Comparison of linear and nonlinear models of GFOL with1 % increase on the power reference**

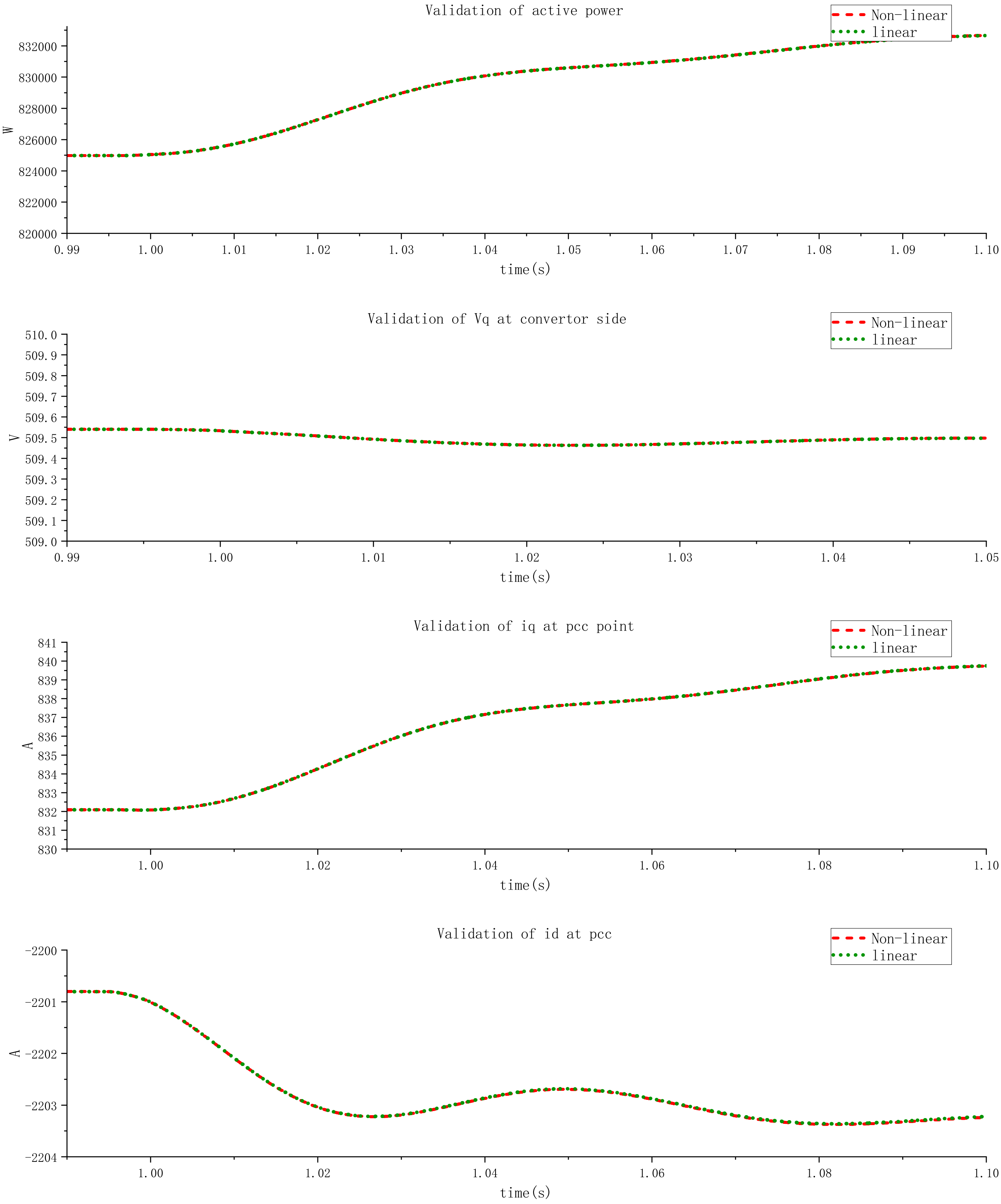

Figure 54: **Comparison of linear and nonlinear models of GFOL with1 % increase on the tehvenin voltage**

# 7 Stability Analysis

Eigenvalues and PF are conventional tools used to analyze the effects of oscillatory modes in power system stability [2]. The eigenvalues are obtained from the diagonalization of the state matrix A, which provides the frequencies and damping ratios of the modes.

Unstable eigenvalues are associated with negative damping, while positive values close to zero are identified as potential modes that can be destabilized under different operating conditions or control parameters.

PFs are used to define the relative relationship between state variables and modes [2]. Thus, the participation matrix can be defined as follows

$$P = [P_1, P_2, \ldots\ldots, P_n]; P_i = [p_{1i}, p_{2i}, \ldots\ldots, p_{2i}]^T \tag{112}$$

where i, j = 0,...,n of $p_{ji}$ is the PF of state variable j in mode i. PFs $p_{ji}$ provide a measure of the contribution of the state variable to each mode and vice versa.

PFs can provide an indication of the interactions between the components of a power system. State variables can be grouped according to their associated components [32]. Interactions can then be identified when a model has the participation of state variables from different components. However, if the coupling effects between components do not have any associated state variables, then PF may not be used to identify interactions.

In this section, the stability results of the system will be analyzed by looking at the eigenvalues and the participation factor (PF). From the eigenvalues obtained, the damping ratio and oscillation frequency of the mode can be calculated and the stability of the mode can be observed. If the real part of all the eigenvalues is negative, the system can be said to be stable. Another theory is that low damping modes are critical poles and that negative damping modes occur as instabilities. In addition, the location of the poles is also critical. If the real part of the pole is close to the origin, then changes in certain parameters of the system may cause the real part of that pole to become positive and thus cause the system to become unstable.

## 7.1 Stability Analysis of grid forming system

The GFOR model constructed from the data in Table 3 has been validated and the following values of oscillation frequency, damping ratio, and participation coefficient can be obtained by using the matrix eigenvalues of the GFOR model for analytical calculations.

Table 4 indicates the poles, frequencies, and damping ratios for each mode of the GFOR, for a total of 21 modes. We can see that the damping ratios of all modes are higher than 0.3. In addition, modes 17-21 are close to the origin, so they are sensitive to changes in parameters, but they are highly damped. There are also modes with a damping ratio of 1. They have no imaginary part, so they do not show oscillatory behavior.

Table 4: Real, Imaginary, Frequency and Damping ratio of each mode

| Mode | Real | Imaginary | Frequency | $\xi$ |
|---|---|---|---|---|
| 1 | -28978.6198 | 88353.2288 | 14061.8531 | 0.8997 |
| 2 | -28978.6198 | -88353.2288 | 14061.8531 | 0.8997 |
| 3 | -28978.6198 | 87724.9103 | 13961.8531 | 0.9009 |
| 4 | -28978.6198 | -87724.9103 | 13961.8531 | 0.9009 |
| 5 | -435.9099 | 7936.7646 | 1263.1753 | 0.3262 |
| 6 | -435.9099 | -7936.7646 | 1263.1753 | 0.3262 |
| 7 | -435.8200 | 7315.7438 | 1164.3368 | 0.3506 |
| 8 | -435.8200 | -7315.7438 | 1164.3368 | 0.3506 |
| 9 | -139.7574 | 1181.8826 | 188.1025 | 0.5964 |
| 10 | -139.7574 | -1181.8826 | 188.1025 | 0.5964 |
| 11 | -107.7017 | 695.9387 | 110.7621 | 0.6971 |
| 12 | -107.7017 | -695.9387 | 110.7621 | 0.6971 |
| 13 | -34.5707 | 149.5782 | 23.8061 | 0.8236 |
| 14 | -34.5707 | -149.5782 | 23.8061 | 0.8236 |
| 15 | -59.8931 | 0.0000 | 0.0000 | 1.0000 |
| 16 | -36.5474 | 0.0000 | 0.0000 | 1.0000 |
| 17 | -13.7435 | 0.0000 | 0.0000 | 1.0000 |
| 18 | -8.1796 | 0.0000 | 0.0000 | 1.0000 |
| 19 | -9.5274 | 0.6533 | 0.1040 | 0.9999 |
| 20 | -9.5274 | -0.6533 | 0.1040 | 0.9999 |
| 21 | -10.4720 | 0.0000 | 0.0000 | 1.0000 |

The graphical form of the eigenvalues of the system is shown in Fig. 55.

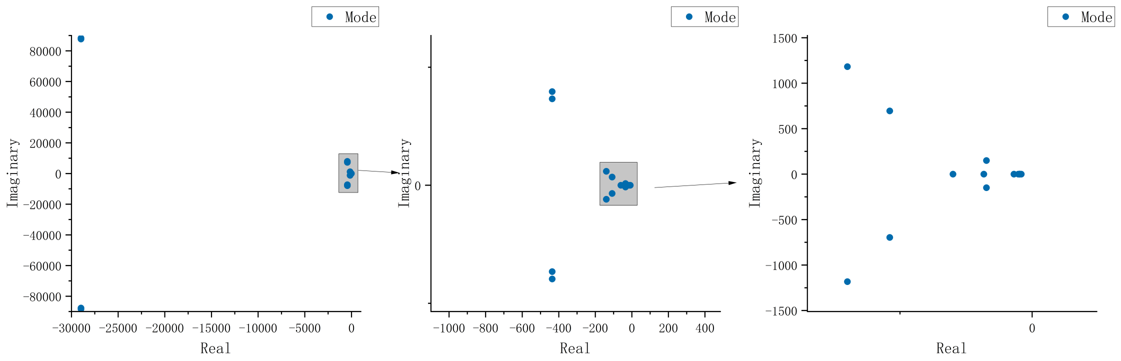

Figure 55: **Eigenvalues of the system with GFOL**

### 7.1.1 Table of Participation Factors of GFOR

To further investigate from which system components different poles originate, the tool of participation factors is applied. Participation factors provide a measure of the participation between state variables and poles.

The state-space model consists of 21 states in total. Note that it requires two states to capture both the d- and q-component and that some system components may have two inputs, hence several states are required for one state-space representation of such a system component.

Based on the results in Fig. 56, the state variables can be grouped into the following clusters:

- Group 1: Voltage control $v_d$,$v_q$
- Group 2: Current control $i_d$,$i_q$
- Group 3: Q droop control,$KQ_{droop}$
- Group 4: P droop control,$KP_{droop}$ and cita
- Group 5: Thevenin grid $I_{dTH}$,$I_{qTH}$
- Group 6: PI line $V_{pi1q}$ ,$V_{pi1d}$ ,$V_{pi2q}$ ,$V_{pi2q}$ ,$I_{piq}$,$I_{pid}$
- Group 7: Transformer $I_{trd}$ ,$I_{trq}$
- Group 8: Converter side $I_{vscq}$ ,$I_{vscd}$,$V_{vscq}$ ,$V_{vscd}$

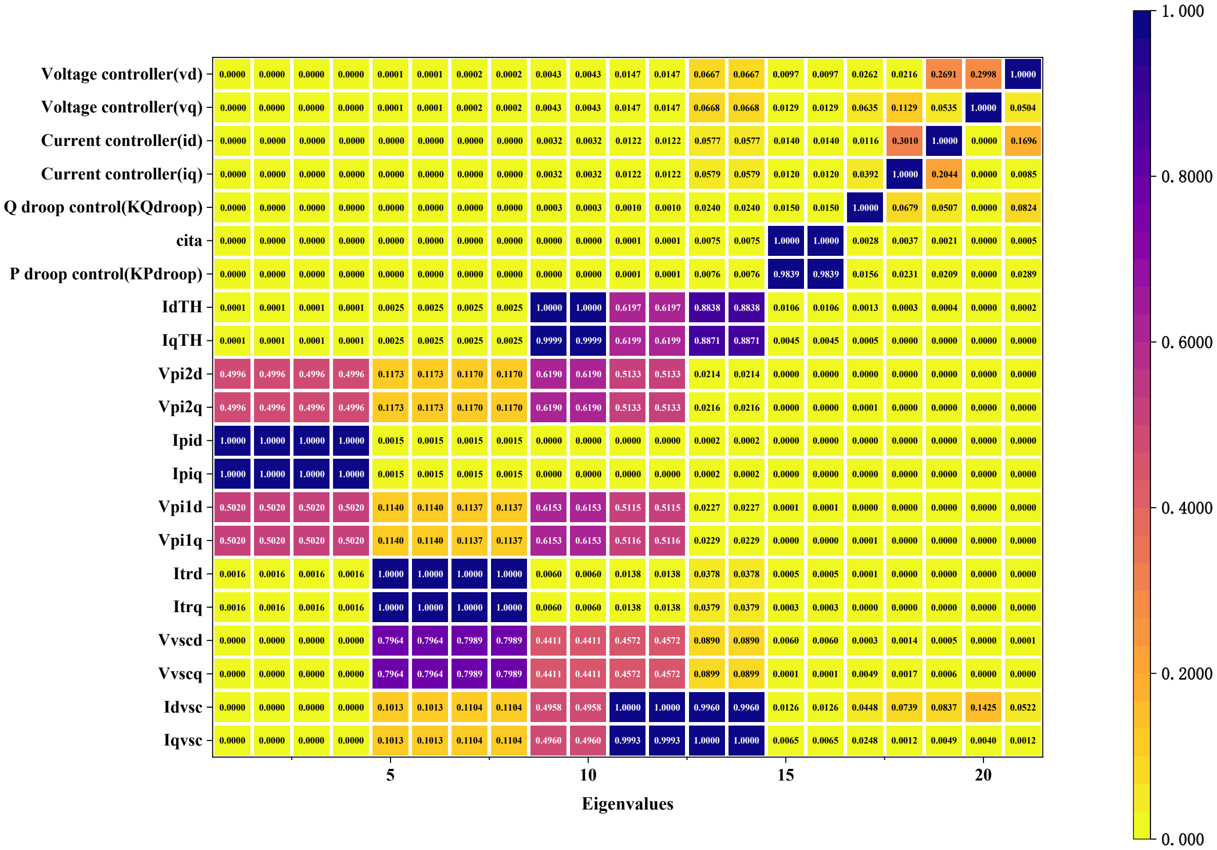

| | | | | | | | | | | | | | | | | | | | | | |
|---|---|---|---|---|---|---|---|---|---|---|---|---|---|---|---|---|---|---|---|---|---|
| Voltage controller(vd) | 0.0000 | 0.0000 | 0.0000 | 0.0000 | 0.0001 | 0.0001 | 0.0002 | 0.0002 | 0.0043 | 0.0043 | 0.0147 | 0.0147 | 0.0667 | 0.0667 | 0.0097 | 0.0097 | 0.0262 | 0.0216 | 0.2691 | 0.2998 | 1.0000 |
| Voltage controller(vq) | 0.0000 | 0.0000 | 0.0000 | 0.0000 | 0.0001 | 0.0001 | 0.0002 | 0.0002 | 0.0043 | 0.0043 | 0.0147 | 0.0147 | 0.0668 | 0.0668 | 0.0129 | 0.0129 | 0.0635 | 0.1129 | 0.0535 | 1.0000 | 0.0504 |
| Current controller(id) | 0.0000 | 0.0000 | 0.0000 | 0.0000 | 0.0000 | 0.0000 | 0.0000 | 0.0000 | 0.0032 | 0.0032 | 0.0122 | 0.0122 | 0.0577 | 0.0577 | 0.0140 | 0.0140 | 0.0116 | 0.3010 | 1.0000 | 0.0000 | 0.1696 |
| Current controller(iq) | 0.0000 | 0.0000 | 0.0000 | 0.0000 | 0.0000 | 0.0000 | 0.0000 | 0.0000 | 0.0032 | 0.0032 | 0.0122 | 0.0122 | 0.0579 | 0.0579 | 0.0120 | 0.0120 | 0.0392 | 1.0000 | 0.2044 | 0.0000 | 0.0085 |
| Q droop control(KQdroop) | 0.0000 | 0.0000 | 0.0000 | 0.0000 | 0.0000 | 0.0000 | 0.0000 | 0.0000 | 0.0003 | 0.0003 | 0.0010 | 0.0010 | 0.0240 | 0.0240 | 0.0150 | 0.0150 | 1.0000 | 0.0679 | 0.0507 | 0.0000 | 0.0824 |
| cita | 0.0000 | 0.0000 | 0.0000 | 0.0000 | 0.0000 | 0.0000 | 0.0000 | 0.0000 | 0.0000 | 0.0000 | 0.0001 | 0.0001 | 0.0075 | 0.0075 | 1.0000 | 1.0000 | 0.0028 | 0.0037 | 0.0021 | 0.0000 | 0.0005 |
| P droop control(KPdroop) | 0.0000 | 0.0000 | 0.0000 | 0.0000 | 0.0000 | 0.0000 | 0.0000 | 0.0000 | 0.0000 | 0.0000 | 0.0001 | 0.0001 | 0.0076 | 0.0076 | 0.9839 | 0.9839 | 0.0156 | 0.0231 | 0.0209 | 0.0000 | 0.0289 |
| IdTH | 0.0001 | 0.0001 | 0.0001 | 0.0001 | 0.0025 | 0.0025 | 0.0025 | 0.0025 | 1.0000 | 1.0000 | 0.6197 | 0.6197 | 0.8838 | 0.8838 | 0.0106 | 0.0106 | 0.0013 | 0.0003 | 0.0004 | 0.0000 | 0.0002 |
| IqTH | 0.0001 | 0.0001 | 0.0001 | 0.0001 | 0.0025 | 0.0025 | 0.0025 | 0.0025 | 0.9999 | 0.9999 | 0.6199 | 0.6199 | 0.8871 | 0.8871 | 0.0045 | 0.0045 | 0.0005 | 0.0000 | 0.0000 | 0.0000 | 0.0000 |
| Vpi2d | 0.4996 | 0.4996 | 0.4996 | 0.4996 | 0.1173 | 0.1173 | 0.1170 | 0.1170 | 0.6190 | 0.6190 | 0.5133 | 0.5133 | 0.0214 | 0.0214 | 0.0000 | 0.0000 | 0.0000 | 0.0000 | 0.0000 | 0.0000 | 0.0000 |
| Vpi2q | 0.4996 | 0.4996 | 0.4996 | 0.4996 | 0.1173 | 0.1173 | 0.1170 | 0.1170 | 0.6190 | 0.6190 | 0.5133 | 0.5133 | 0.0216 | 0.0216 | 0.0000 | 0.0000 | 0.0001 | 0.0000 | 0.0000 | 0.0000 | 0.0000 |
| Ipid | 1.0000 | 1.0000 | 1.0000 | 1.0000 | 0.0015 | 0.0015 | 0.0015 | 0.0015 | 0.0000 | 0.0000 | 0.0000 | 0.0000 | 0.0002 | 0.0002 | 0.0000 | 0.0000 | 0.0000 | 0.0000 | 0.0000 | 0.0000 | 0.0000 |
| Ipiq | 1.0000 | 1.0000 | 1.0000 | 1.0000 | 0.0015 | 0.0015 | 0.0015 | 0.0015 | 0.0000 | 0.0000 | 0.0000 | 0.0000 | 0.0002 | 0.0002 | 0.0000 | 0.0000 | 0.0000 | 0.0000 | 0.0000 | 0.0000 | 0.0000 |
| Vpi1d | 0.5020 | 0.5020 | 0.5020 | 0.5020 | 0.1140 | 0.1140 | 0.1137 | 0.1137 | 0.6153 | 0.6153 | 0.5115 | 0.5115 | 0.0227 | 0.0227 | 0.0001 | 0.0001 | 0.0000 | 0.0000 | 0.0000 | 0.0000 | 0.0000 |
| Vpi1q | 0.5020 | 0.5020 | 0.5020 | 0.5020 | 0.1140 | 0.1140 | 0.1137 | 0.1137 | 0.6153 | 0.6153 | 0.5116 | 0.5116 | 0.0229 | 0.0229 | 0.0000 | 0.0000 | 0.0001 | 0.0000 | 0.0000 | 0.0000 | 0.0000 |
| Itrd | 0.0016 | 0.0016 | 0.0016 | 0.0016 | 1.0000 | 1.0000 | 1.0000 | 1.0000 | 0.0060 | 0.0060 | 0.0138 | 0.0138 | 0.0378 | 0.0378 | 0.0005 | 0.0005 | 0.0001 | 0.0000 | 0.0000 | 0.0000 | 0.0000 |
| Itrq | 0.0016 | 0.0016 | 0.0016 | 0.0016 | 1.0000 | 1.0000 | 1.0000 | 1.0000 | 0.0060 | 0.0060 | 0.0138 | 0.0138 | 0.0379 | 0.0379 | 0.0003 | 0.0003 | 0.0000 | 0.0000 | 0.0000 | 0.0000 | 0.0000 |
| Vvscd | 0.0000 | 0.0000 | 0.0000 | 0.0000 | 0.7964 | 0.7964 | 0.7989 | 0.7989 | 0.4411 | 0.4411 | 0.4572 | 0.4572 | 0.0890 | 0.0890 | 0.0060 | 0.0060 | 0.0003 | 0.0014 | 0.0005 | 0.0000 | 0.0001 |
| Vvscq | 0.0000 | 0.0000 | 0.0000 | 0.0000 | 0.7964 | 0.7964 | 0.7989 | 0.7989 | 0.4411 | 0.4411 | 0.4572 | 0.4572 | 0.0899 | 0.0899 | 0.0001 | 0.0001 | 0.0049 | 0.0017 | 0.0006 | 0.0000 | 0.0000 |
| Idvsc | 0.0000 | 0.0000 | 0.0000 | 0.0000 | 0.1013 | 0.1013 | 0.1104 | 0.1104 | 0.4958 | 0.4958 | 1.0000 | 1.0000 | 0.9960 | 0.9960 | 0.0126 | 0.0126 | 0.0448 | 0.0739 | 0.0837 | 0.1425 | 0.0522 |
| Iqvsc | 0.0000 | 0.0000 | 0.0000 | 0.0000 | 0.1013 | 0.1013 | 0.1104 | 0.1104 | 0.4960 | 0.4960 | 0.9993 | 0.9993 | 1.0000 | 1.0000 | 0.0065 | 0.0065 | 0.0248 | 0.0012 | 0.0049 | 0.0040 | 0.0012 |

Figure 56: **GFOR modes when SCR = 3**

### 7.1.2 Stability analysis of GFOR under different SCRs

It is known that the short circuit ratio (SCR) is usually defined as a measure of the strength of the grid. According to IEEE Standard 1204-1997, when the SCR is less than 2, the grid is very weak. Alternatively, when the SCR is greater than 3, the grid becomes very strong [33].

By varying the control parameters, the effect of different control parameters on the modes can be observed. The effect of grid strength on the modes can be observed by varying the SCRs. In order to compare the performance of grid-forming converters under different SCRs, a state-space model of the whole system was developed on the basis of a small-signal model.

Table 5 shows the real, imaginary, frequency, and damping ratios for the different modes at different SCRs. Where the stability of the modes improves as the color deepens.

Table 5: Real, Imaginary, Frequency and Damping ratio with different SCR

| | SCR=1 | | | | SCR=3 | | | | SCR=5 | | | |
|---|---|---|---|---|---|---|---|---|---|---|---|---|
| Mode | Real | Imaginary | Frequency | $\xi$ | Real | Imaginary | Frequency | $\xi$ | Real | Imaginary | Frequency | $\xi$ |
| 1 | -28979.97 | 88351.39 | 14061.56 | 0.90 | -28978.62 | 88353.23 | 14061.85 | 0.90 | -28977.27 | 88355.07 | 14062.15 | 0.90 |
| 2 | -28979.97 | -88351.39 | 14061.56 | 0.90 | -28978.62 | -88353.23 | 14061.85 | 0.90 | -28977.27 | -88355.07 | 14062.15 | 0.90 |
| 3 | -28979.97 | 87723.07 | 13961.56 | 0.90 | -28978.62 | 87724.91 | 13961.85 | 0.90 | -28977.27 | 87726.75 | 13962.15 | 0.90 |
| 4 | -28979.97 | -87723.07 | 13961.56 | 0.90 | -28978.62 | -87724.91 | 13961.85 | 0.90 | -28977.27 | -87726.75 | 13962.15 | 0.90 |
| 5 | -437.76 | 7931.03 | 1262.26 | 0.33 | -435.91 | 7936.76 | 1263.18 | 0.33 | -434.05 | 7942.56 | 1264.10 | 0.32 |
| 6 | -437.76 | -7931.03 | 1262.26 | 0.33 | -435.91 | -7936.76 | 1263.18 | 0.33 | -434.05 | -7942.56 | 1264.10 | 0.32 |
| 7 | -437.65 | 7310.04 | 1163.43 | 0.35 | -435.82 | 7315.74 | 1164.34 | 0.35 | -433.97 | 7321.50 | 1165.25 | 0.35 |
| 8 | -437.65 | -7310.04 | 1163.43 | 0.35 | -435.82 | -7315.74 | 1164.34 | 0.35 | -433.97 | -7321.50 | 1165.25 | 0.35 |
| 9 | -136.59 | 958.29 | 152.52 | 0.67 | -139.76 | 1181.88 | 188.10 | 0.60 | -143.28 | 1353.03 | 215.34 | 0.55 |
| 10 | -136.59 | -958.29 | 152.52 | 0.67 | -139.76 | -1181.88 | 188.10 | 0.60 | -143.28 | -1353.03 | 215.34 | 0.55 |
| 11 | -89.92 | 549.84 | 87.51 | 0.72 | -107.70 | 695.94 | 110.76 | 0.70 | -119.20 | 830.31 | 132.15 | 0.67 |
| 12 | -89.92 | -549.84 | 87.51 | 0.72 | -107.70 | -695.94 | 110.76 | 0.70 | -119.20 | -830.31 | 132.15 | 0.67 |
| 13 | -52.15 | 227.43 | 36.20 | 0.82 | -34.57 | 149.58 | 23.81 | 0.82 | -23.28 | 112.63 | 17.92 | 0.79 |
| 14 | -52.15 | -227.43 | 36.20 | 0.82 | -34.57 | -149.58 | 23.81 | 0.82 | -23.28 | -112.63 | 17.92 | 0.79 |
| 15 | -53.35 | 0.00 | 0.00 | 1.00 | -59.89 | 0.00 | 0.00 | 1.00 | -65.33 | 0.00 | 0.00 | 1.00 |
| 16 | -46.54 | 0.00 | 0.00 | 1.00 | -36.55 | 0.00 | 0.00 | 1.00 | -24.84 | 13.03 | 2.07 | 1.00 |
| 17 | -3.30 | 0.00 | 0.00 | 1.00 | -13.74 | 0.00 | 0.00 | 1.00 | -24.84 | -13.03 | 2.07 | 1.00 |
| 18 | -8.86 | 0.11 | 0.02 | 1.00 | -8.18 | 0.00 | 0.00 | 1.00 | -8.31 | 0.00 | 0.00 | 1.00 |
| 19 | -8.86 | -0.11 | 0.02 | 1.00 | -9.53 | 0.65 | 0.10 | 1.00 | -10.47 | 0.00 | 0.00 | 1.00 |
| 20 | -10.47 | 0.00 | 0.00 | 1.00 | -9.53 | -0.65 | 0.10 | 1.00 | -9.73 | 0.41 | 0.06 | 1.00 |
| 21 | -10.49 | 0.00 | 0.00 | 1.00 | -10.47 | 0.00 | 0.00 | 1.00 | -9.73 | -0.41 | 0.06 | 1.00 |

The trajectory of the eigenvalues of the GFOR system as the SCR increases from 1 to 5 is plotted in Fig. 57. As the SCR changes from 1 to 5, all the eigenvalues of the GFOR system remain in the left half-plane.

**Mode 1-4:** As can be seen from A as well as B in Fig. 57(b), the real part of modes 1-4 is getting increasingly larger and therefore closer to the origin. These mode points are conjugate, therefore, it is only necessary to zoom in and view Cluster 1 in Fig. 57(a) to see their positions.

**Mode 5-8:** From C as well as D in Fig. 57(d) it can be seen that the real part of modes 5-8 is getting larger and therefore closer to the origin. These mode points are conjugate, so it is only necessary to zoom in and observe at cluster 4 in Fig. 57(c).

**Mode 9-12:** As can be seen from E as well as F in Fig. 57(e), the real part of modes 9-12 is getting smaller and smaller and therefore more and more away from the origin. In addition, their oscillation frequencies and damping ratios are gradually reduced.

**Mode 13,14,16:** As shown in G of Fig. 57(e), with the addition of SCRs, modes 13, 14, and 16 are very close to the right half-plane and there is a risk of the system losing stability. The damping ratios of modes 13 and 14 are getting smaller and smaller. Mode 16 shows its oscillatory behavior at very low frequencies.

**Mode 15:** As can be seen from H in Fig. 57(e), the real part of mode 15 is getting smaller and smaller, moving further and further away from the origin. Furthermore, it shows no oscillatory behavior.

**Mode 17-21:** Modes 17-21 are not affected by the increase in SCR and their positions remain almost unchanged. However, it can be seen that the position of mode 18 in Fig. 57(f), is very close to the origin, and the position of this pole may be critical.

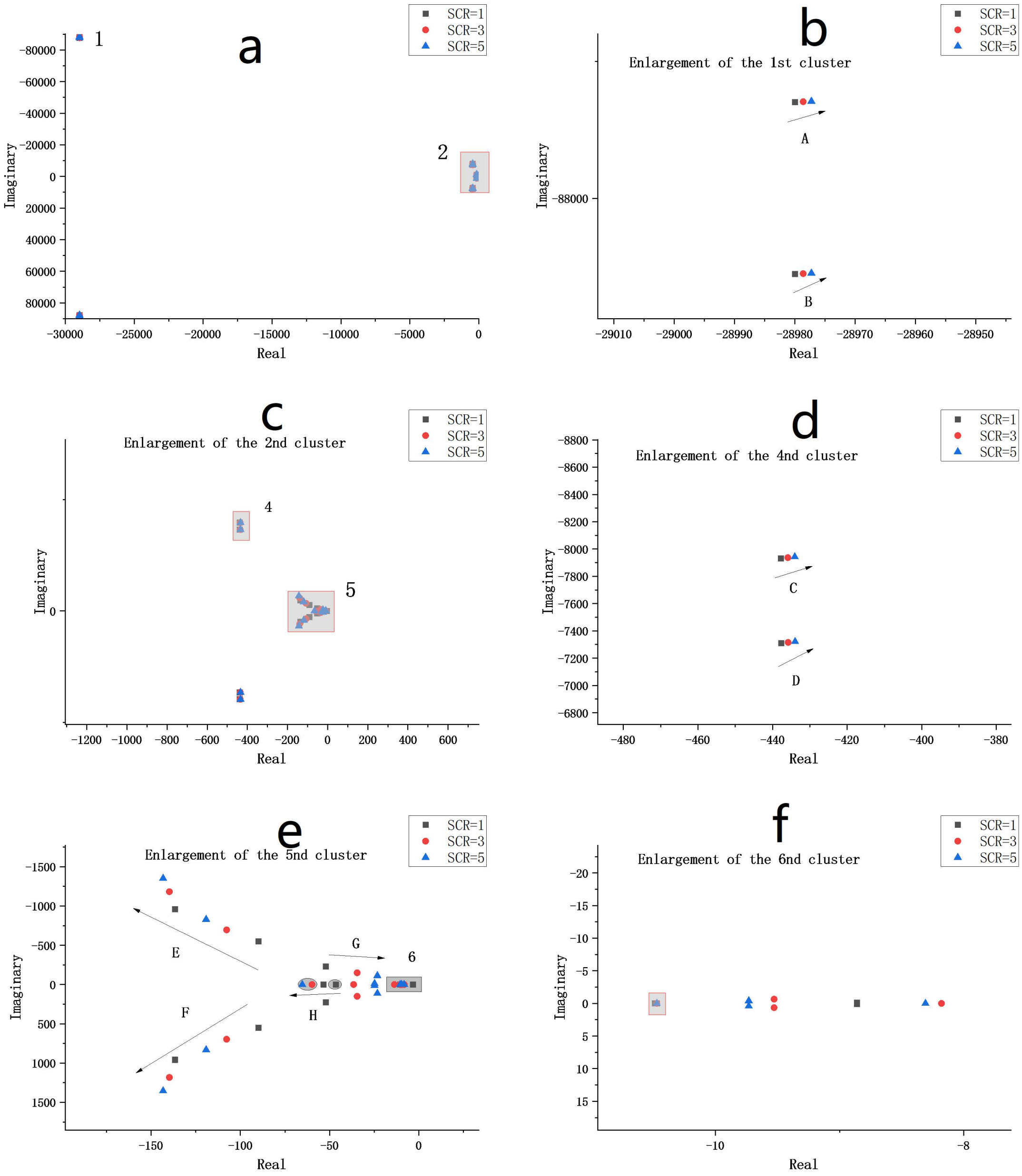

Figure 57: **The modes with different SCR**

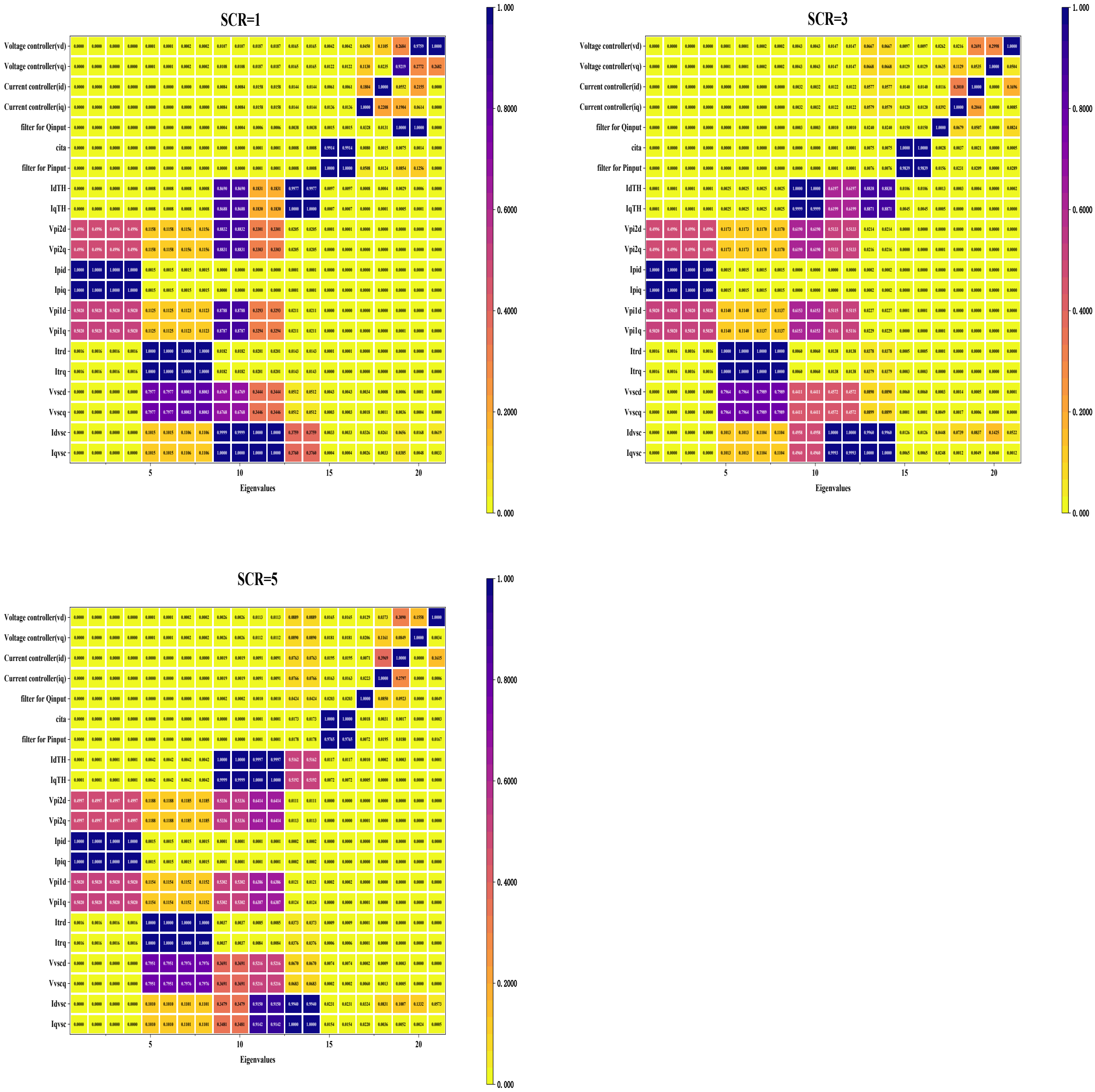

Figure 58: **Participation factor of GFOR modes at different SCR**

As can be seen from the Fig. 58 at different SCRs, as the SCR increases, Modes 9 and 10 have higher PF values with Group 5(Thevenin grid $I_{dTH}$,$I_{qTH}$). While modes 9 and 10 have gradually lower PF values with Group 8(Convertor side $I_{vscq}$,$I_{vscd}$,$V_{vscq}$).

However, modes 13-14 have lower PF values for Group 5 and higher PF values for Group 8 as the SCR increases.

It can also be seen that as the SCR increases, the interaction within Group 1(voltage control $v_d$,$v_q$) decreases, and the interaction within Group 2:(current control $i_d$,$i_q$) increases.

### 7.1.3 Stability analysis of GFOR under different $k_{pcc}$

The effect of different control parameters on the stability of the system was observed by varying the control parameters. By varying the control parameter $k_{pcc}$ of the current loop, the effect of it on the stability of the system was observed.

Table 6 shows the real, imaginary, frequency, and damping ratios for different modes with different $k_{pcc}$. In this case, the distance of the mode from the origin increases as the color deepens.

Table 6: Real, Imaginary, Frequency and Damping ratio with different $k_{pcc}$

| | $k_{pcc}$=0.0827 | | | | $k_{pcc}$=0.1 | | | | $k_{pcc}$=0.12 | | | |
|---|---|---|---|---|---|---|---|---|---|---|---|---|
| | Real | Imaginary | Frequency | $\xi$ | Real | Imaginary | Frequency | $\xi$ | Real | Imaginary | Frequency | $\xi$ |
| 1 | -28978.55 | 88353.32 | 14061.87 | 0.90 | -28978.55 | 88353.32 | 14061.87 | 0.90 | -28978.55 | 88353.32 | 14061.87 | 0.90 |
| 2 | -28978.55 | -88353.32 | 14061.87 | 0.90 | -28978.55 | 88353.32 | 14061.87 | 0.90 | -28978.55 | 88353.32 | 14061.87 | 0.90 |
| 3 | -28978.55 | 87725.00 | 13961.87 | 0.90 | -28978.55 | 87725.01 | 13961.87 | 0.90 | -28978.55 | 87725.01 | 13961.87 | 0.90 |
| 4 | -28978.55 | 87725.00 | 13961.87 | 0.90 | -28978.55 | 87725.01 | 13961.87 | 0.90 | -28978.55 | 87725.01 | 13961.87 | 0.90 |
| 5 | -436.04 | 7937.09 | 1263.23 | 0.33 | -518.17 | 7945.36 | 1264.54 | 0.38 | -613.55 | 7952.63 | 1265.70 | 0.44 |
| 6 | -436.04 | 7937.09 | 1263.23 | 0.33 | -518.17 | 7945.36 | 1264.54 | 0.38 | -613.55 | 7952.63 | 1265.70 | 0.44 |
| 7 | -435.95 | 7316.07 | 1164.39 | 0.35 | -518.07 | 7325.86 | 1165.95 | 0.41 | -613.45 | 7334.91 | 1167.39 | 0.47 |
| 8 | -435.95 | 7316.07 | 1164.39 | 0.35 | -518.07 | 7325.86 | 1165.95 | 0.41 | -613.45 | 7334.91 | 1167.39 | 0.47 |
| 9 | -153.63 | 1192.02 | 189.72 | 0.63 | -175.86 | 1226.23 | 195.16 | 0.67 | -201.64 | 1264.11 | 201.19 | 0.71 |
| 10 | -153.63 | 1192.02 | 189.72 | 0.63 | -175.86 | 1226.23 | 195.16 | 0.67 | -201.64 | 1264.11 | 201.19 | 0.71 |
| 11 | -117.83 | 702.62 | 111.83 | 0.73 | -135.71 | 749.10 | 119.22 | 0.75 | -156.37 | 798.45 | 127.08 | 0.78 |
| 12 | -117.83 | 702.62 | 111.83 | 0.73 | -135.71 | 749.10 | 119.22 | 0.75 | -156.37 | 798.45 | 127.08 | 0.78 |
| 13 | -56.61 | 146.03 | 23.24 | 0.93 | -63.39 | 159.73 | 25.42 | 0.93 | -69.58 | 172.93 | 27.52 | 0.93 |
| 14 | -56.61 | 146.03 | 23.24 | 0.93 | -63.39 | 159.73 | 25.42 | 0.93 | -69.58 | 172.93 | 27.52 | 0.93 |
| 15 | -4.85 | 8.14 | 1.30 | 0.97 | -4.83 | 8.13 | 1.29 | 0.97 | -4.82 | 8.12 | 1.29 | 0.97 |
| 16 | -4.85 | 8.14 | 1.30 | 0.97 | -4.83 | 8.13 | 1.29 | 0.97 | -4.82 | 8.12 | 1.29 | 0.97 |
| 17 | -12.16 | 0.00 | 0.00 | 1.00 | -12.09 | 0.00 | 0.00 | 1.00 | -12.07 | 0.00 | 0.00 | 1.00 |
| 18 | -8.62 | 0.00 | 0.00 | 1.00 | -8.17 | 0.00 | 0.00 | 1.00 | -7.03 | 0.00 | 0.00 | 1.00 |
| 19 | -9.10 | 0.00 | 0.00 | 1.00 | -9.13 | 0.00 | 0.00 | 1.00 | -7.46 | 0.00 | 0.00 | 1.00 |
| 20 | -10.47 | 0.00 | 0.00 | 1.00 | -8.75 | 0.61 | 0.10 | 1.00 | -8.89 | 0.00 | 0.00 | 1.00 |
| 21 | -10.18 | 0.00 | 0.00 | 1.00 | -8.75 | 0.61 | 0.10 | 1.00 | -8.55 | 0.00 | 0.00 | 1.00 |

The effect of varying $k_{pcc}$ on system stability can be seen more visually in Fig. 59. And it can be observed that the modes behave as follows as $k_{pcc}$ increases:

**Mode 1-4:** As can be seen from A in Fig. 59(b), the change in $k_{pcc}$ has little effect on the stability of modes 1-4.

**Mode 5-8:** The movement of modes 5-8 can be seen at B in Fig. 59(c). The real part of these two modes is getting increasingly smaller and therefore further away from the origin.

**Mode 9-12:** The motion of modes 9-12 can be seen at C in Fig. 59(d). The real part of these two modes is getting increasingly smaller and therefore further away from the origin. At the same time their damping ratios and oscillation frequencies are getting larger, indicating that these modes are becoming less overshoot in the face of the perturbation and faster in their response.

**Mode 13-14:** The motion of modes 13-14 can be seen at D in Fig. 59(d). The real part of these two modes is getting increasingly smaller and therefore further away from the origin.

**Mode 15-16:** As can be seen from F in Fig. 59(e), the change in $k_{pcc}$ has little effect on modes 15-16.

**Mode 17:** As can be seen from E in Fig. 59(e), the change in $k_{pcc}$ has little effect on modes 17.

**Mode 18-19:** The distribution of modes 18-21 can be seen in Fig. 59(f). There is no clear pattern and little variation in the position of mode 19 as $k_{pcc}$ increases. However, it can be noticed that the damping ratio of modes 18-19 is 1 and the oscillation frequency is 0. They no longer have oscillatory behavior. The movement of mode 18 can be seen. The real part of this mode is getting small and therefore away from the origin.

**Mode 20-21:** The distribution of modes 20-21 can be seen in Fig. 59(f). There is no clear pattern and little variation in the position of modes 20-21 as $k_{pcc}$ increases. However, it can be noted that the damping ratio of modes 20-21 is always 1, but at $k_{pcc} = 1$, the oscillation frequency will not be 0, with low-frequency oscillation characteristics. At the same time, they are complex conjugates.

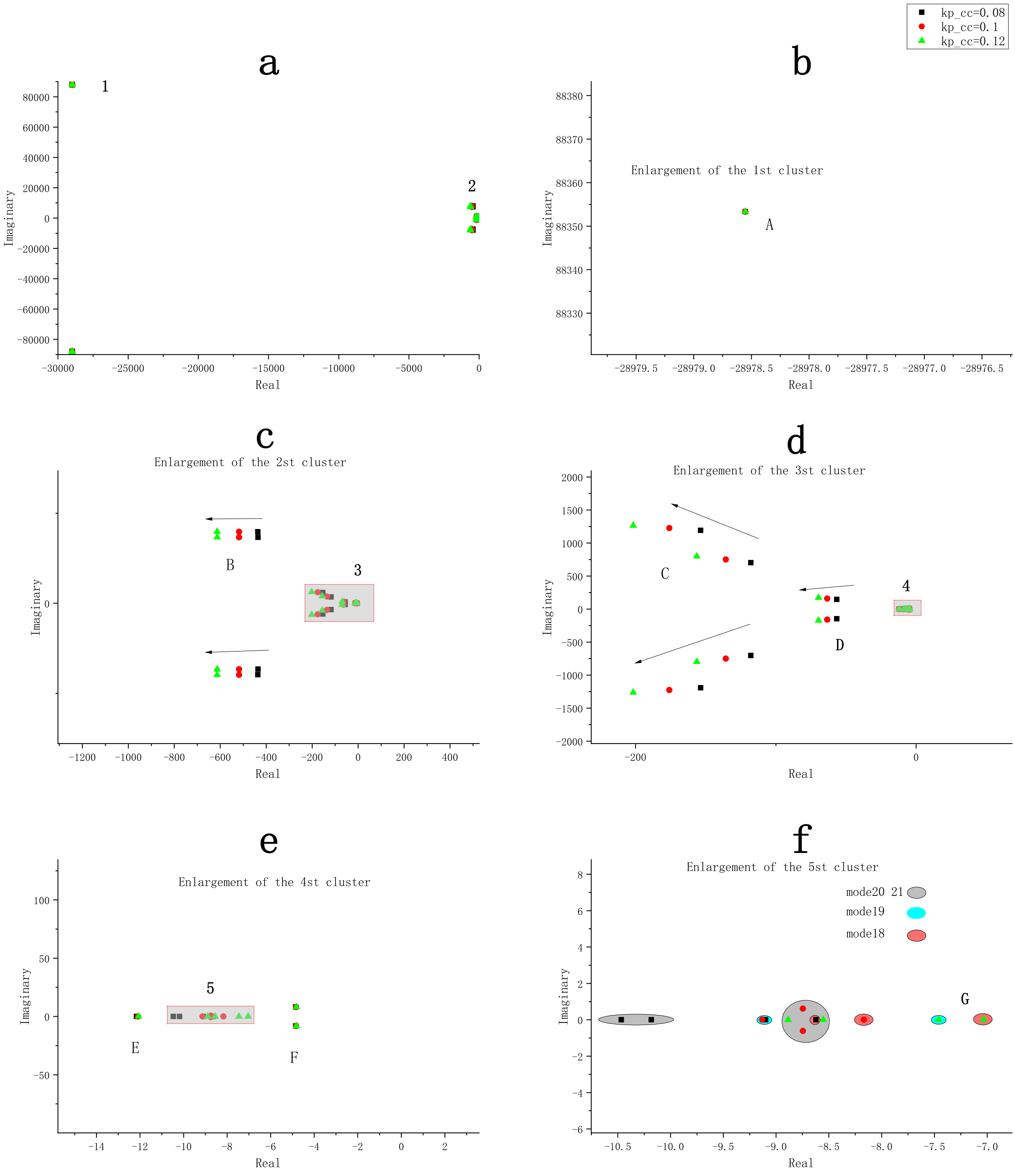

Figure 59: **GFOR modes with different $k_{pcc}$**

From Fig. 60 it can be noticed that as $k_{pcc}$ increases, the interaction within Group 1(voltage control $v_d$,$v_q$) and Group 2:(current control $i_d$,$i_q$) can be seen to first increase and then decrease.

As $k_{pcc}$ increases, the interaction between $I_{dvsc}$ and $I_{qvsc}$ weakens.

For modes 20 and 21, Group 1, group 2 and $i_vsc$ are interacting at $k_{pcc}$ = 0.1, but they no longer have interaction when $k_{pcc}$ is not equal to 0.1. This may be related to the fact that at $k_{pcc}$=0.1, modes 20 and 21 have very low oscillation frequencies, while Group 1, Group 2, and Group 8 contribute to this phenomenon.

Table 6 shows that as $k_{pcc}$ increases, the modes that change position significantly with increasing $k_{pcc}$ are also all further away from the origin. It can therefore be said that the relative stability of the system is increased by increasing the $k_{pcc}$.

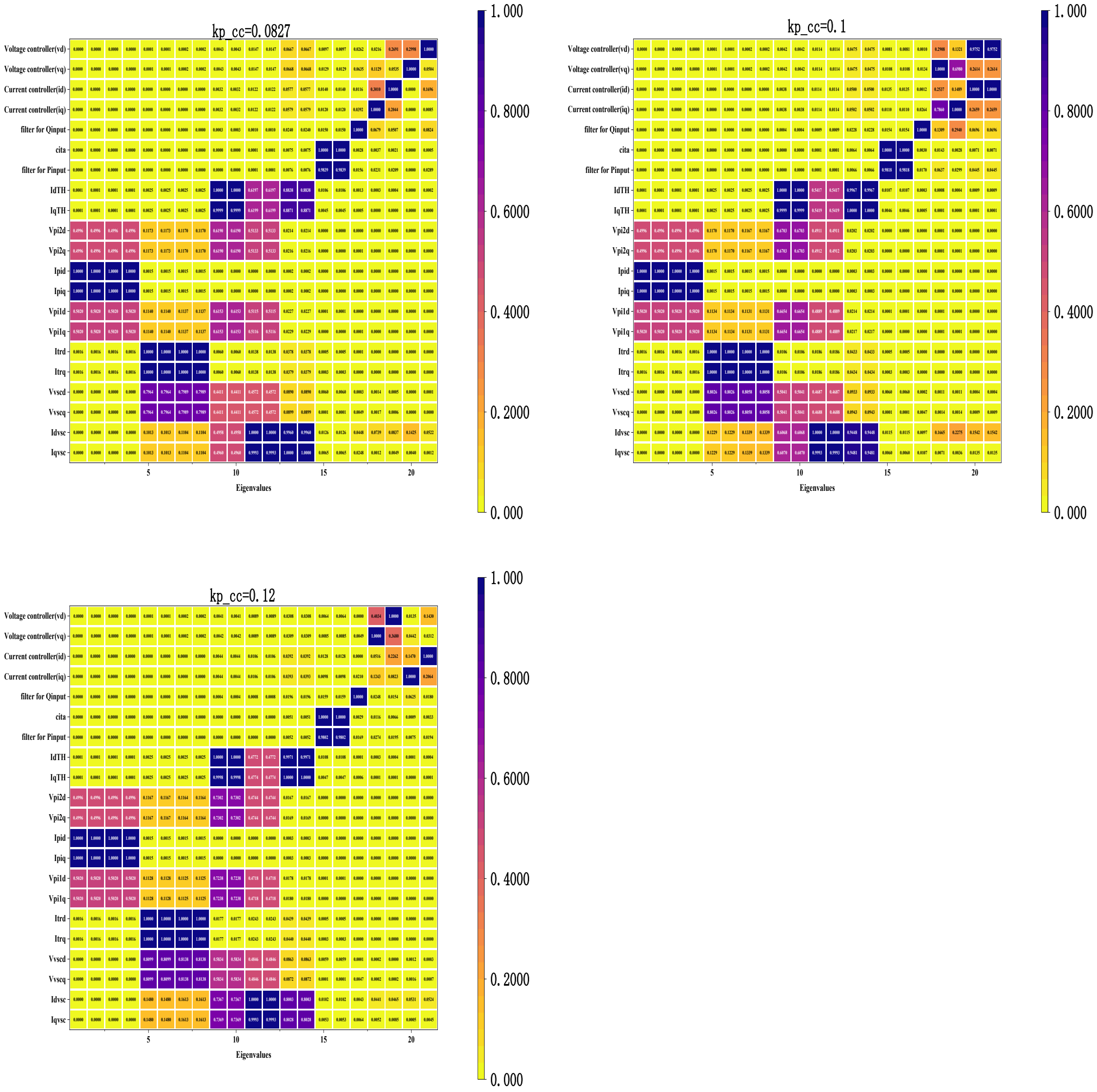

Figure 60: **Participation factor of GFOR modes with different $k_{pcc}$**

### 7.1.4 Stability analysis of GFOR under different XR

Table 7 shows the real, imaginary, frequency, and damping ratios for the different modes at different XR.

As can be seen from table 7, the change in XR has little effect on the position of the modes except for 9-14. The real part of modes 9-14 gets larger as XR increases and its position gets closer to the origin. It can be seen that the relative stability of the system is decreased by increasing the XR.

Table 7: Real, Imaginary, Frequency and Damping ratio with different XR

| | XR=1 | | | | XR=5 | | | | XR=10 | | | |
|---|---|---|---|---|---|---|---|---|---|---|---|---|
| | Real | Imaginary | Frequency | kce | Real | Imaginary | Frequency | kce | Real | Imaginary | Frequency | kce |
| 1 | -28977.84 | 88354.30675 | 14062.02 | 0.90 | -28978.61978 | 88353.22885 | 14061.85 | 0.90 | -28978.64857 | 88353.18782 | 14061.85 | 0.90 |
| 2 | -28977.84 | -88354.30675 | 14062.02 | 0.90 | -28978.61978 | -88353.22885 | 14061.85 | 0.90 | -28978.64857 | -88353.18782 | 14061.85 | 0.90 |
| 3 | -28977.84 | 87725.98821 | 13962.02 | 0.90 | -28978.61978 | 87724.91032 | 13961.85 | 0.90 | -28978.64857 | 87724.86929 | 13961.85 | 0.90 |
| 4 | -28977.84 | -87725.98821 | 13962.02 | 0.90 | -28978.61978 | -87724.91032 | 13961.85 | 0.90 | -28978.64857 | -87724.86929 | 13961.85 | 0.90 |
| 5 | -435.2277 | 7940.252424 | 1263.73 | 0.33 | -435.910254 | 7936.76599 | 1263.18 | 0.33 | -435.9162636 | 7936.627326 | 1263.15 | 0.33 |
| 6 | -435.2277 | -7940.252424 | 1263.73 | 0.33 | -435.910254 | -7936.76599 | 1263.18 | 0.33 | -435.9162636 | -7936.627326 | 1263.15 | 0.33 |
| 7 | -435.1414 | 7319.208578 | 1164.89 | 0.35 | -435.8197319 | 7315.742186 | 1164.34 | 0.35 | -435.8257116 | 7315.604334 | 1164.31 | 0.35 |
| 8 | -435.1414 | -7319.208578 | 1164.89 | 0.35 | -435.8197319 | -7315.742186 | 1164.34 | 0.35 | -435.8257116 | -7315.604334 | 1164.31 | 0.35 |
| 9 | -231.7875 | 1280.290102 | 203.76 | 0.75 | -139.5438569 | 1181.768684 | 188.08 | 0.60 | -129.2578656 | 1176.707726 | 187.28 | 0.57 |
| 10 | -231.7875 | -1280.290102 | 203.76 | 0.75 | -139.5438569 | -1181.768684 | 188.08 | 0.60 | -129.2578656 | -1176.707726 | 187.28 | 0.57 |
| 11 | -179.1911 | 763.6156454 | 121.53 | 0.83 | -108.1411378 | 696.1808592 | 110.80 | 0.70 | -101.3378619 | 693.3323767 | 110.35 | 0.68 |
| 12 | -179.1911 | -763.6156454 | 121.53 | 0.83 | -108.1411378 | -696.1808592 | 110.80 | 0.70 | -101.3378619 | -693.3323767 | 110.35 | 0.68 |
| 13 | -129.336 | 118.5026548 | 18.86 | 0.99 | -38.11647214 | 149.9381717 | 23.86 | 0.85 | -23.68284216 | 152.229265 | 24.23 | 0.70 |
| 14 | -129.336 | -118.5026548 | 18.86 | 0.99 | -38.11647214 | -149.9381717 | 23.86 | 0.85 | -23.68284216 | -152.229265 | 24.23 | 0.70 |
| 15 | -4.436723 | 7.439994595 | 1.18 | 0.97 | -4.932760076 | 8.180606961 | 1.30 | 0.97 | -4.983929048 | 8.169100301 | 1.30 | 0.97 |
| 16 | -4.436723 | -7.439994595 | 1.18 | 0.97 | -4.932760076 | -8.180606961 | 1.30 | 0.97 | -4.983929048 | -8.169100301 | 1.30 | 0.97 |
| 17 | -12.69205 | 0 | 0.00 | 1.00 | -12.06733177 | 0 | 0.00 | 1.00 | -12.01264138 | 0 | 0.00 | 1.00 |
| 18 | -8.535735 | 0 | 0.00 | 1.00 | -8.639583875 | 0 | 0.00 | 1.00 | -8.651437613 | 0 | 0.00 | 1.00 |
| 19 | -9.06832 | 0 | 0.00 | 1.00 | -9.108095837 | 0 | 0.00 | 1.00 | -9.117209327 | 0 | 0.00 | 1.00 |
| 20 | -10.47198 | 0 | 0.00 | 1.00 | -10.47197551 | 0 | 0.00 | 1.00 | -10.47197551 | 0 | 0.00 | 1.00 |
| 21 | -10.16202 | 0 | 0.00 | 1.00 | -10.19427834 | 0 | 0.00 | 1.00 | -10.20046185 | 0 | 0.00 | 1.00 |

### 7.1.5 Stability analysis of the GFOR under different closed-loop time constants of the current loop

The position of modes 5-14 varies significantly with the increase of $\tau$. They are all moving closer to the origin.

The damping ratio of mode 5 and mode 6 decreases a lot with increasing $\tau$, and when $\tau = 7$, the damping ratio of mode 5 and mode 6 are very low, and mode 5 and mode 6 are critical poles.

Table 8: Real, Imaginary, Frequency and Damping ratio with different $\tau$ of current loop

| | $\tau$=1 | | | | $\tau$=3 | | | | $\tau$=7 | | | |
|---|---|---|---|---|---|---|---|---|---|---|---|---|
| | Real | Imaginary | Frequency | $\xi$ | Real | Imaginary | Frequency | $\xi$ | Real | Imaginary | Frequency | $\xi$ |
| 1 | -28978.55254 | 88353.32295 | 14061.87 | 0.90 | -28978.55263 | 88353.32017 | 14061.87 | 0.90 | -28978.6 | 88353.32 | 14061.87 | 0.90 |
| 2 | -28978.55254 | -88353.32295 | 14061.87 | 0.90 | -28978.55263 | -88353.32017 | 14061.87 | 0.90 | -28978.6 | -88353.3 | 14061.87 | 0.90 |
| 3 | -28978.55254 | 87725.00442 | 13961.87 | 0.90 | -28978.55263 | 87725.00164 | 13961.87 | 0.90 | -28978.6 | 87725 | 13961.87 | 0.90 |
| 4 | -28978.55254 | -87725.00442 | 13961.87 | 0.90 | -28978.55263 | -87725.00164 | 13961.87 | 0.90 | -28978.6 | -87725 | 13961.87 | 0.90 |
| 5 | -435.8650733 | 7937.074547 | 1263.22 | 0.33 | -176.9683089 | 7898.136444 | 1257.03 | 0.14 | -103.806 | 7883.554 | 1254.71 | 0.08 |
| 6 | -435.8650733 | -7937.074547 | 1263.22 | 0.33 | -176.9683089 | -7898.136444 | 1257.03 | 0.14 | -103.806 | -7883.55 | 1254.71 | 0.08 |
| 7 | -435.7748295 | 7316.048957 | 1164.39 | 0.35 | -176.9251755 | 7272.251862 | 1157.41 | 0.15 | -103.786 | 7256.28 | 1154.87 | 0.09 |
| 8 | -435.7748295 | -7316.048957 | 1164.39 | 0.35 | -176.9251755 | -7272.251862 | 1157.41 | 0.15 | -103.786 | -7256.28 | 1154.87 | 0.09 |
| 9 | -153.5837016 | 1191.947035 | 189.70 | 0.63 | -86.0783636 | 1071.629465 | 170.56 | 0.45 | -68.1581 | 1033.655 | 164.51 | 0.38 |
| 10 | -153.5837016 | -1191.947035 | 189.70 | 0.63 | -86.0783636 | -1071.629465 | 170.56 | 0.45 | -68.1581 | -1033.65 | 164.51 | 0.38 |
| 11 | -117.795008 | 702.5124804 | 111.81 | 0.73 | -67.37482213 | 516.0347017 | 82.13 | 0.63 | -57.4315 | 443.1088 | 70.52 | 0.63 |
| 12 | -117.795008 | -702.5124804 | 111.81 | 0.73 | -67.37482213 | -516.0347017 | 82.13 | 0.63 | -57.4315 | -443.109 | 70.52 | 0.63 |
| 13 | -56.58941546 | 146.0020571 | 23.24 | 0.93 | -25.61343322 | 75.26021715 | 11.98 | 0.91 | -9.47142 | 39.35897 | 6.26 | 0.83 |
| 14 | -56.58941546 | -146.0020571 | 23.24 | 0.93 | -25.61343322 | -75.26021715 | 11.98 | 0.91 | -9.47142 | -39.359 | 6.26 | 0.83 |
| 15 | -4.851507275 | 8.139027942 | 1.30 | 0.97 | -4.88434932 | 8.361210021 | 1.33 | 0.96 | -4.98635 | 8.743116 | 1.39 | 0.96 |
| 16 | -4.851507275 | -8.139027942 | 1.30 | 0.97 | -4.88434932 | -8.361210021 | 1.33 | 0.96 | -4.98635 | -8.74312 | 1.39 | 0.96 |
| 17 | -12.156982 | 0 | 0.00 | 1.00 | -12.07912217 | 0 | 0.00 | 1.00 | -7.73033 | 0 | 0.00 | 1.00 |
| 18 | -8.622495931 | 0 | 0.00 | 1.00 | -8.304384648 | 0 | 0.00 | 1.00 | -10.4357 | 1.609347 | 0.26 | 1.00 |
| 19 | -9.09735273 | 0 | 0.00 | 1.00 | -10.47197551 | 0 | 0.00 | 1.00 | -10.4357 | -1.60935 | 0.26 | 1.00 |
| 20 | -10.47197551 | 0 | 0.00 | 1.00 | -9.788189027 | 0.597226362 | 0.10 | 1.00 | -10.8164 | 0 | 0.00 | 1.00 |
| 21 | -10.18656736 | 0 | 0.00 | 1.00 | -9.788189027 | -0.597226362 | 0.10 | 1.00 | -10.472 | 0 | 0.00 | 1.00 |

## 7.2 Stability Analysis of grid following system

The GFOL model constructed from the data in Table 2 has been validated.

Table 9 indicates the poles, frequencies, and damping ratios for each mode of the GFOL, for a total of 18 modes.

Table 9: Real, Imaginary, Frequency and Damping ratio with different $\tau_p$ and $\tau_Q$

| | $\tau_p, \tau_q = 0.1$ | | | | $\tau_p, \tau_q = 0.3$ | | | | $\tau_p, \tau_q = 0.5$ | | | |
|---|---|---|---|---|---|---|---|---|---|---|---|---|
| | Real | Imaginary | Frequency | $\xi$ | Real | Imaginary | Frequency | $\xi$ | Real | Imaginary | Frequency | $\xi$ |
| 1 | -29023.47508 | 88293.04 | 14052.27 | 0.90 | -29023.47511 | 88293.03519 | 14052.27 | 0.90 | -29023.5 | 88293.03513 | 14052.27 | 0.90 |
| 2 | -29023.47508 | -88293 | 14052.27 | 0.90 | -29023.47511 | -88293.0352 | 14052.27 | 0.90 | -29023.5 | -88293.03513 | 14052.27 | 0.90 |
| 3 | -29023.47653 | 87664.72 | 13952.27 | 0.90 | -29023.47648 | 87664.71567 | 13952.27 | 0.90 | -29023.5 | 87664.71565 | 13952.27 | 0.90 |
| 4 | -29023.47653 | -87664.7 | 13952.27 | 0.90 | -29023.47648 | -87664.7157 | 13952.27 | 0.90 | -29023.5 | -87664.71565 | 13952.27 | 0.90 |
| 5 | -59.86975419 | 1103.97 | 175.70 | 0.32 | -59.85199222 | 1103.722659 | 175.66 | 0.32 | -59.6296 | 1103.768879 | 175.67 | 0.32 |
| 6 | -59.86975419 | -1103.97 | 175.70 | 0.32 | -59.85199222 | -1103.72266 | 175.66 | 0.32 | -59.6296 | -1103.768879 | 175.67 | 0.32 |
| 7 | -49.48770461 | 453.3505 | 72.15 | 0.57 | -49.26700562 | 455.3617424 | 72.47 | 0.56 | -48.9565 | 456.5515063 | 72.66 | 0.56 |
| 8 | -49.48770461 | -453.351 | 72.15 | 0.57 | -49.26700562 | -455.361742 | 72.47 | 0.56 | -48.9565 | -456.5515063 | 72.66 | 0.56 |
| 9 | -985.0734544 | 0 | 0.00 | 1.00 | -985.5592683 | 0 | 0.00 | 1.00 | -986.636 | 0 | 0.00 | 1.00 |
| 10 | -1000 | 0 | 0.00 | 1.00 | -1000 | 0 | 0.00 | 1.00 | -1000 | 0 | 0.00 | 1.00 |
| 11 | -47.91355142 | 42.8083 | 6.81 | 0.99 | -48.42171475 | 41.53379003 | 6.61 | 0.99 | -48.5604 | 41.18613188 | 6.55 | 0.99 |
| 12 | -47.91355142 | -42.8083 | 6.81 | 0.99 | -48.42171475 | -41.53379 | 6.61 | 0.99 | -48.5604 | -41.18613188 | 6.55 | 0.99 |
| 13 | -14.13684883 | 31.98986 | 5.09 | 0.94 | -11.37200807 | 16.30716047 | 2.60 | 0.97 | -10.8176 | 10.85932282 | 1.73 | 0.99 |
| 14 | -14.13684883 | -31.9899 | 5.09 | 0.94 | -11.37200807 | -16.3071605 | 2.60 | 0.97 | -10.8176 | -10.85932282 | 1.73 | 0.99 |
| 15 | -24.18520528 | 0 | 0.00 | 1.00 | -21.11899442 | 0 | 0.00 | 1.00 | -20.6402 | 0 | 0.00 | 1.00 |
| 16 | -6.944428395 | 0 | 0.00 | 1.00 | -2.745773693 | 0 | 0.00 | 1.00 | -1.69536 | 0 | 0.00 | 1.00 |
| 17 | -10.4354974 | 0 | 0.00 | 1.00 | -10.44724474 | 0 | 0.00 | 1.00 | -10.4458 | 0 | 0.00 | 1.00 |
| 18 | -10.47197551 | 0 | 0.00 | 1.00 | -10.47197551 | 0 | 0.00 | 1.00 | -10.472 | 0 | 0.00 | 1.00 |

As can be seen from Table 9, for modes 5-6, changes in $\tau$ have little effect on their position. Changes in $\tau$ have a greater effect on changes in the position of Mode 16, and Mode 16 has a damping ratio of 1 and does not have oscillatory characteristics.

### 7.2.1 Table of Participation Factors of GFOL

PF is represented as a matrix, with the darker the color, the higher the involvement. In Fig. 61, it can be seen that the state variables of the PI line section: $Vpi1q$, $Vpi1d$, $Vpi2q$, $Vpi2q$, $Ipiq$, and $Ipid$ interact strongly with each other. The eigenvalues that are strongly influenced by these state variables are also all conjugate poles.

The interaction between cita and $Ki_{PLL}$ is also strong as they have high participation factors for the same eigenvalues and create a pair of complex conjugates. This is due to the fact that these two states are highly correlated from a mathematical calculation point of view and the PLL module provides the corresponding electrical angles for the system. The same is true for the Q control module and the input voltage($V_{peak}$), which provides the reference reactive power for the Q control module.

Based on the results in the Fig. 61, the state variables can be grouped into the following clusters:

- Group 1: Thevenin grid $I_{dTH}$,$I_{qTH}$
- Group 2: PI line $V_{pi1q}$ ,$V_{pi1d}$ ,$V_{pi2q}$ ,$V_{pi2q}$ ,$I_{piq}$,$I_{pid}$
- Group 3: Convertor side $I_{vscq}$ ,$I_{vscd}$
- Group 4: P control($KP_{droop}$)and input frequency($\omega$)
- Group 5: Current control $i_q$ and $i_d$

- Group 6: Q control$(KQ_{droop})$ and input voltage$(V_{peak})$
- Group 7: $Ki_{pll}$ and cita

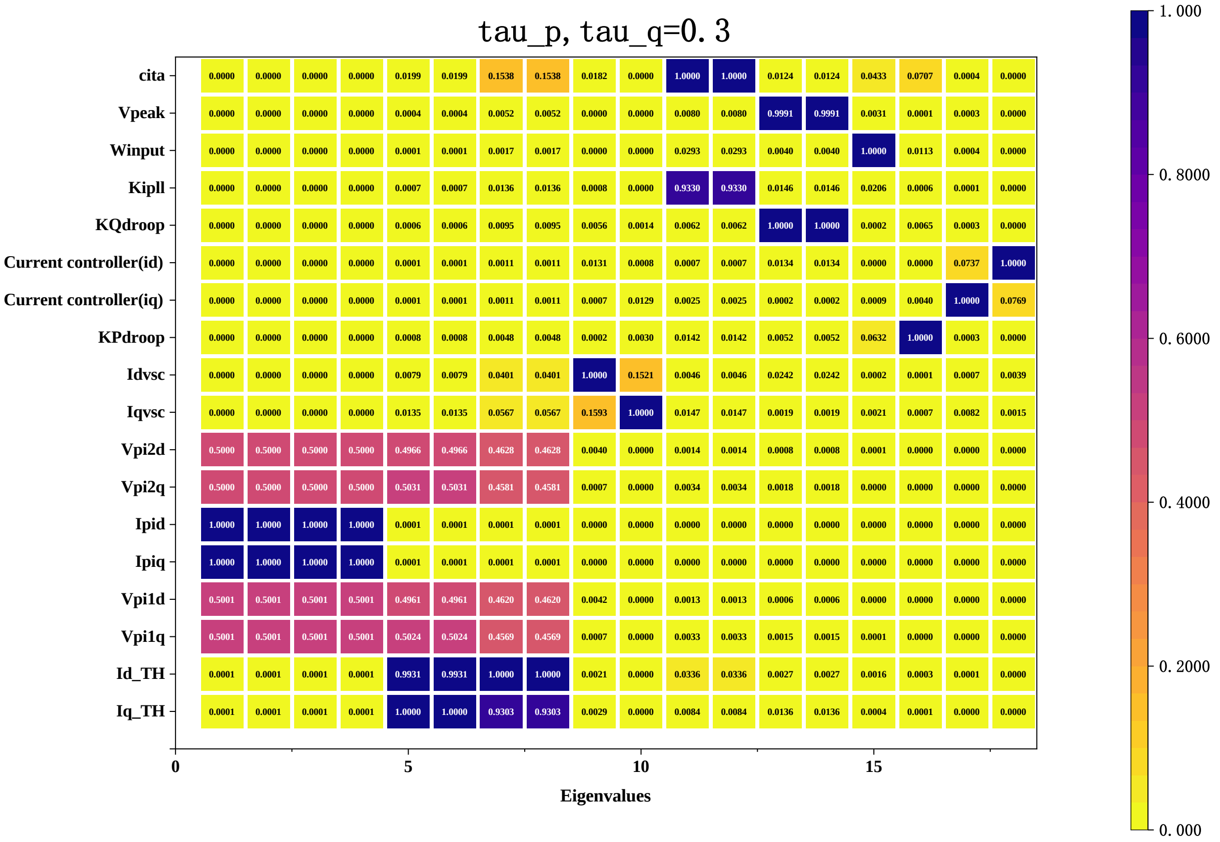

| | | | | | | | | | | | | | | | | | | |
|---|---|---|---|---|---|---|---|---|---|---|---|---|---|---|---|---|---|---|
| cita | 0.0000 | 0.0000 | 0.0000 | 0.0000 | 0.0199 | 0.0199 | 0.1538 | 0.1538 | 0.0182 | 0.0000 | 1.0000 | 1.0000 | 0.0124 | 0.0124 | 0.0433 | 0.0707 | 0.0004 | 0.0000 |
| Vpeak | 0.0000 | 0.0000 | 0.0000 | 0.0000 | 0.0004 | 0.0004 | 0.0052 | 0.0052 | 0.0000 | 0.0000 | 0.0080 | 0.0080 | 0.9991 | 0.9991 | 0.0031 | 0.0001 | 0.0003 | 0.0000 |
| Winput | 0.0000 | 0.0000 | 0.0000 | 0.0000 | 0.0001 | 0.0001 | 0.0017 | 0.0017 | 0.0000 | 0.0000 | 0.0293 | 0.0293 | 0.0040 | 0.0040 | 1.0000 | 0.0113 | 0.0004 | 0.0000 |
| Kipll | 0.0000 | 0.0000 | 0.0000 | 0.0000 | 0.0007 | 0.0007 | 0.0136 | 0.0136 | 0.0008 | 0.0000 | 0.9330 | 0.9330 | 0.0146 | 0.0146 | 0.0206 | 0.0006 | 0.0001 | 0.0000 |
| KQdroop | 0.0000 | 0.0000 | 0.0000 | 0.0000 | 0.0006 | 0.0006 | 0.0095 | 0.0095 | 0.0056 | 0.0014 | 0.0062 | 0.0062 | 1.0000 | 1.0000 | 0.0002 | 0.0065 | 0.0003 | 0.0000 |
| Current controller(id) | 0.0000 | 0.0000 | 0.0000 | 0.0000 | 0.0001 | 0.0001 | 0.0011 | 0.0011 | 0.0131 | 0.0008 | 0.0007 | 0.0007 | 0.0134 | 0.0134 | 0.0000 | 0.0000 | 0.0737 | 1.0000 |
| Current controller(iq) | 0.0000 | 0.0000 | 0.0000 | 0.0000 | 0.0001 | 0.0001 | 0.0011 | 0.0011 | 0.0007 | 0.0129 | 0.0025 | 0.0025 | 0.0002 | 0.0002 | 0.0009 | 0.0040 | 1.0000 | 0.0769 |
| KPdroop | 0.0000 | 0.0000 | 0.0000 | 0.0000 | 0.0008 | 0.0008 | 0.0048 | 0.0048 | 0.0002 | 0.0030 | 0.0142 | 0.0142 | 0.0052 | 0.0052 | 0.0632 | 1.0000 | 0.0003 | 0.0000 |
| Idvsc | 0.0000 | 0.0000 | 0.0000 | 0.0000 | 0.0079 | 0.0079 | 0.0401 | 0.0401 | 1.0000 | 0.1521 | 0.0046 | 0.0046 | 0.0242 | 0.0242 | 0.0002 | 0.0001 | 0.0007 | 0.0039 |
| Iqvsc | 0.0000 | 0.0000 | 0.0000 | 0.0000 | 0.0135 | 0.0135 | 0.0567 | 0.0567 | 0.1593 | 1.0000 | 0.0147 | 0.0147 | 0.0019 | 0.0019 | 0.0021 | 0.0007 | 0.0082 | 0.0015 |
| Vpi2d | 0.5000 | 0.5000 | 0.5000 | 0.5000 | 0.4966 | 0.4966 | 0.4628 | 0.4628 | 0.0040 | 0.0000 | 0.0014 | 0.0014 | 0.0008 | 0.0008 | 0.0001 | 0.0000 | 0.0000 | 0.0000 |
| Vpi2q | 0.5000 | 0.5000 | 0.5000 | 0.5000 | 0.5031 | 0.5031 | 0.4581 | 0.4581 | 0.0007 | 0.0000 | 0.0034 | 0.0034 | 0.0018 | 0.0018 | 0.0000 | 0.0000 | 0.0000 | 0.0000 |
| Ipid | 1.0000 | 1.0000 | 1.0000 | 1.0000 | 0.0001 | 0.0001 | 0.0001 | 0.0001 | 0.0000 | 0.0000 | 0.0000 | 0.0000 | 0.0000 | 0.0000 | 0.0000 | 0.0000 | 0.0000 | 0.0000 |
| Ipiq | 1.0000 | 1.0000 | 1.0000 | 1.0000 | 0.0001 | 0.0001 | 0.0001 | 0.0001 | 0.0000 | 0.0000 | 0.0000 | 0.0000 | 0.0000 | 0.0000 | 0.0000 | 0.0000 | 0.0000 | 0.0000 |
| Vpi1d | 0.5001 | 0.5001 | 0.5001 | 0.5001 | 0.4961 | 0.4961 | 0.4620 | 0.4620 | 0.0042 | 0.0000 | 0.0013 | 0.0013 | 0.0006 | 0.0006 | 0.0000 | 0.0000 | 0.0000 | 0.0000 |
| Vpi1q | 0.5001 | 0.5001 | 0.5001 | 0.5001 | 0.5024 | 0.5024 | 0.4569 | 0.4569 | 0.0007 | 0.0000 | 0.0033 | 0.0033 | 0.0015 | 0.0015 | 0.0001 | 0.0000 | 0.0000 | 0.0000 |
| Id_TH | 0.0001 | 0.0001 | 0.0001 | 0.0001 | 0.9931 | 0.9931 | 1.0000 | 1.0000 | 0.0021 | 0.0000 | 0.0336 | 0.0336 | 0.0027 | 0.0027 | 0.0016 | 0.0003 | 0.0001 | 0.0000 |
| Iq_TH | 0.0001 | 0.0001 | 0.0001 | 0.0001 | 1.0000 | 1.0000 | 0.9303 | 0.9303 | 0.0029 | 0.0000 | 0.0084 | 0.0084 | 0.0136 | 0.0136 | 0.0004 | 0.0001 | 0.0000 | 0.0000 |

Figure 61: **GFOL participation factor at $\tau_p$ and $\tau_Q$=0.1**

### 7.2.2 Stability analysis of GFOL under different $\tau_p$ and $\tau_Q$

The effect of different control parameters on the stability of the system is observed by varying the control parameters and conclusions are drawn accordingly. The effect of the P, Q control module on the system stability was observed by varying the $\tau_p$ and $\tau_Q$. Table 9 shows the real, imaginary, frequency, and damping ratios for the different modes at different $\tau_p$ and $\tau_Q$. The stability of the modes increases as the color deepens.

**Mode 1-4:** As can be seen from cluster 1 in Fig. 62(a), the change in $\tau_p$ and $\tau_Q$ has little effect on modes 1-4 and they remain in their locations.

**Mode 5-6:** As can be seen from H in Fig. 62(h), the change in $\tau_p$ and $\tau_Q$ has little effect on modes 5-6 and they remain in their locations. Since modes 5 and 6 are conjugate, only the state of mode 5 is enlarged in the diagram to observe its stability state.

**Mode 7-8:** As can be seen from F in Fig. 62(h), the change in $\tau_p$ and $\tau_Q$ has little effect on modes 7-8. Modes 7 and 8 are conjugate, and as $\tau_p$ and $\tau_Q$ increase, they get closer and closer to the origin.

**Mode9:** As can be seen from A in Fig. 62(d), the change in $\tau_p$ and $\tau_Q$ has little effect on modes 9. Mode 9 has a damping ratio of 1 and an oscillatory frequency of 0. It shows no oscillatory behavior.

**Mode 10:** As can be seen in Fig. 62(e), the change in $\tau_p$ and $\tau_Q$ has little effect on mode 10. Mode 10 has a damping ratio of 1 and an oscillation frequency of 0. It exhibits no oscillatory behavior.

**Mode 11-12:** The movement of modes 11-12 can be seen at G in Fig. 62(h). The real part of these two modes is getting increasingly smaller and therefore further away from the origin.

**Mode 13-14:** The movement of modes 13-14 can be seen at D in Fig. 62(g). The real part of these two modes is getting larger and larger, so these 2 modes are getting closer and closer to the origin.

**Mode 15:** The movement of mode 15 can be seen at E in Fig. 62(g). The real part of these two modes is getting increasingly bigger and closer to the origin.

**Mode 16:**The motion of mode 16 can be seen at C in Fig. 62(g). The real part of the mode is getting larger and larger, so the mode is getting closer to the origin. Mode 16 has a damping ratio of 1 and an oscillation frequency of 0. It exhibits no oscillatory behavior.

**Mode 17-18:**The movement of modes 17-18 can be seen at I in Fig. 62(g). Changes in $\tau_p$ and $\tau_Q$ have almost no effect on the position of the modes.

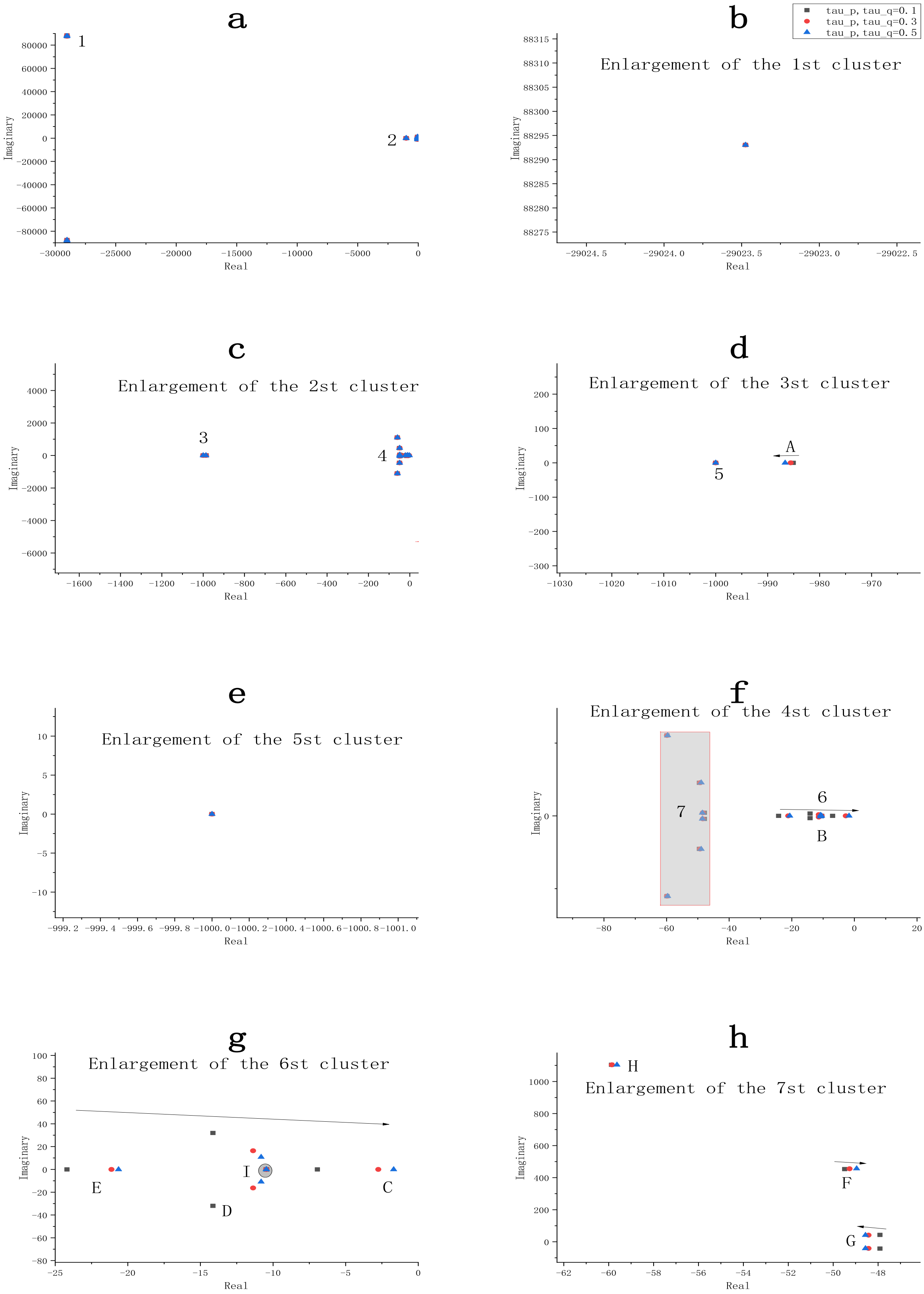

Figure 62: **GFOL modes with different $\tau_p$ and $\tau_Q$**

As can be noted from Fig. 63, the interaction between cita, $w_{input}$, and $KP_{droop}$ gradually weakens as $\tau_p$ increases.

According to 60 and 63, as $\tau_p$ increases, the proportionality coefficient $kp_P$, and the integration coefficient $ki_P$ of the power control module decrease, making the interactions between several state variables with mathematical relationships weaker.

However, as $\tau_q$ increases, there is always an interaction between the $KQ_{droop}$ and the input voltage $(V_{peak})$.In other words, there is an interaction within Group 6.

Moreover, it can be also seen that there is an interaction within Group 5 while changing the $\tau_p$ and $\tau_Q$. And this interaction is getting stronger as $\tau_p$ and $\tau_Q$ increase. As $\tau_p$ and $\tau_Q$ increase, the control effect of the P and Q controllers diminishes, making it less effective in controlling the variables in the power system, so the interactions between the state variables within the current controller become stronger.

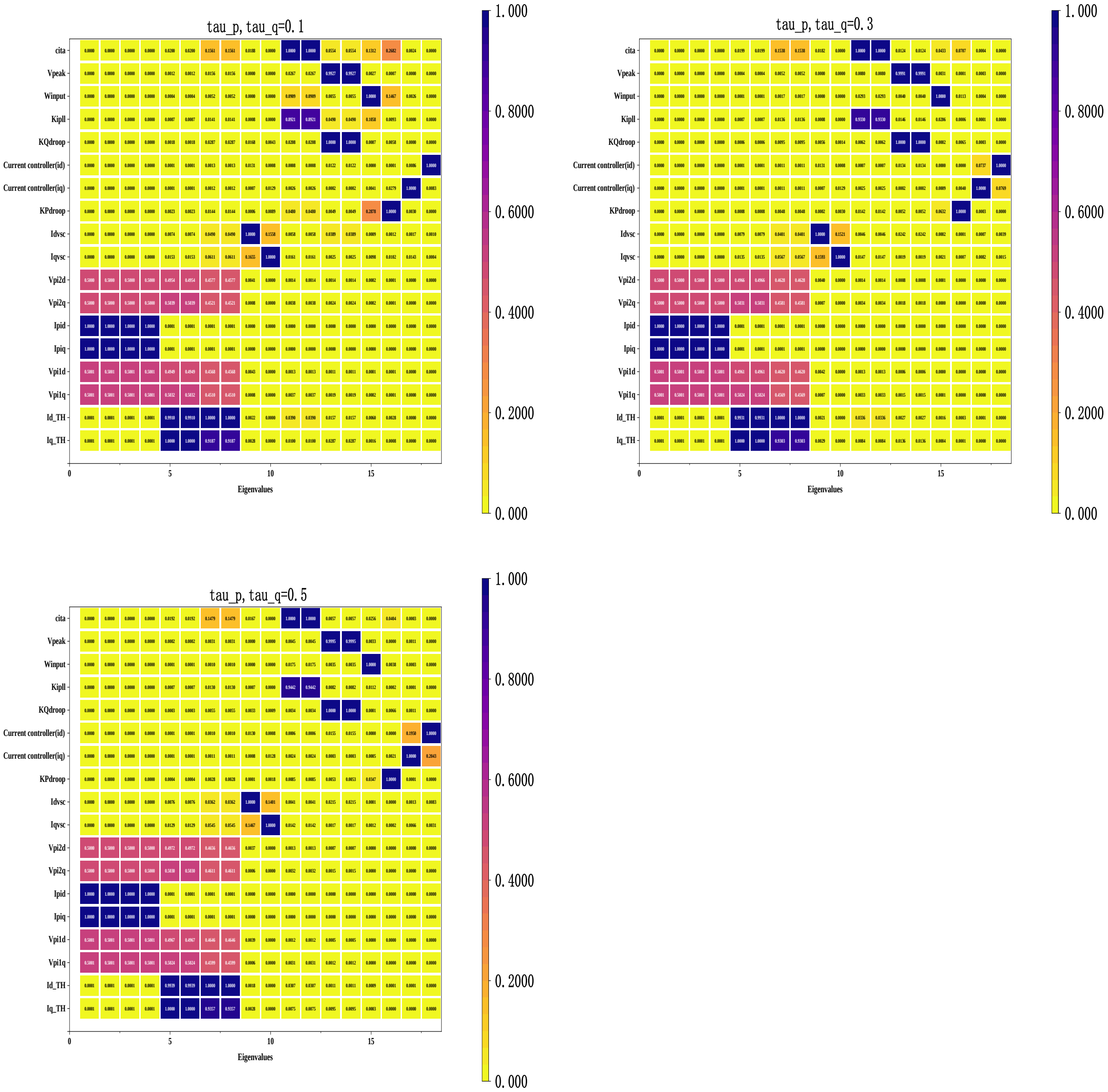

Figure 63: **GFOL participation factor at different $\tau_p$ and $\tau_Q$**

### 7.2.3 Stability analysis of GFOL under different XR

The X/R ratio is the amount of reactance X divided by the amount of resistance R, which also happens to be tangent to the angle created by the reactance and resistance in the circuit.

Table 10 shows the real, imaginary, frequency, and damping ratios for the different modes at different XR.

Table 10: Real, Imaginary, Frequency and Damping ratio with different XR

| | XR=1 | | | | XR=5 | | | | XR=10 | | | |
|---|---|---|---|---|---|---|---|---|---|---|---|---|
| | Real | Imaginary | Frequency | $\xi$ | Real | Imaginary | Frequency | $\xi$ | Real | Imaginary | Frequency | $\xi$ |
| 1 | -29022.76 | 88294.02 | 14052.43 | 0.90 | -29023.54 | 88292.94 | 14052.26 | 0.90 | -29023.57 | 88292.90 | 14052.25 | 0.90 |
| 2 | -29022.76 | -88294.02 | 14052.43 | 0.90 | -29023.54 | -88292.94 | 14052.26 | 0.90 | -29023.57 | -88292.90 | 14052.25 | 0.90 |
| 3 | -29022.76 | 87665.70 | 13952.43 | 0.90 | -29023.54 | 87664.62 | 13952.26 | 0.90 | -29023.57 | 87664.58 | 13952.25 | 0.90 |
| 4 | -29022.76 | -87665.70 | 13952.43 | 0.90 | -29023.54 | -87664.62 | 13952.26 | 0.90 | -29023.57 | -87664.58 | 13952.25 | 0.90 |
| 5 | -164.53 | 1219.32 | 194.06 | 0.65 | -38.75 | 1091.54 | 173.72 | 0.22 | -22.85 | 1085.91 | 172.83 | 0.13 |
| 6 | -164.53 | -1219.32 | 194.06 | 0.65 | -38.75 | -1091.54 | 173.72 | 0.22 | -22.85 | -1085.91 | 172.83 | 0.13 |
| 7 | -160.87 | 566.78 | 90.21 | 0.87 | -984.84 | 0.00 | 0.00 | 1.00 | -984.65 | 0.00 | 0.00 | 1.00 |
| 8 | -160.87 | -566.78 | 90.21 | 0.87 | -27.62 | 442.34 | 70.40 | 0.37 | -11.48 | 438.01 | 69.71 | 0.16 |
| 9 | -985.87 | 0.00 | 0.00 | 1.00 | -27.62 | -442.34 | 70.40 | 0.37 | -11.48 | -438.01 | 69.71 | 0.16 |
| 10 | -1000.00 | 0.00 | 0.00 | 1.00 | -1000.00 | 0.00 | 0.00 | 1.00 | -1000.00 | 0.00 | 0.00 | 1.00 |
| 11 | -43.43 | 38.60 | 6.14 | 0.99 | -48.81 | 43.42 | 6.91 | 0.99 | -49.36 | 43.75 | 6.96 | 0.99 |
| 12 | -43.43 | -38.60 | 6.14 | 0.99 | -48.81 | -43.42 | 6.91 | 0.99 | -49.36 | -43.75 | 6.96 | 0.99 |
| 13 | -13.44 | 30.90 | 4.92 | 0.94 | -14.17 | 31.78 | 5.06 | 0.94 | -14.15 | 31.48 | 5.01 | 0.94 |
| 14 | -13.44 | -30.90 | 4.92 | 0.94 | -14.17 | -31.78 | 5.06 | 0.94 | -14.15 | -31.48 | 5.01 | 0.94 |
| 15 | -25.00 | 0.00 | 0.00 | 1.00 | -24.13 | 0.00 | 0.00 | 1.00 | -24.12 | 0.00 | 0.00 | 1.00 |
| 16 | -6.77 | 0.00 | 0.00 | 1.00 | -6.94 | 0.00 | 0.00 | 1.00 | -6.92 | 0.00 | 0.00 | 1.00 |
| 17 | -10.42 | 0.00 | 0.00 | 1.00 | -10.44 | 0.00 | 0.00 | 1.00 | -10.44 | 0.00 | 0.00 | 1.00 |
| 18 | -10.47 | 0.00 | 0.00 | 1.00 | -10.47 | 0.00 | 0.00 | 1.00 | -10.47 | 0.00 | 0.00 | 1.00 |

As can be seen from Table 10, changes in XR have a greater effect on modes 8-9, with the real part of these two modes getting larger and the modes getting closer to the origin and changing by a greater amount. Among the other modes with a large change in position, as XR increases, modes 5 and 6 are getting closer to the origin.

### 7.2.4 Stability analysis of the GFOL under different closed-loop time constants of the current loop

It can be seen from Table 11 that the positions of modes 9 and 10 vary a lot with increasing $\tau$. Moreover, mode 9 doesn't show oscillatory behavior. Mode 10 has oscillation characteristics at $\tau$ of 7, it has a very low oscillation frequency and a very high damping ratio.

Modes 11 and 12 are complex conjugates at $\tau$ equal to 1 and 3, and modes 13 and 14 are also complex conjugates at $\tau$ equal to 1 and 3. However, when $\tau = 7$, modes 12 and 13 are no longer the complex conjugate poles of modes 11 and 14, respectively. Modes 12 and 13 become the new complex conjugate poles.

Table 11: Real, Imaginary, Frequency and Damping ratio under different closed-loop time constants of the current loop

| | $\tau$=1 | | | | $\tau$=3 | | | | $\tau$=7 | | | |
|---|---|---|---|---|---|---|---|---|---|---|---|---|
| | Real | Imaginary | Frequency | $\xi$ | Real | Imaginary | Frequency | $\xi$ | Real | Imaginary | Frequency | $\xi$ |
| 1 | -29023.5 | 88293.03 | 14052.27 | 0.90 | -29023.5 | 88293.03 | 14052.27 | 0.90 | -29023.5 | 88293.03 | 14052.27 | 0.90 |
| 2 | -29023.5 | -88293 | 14052.27 | 0.90 | -29023.5 | -88293 | 14052.27 | 0.90 | -29023.5 | -88293 | 14052.27 | 0.90 |
| 3 | -29023.5 | 87664.72 | 13952.27 | 0.90 | -29023.5 | 87664.72 | 13952.27 | 0.90 | -29023.5 | 87664.72 | 13952.27 | 0.90 |
| 4 | -29023.5 | -87664.7 | 13952.27 | 0.90 | -29023.5 | -87664.7 | 13952.27 | 0.90 | -29023.5 | -87664.7 | 13952.27 | 0.90 |
| 5 | -56.3365 | 1105.498 | 175.95 | 0.30 | -54.6389 | 1104.206 | 175.74 | 0.30 | -54.4026 | 1103.437 | 175.62 | 0.30 |
| 6 | -56.3365 | -1105.5 | 175.95 | 0.30 | -54.6389 | -1104.21 | 175.74 | 0.30 | -54.4026 | -1103.44 | 175.62 | 0.30 |
| 7 | -45.5994 | 466.0567 | 74.18 | 0.52 | -51.8099 | 465.1199 | 74.03 | 0.57 | -54.6641 | 467.9902 | 74.48 | 0.59 |
| 8 | -45.5994 | -466.057 | 74.18 | 0.52 | -51.8099 | -465.12 | 74.03 | 0.57 | -54.6641 | -467.99 | 74.48 | 0.59 |
| 9 | -1000.73 | 0 | 0.00 | 1.00 | -322.742 | 0 | 0.00 | 1.00 | -122.325 | 0 | 0.00 | 1.00 |
| 10 | -1000 | 0 | 0.00 | 1.00 | -333.333 | 0 | 0.00 | 1.00 | -51.1521 | 45.94565 | 7.31 | 0.99 |
| 11 | -47.5049 | 42.12352 | 6.70 | 0.99 | -48.6946 | 42.72723 | 6.80 | 0.99 | -51.1521 | -45.9457 | 7.31 | 0.99 |
| 12 | -47.5049 | -42.1235 | 6.70 | 0.99 | -48.6946 | -42.7272 | 6.80 | 0.99 | -13.4888 | 30.84728 | 4.91 | 0.94 |
| 13 | -13.4861 | 30.7605 | 4.90 | 0.94 | -13.4903 | 30.78867 | 4.90 | 0.94 | -13.4888 | -30.8473 | 4.91 | 0.94 |
| 14 | -13.4861 | -30.7605 | 4.90 | 0.94 | -13.4903 | -30.7887 | 4.90 | 0.94 | -24.0784 | 0 | 0.00 | 1.00 |
| 15 | -24.2476 | 0 | 0.00 | 1.00 | -24.1959 | 0 | 0.00 | 1.00 | -6.84289 | 0 | 0.00 | 1.00 |
| 16 | -6.78378 | 0 | 0.00 | 1.00 | -6.80239 | 0 | 0.00 | 1.00 | -10.253 | 0 | 0.00 | 1.00 |
| 17 | -10.4428 | 0 | 0.00 | 1.00 | -10.3825 | 0 | 0.00 | 1.00 | -142.857 | 0 | 0.00 | 1.00 |
| 18 | -10.472 | 0 | 0.00 | 1.00 | -10.472 | 0 | 0.00 | 1.00 | -10.472 | 0 | 0.00 | 1.00 |

# Conclusions

This paper introduced and analyzed the GFOL and GFOR systems with droop control, encompassing their components, modeling, and an active/reactive power control scheme based on instantaneous power theory.

The simulation results provided evidence of the scheme's feasibility. The development and validation of state-space equation models for GFOL and GFOR using small-signal analysis yielded promising results, confirming the correctness of the models. Theoretical analysis and simulations affirmed the accuracy and effectiveness of the state-space model in addressing transient system responses, further validating its correctness.

The analysis of the GFOR system reveals its ability to maintain system stability under both high and low SCR conditions. Moreover, it is evident that the GFOR system's relative stability improves with increasing kpP, while the relative stability of the GFOL system remains relatively unaffected by variations in $\tau_p$ and $\tau_Q$. Furthermore, the relative stability of the GFOR system diminishes with higher time constants in the current loop and XR values. Similarly, an increase in XR leads to reduced relative stability in the GFOL system. Two state variables with a mathematical computational relationship will have a large participation factor for some of the same modes, such as cita and $K_{Pdroop}$ of the GFOR system both have big PF with modes 15 and 16.

Conclusively, this research contributes to the advancement of state-space modeling, enhances understanding of system limitations, aids model refinement, and improves decision-making across various fields.

# Economics and environmental impact of the project

## • Economics

Table 12: Cost of the project

| **Concept** | **Cost Type** | **Unit** | **Cost (€)** |
|---|---|---|---|
| **University PC** | **Hardware** | **1** | **1250** |
| **Matlab** | **Software** | **1 Year** | **229** |
| **Writing** | **Human Rescource** | **120 Hours** | **3600** |
| **Project preliminary work** | **Human Rescource** | **100 Hours** | **3000** |
| **Building the code** | **Human Rescource** | **230 Hours** | **6900** |
| **Building the Matlab model** | **Human Rescource** | **60 Hours** | **1800** |
| **Scenarios and validation** | **Human Rescource** | **110 Hours** | **3300** |
| **Total** | | | **20079** |

Table 12 indicates the total cost of the project. Taking into account the cost of all hardware, software, and human resources, the total cost of this thesis is €20079.

## • Environmental Impact

In this paper, for environmental impact, a "cradle-to-gate" approach is used, which considers the entire production process of a product from raw material to arrive at the end user. In addition, the OpenLCA software was used to carry out an environmental impact assessment. For this purpose, the program has been divided into three parts: total electricity consumption, laptops, and desktops. Firstly, the necessary data has been collected for laptops and desktops as well as for production locations. Since it is difficult to reach an accurate data set, some estimates have been made of this information.

Firstly, the materials were investigated to find the total weight of the product. As OpenLCA requires transport data in t*km, the distances between Spain and Beijing for laptops and desktops were considered. Air transport was considered and entered into OpenLCA.

Table 13: Cost of the project

| Parameter | Laptop | Electrical Usage | Desktop | Unit |
|---|---|---|---|---|
| SOx | 0.508137469 | 0.00098 | 0.179 | kg |
| Nox | 0.493815433 | 0.005646 | 1.879 | kg |
| CO2 | 28.54793855 | 1.8228 | 257.180 | kg |
| CH4 | 0.413236465 | 0.0069 | 0.356 | kg |
| Total | | 0.91781 | 259.594 | kg |

Table 13 includes emissions that are harmful to the environment during the completion of this thesis. Emissions from the production process of laptops and desktops are considered, as well as emissions from the power consumption process of both.

## Gender Equality Analysis

The elimination of all discrimination against women and girls is not only a fundamental human right but is essential for a sustainable future; the empowerment of women and girls has been shown to contribute to economic growth and development. Empowering women with equal rights to land and property, sexual and reproductive health, and technology and the internet is essential.

This paper was completed independently by me under the guidance of my supervisor and this project has no gender implication. The references, software used, and internet sources consulted during the writing process of this paper do not contain any content that promotes gender discrimination. The stance of this paper is in support of ending all forms of discrimination against women and girls worldwide.

# Acknowledgement

I would like to take this opportunity to express my gratitude to those who made this project possible. My director, Eduardo Prieto Araujo, and my co-director, Onur Alican, have provided me with much help and ongoing support. Your help and continued support have been crucial to the completion of this project. Thank you for all your advice and encouragement throughout the project and for answering my many questions.

I would like to thank my EIT supervisor, Hans Edin, for granting me the scholarship that allowed me to meet so many interesting people and have such incredible moments over the past two years.

I also want to express my gratitude to every classmate in the SENSE project: Daniel, DQ, Berenice, Titouan, Kefan, Ao, Silivia, Manu, Aishwarya, Tim, and Punit. To me, SENSE feels like a big family where we have created numerous beautiful memories together. These memories will be treasures for me throughout my life. We have shared many adventures that I had never experienced before, and I thank all of you for making my two years of studying abroad so amazing. Although we will be on different sides of the world, there will always be a special place in my heart for each and every person of SENSE.

Finally, I would like to thank CITCEA and its personnel for welcoming me and providing me with the opportunity to carry out this project. Thank you all!

# Bibliografia

[1] G. Denis, T. Prevost, M.-S. Debry, F. Xavier, X. Guillaud, and A. Menze, "The migrate project: the challenges of operating a transmission grid with only inverter-based generation. a grid-forming control improvement with transient current-limiting control," *IET Renewable Power Generation*, vol. 12, no. 5, pp. 523–529, 2018.

[2] P. S. Kundur and O. P. Malik, *Power system stability and control*. McGraw-Hill Education, 2022.

[3] P. T. Green, "Is "grid forming" enough: what do electricity grids need from ibr?" 2021.

[4] A. Egea-Alvarez, A. Junyent-Ferré, and O. Gomis-Bellmunt, "Active and reactive power control of grid connected distributed generation systems," *Modeling and Control of Sustainable Power Systems: Towards Smarter and Greener Electric Grids*, pp. 47–81, 2012.

[5] S. Singh, M. Singh, and S. Kaushik, "A review on optimization techniques for sizing of solar-wind hybrid energy systems," *International Journal of Green Energy*, vol. 13, no. 15, pp. 1564–1578, 2016.

[6] G. Venkataramanan and C. Marnay, "A larger role for microgrids," *IEEE Power and Energy Magazine*, vol. 6, no. 3, pp. 78–82, 2008.

[7] F. V. P. Robinson, "Power electronics converters, applications and design: Ned mohan, tore m. undeland and william p. robbins (2nd edition), john wiley, chichester, 1995, 802 pp., isbn: 0-471-30576-6, £22.50," *Microelectronics Journal*, vol. 28, pp. 105–106, 1997.

[8] F. Sadeque and B. Mirafzal, "A universal controller for grid-forming inverters in microgrid during islanding for low transient current," in *2022 1st IEEE International Conference on Industrial Electronics: Developments Applications (ICIDeA)*, 2022, pp. 62–67.

[9] S. Geng and I. A. Hiskens, "Unified grid-forming/following inverter control," *IEEE Open Access Journal of Power and Energy*, vol. 9, pp. 489–500, 2022.

[10] A. C. Z. de Souza and M. Castilla, *Microgrids design and implementation*. Springer, 2019.

[11] J. M. Guerrero, P. C. Loh, T.-L. Lee, and M. Chandorkar, "Advanced control architectures for intelligent microgrids—part ii: Power quality, energy storage, and ac/dc microgrids," *IEEE Transactions on industrial electronics*, vol. 60, no. 4, pp. 1263–1270, 2012.

[12] B. Wen, D. Boroyevich, R. Burgos, P. Mattavelli, and Z. Shen, "Analysis of d-q small-signal impedance of grid-tied inverters," *IEEE Transactions on Power Electronics*, vol. 31, no. 1, pp. 675–687, 2016.

[13] P. Kundur, J. Paserba, V. Ajjarapu, G. Andersson, A. Bose, C. Canizares, N. Hatziargyriou, D. Hill, A. Stankovic, C. Taylor, T. Van Cutsem, and V. Vittal, "Definition and classification of power system stability ieee/cigre joint task force on stability terms and definitions," *IEEE Transactions on Power Systems*, vol. 19, no. 3, pp. 1387–1401, 2004.

[14] R. Newell, D. Raimi, S. Villanueva, B. Prest *et al.*, "Global energy outlook 2021: pathways from paris," *Resources for the Future*, vol. 8, 2021.

[15] L. Bird, M. Milligan, and D. Lew, "Integrating variable renewable energy: Challenges and solutions," National Renewable Energy Lab.(NREL), Golden, CO (United States), Tech. Rep., 2013.

[16] A. Hoke, V. Gevorgian, S. Shah, P. Koralewicz, R. W. Kenyon, and B. Kroposki, "Island power systems with high levels of inverter-based resources: Stability and reliability challenges," *IEEE Electrification Magazine*, vol. 9, no. 1, pp. 74–91, 2021.

[17] J. Matevosyan, J. MacDowell, N. Miller, B. Badrzadeh, D. Ramasubramanian, A. Isaacs, R. Quint, E. Quitmann, R. Pfeiffer, H. Urdal *et al.*, "A future with inverter-based resources: Finding strength from traditional weakness," *IEEE Power and Energy Magazine*, vol. 19, no. 6, pp. 18–28, 2021.

[18] J. Z. Zhou, H. Ding, S. Fan, Y. Zhang, and A. M. Gole, "Impact of short-circuit ratio and phase-locked-loop parameters on the small-signal behavior<? pub _bookmark="" command="[quick mark]"?> of a vsc-hvdc converter," *IEEE Transactions on Power Delivery*, vol. 29, no. 5, pp. 2287–2296, 2014.

[19] D. Pattabiraman, R. Lasseter, and T. Jahns, "Comparison of grid following and grid forming control for a high inverter penetration power system," in *2018 IEEE Power & Energy Society General Meeting (PESGM)*. IEEE, 2018, pp. 1–5.

[20] J. Rocabert, A. Luna, F. Blaabjerg, and P. Rodriguez, "Control of power converters in ac microgrids," *IEEE transactions on power electronics*, vol. 27, no. 11, pp. 4734–4749, 2012.

[21] S. D'Arco and J. A. Suul, "Equivalence of virtual synchronous machines and frequency-droops for converter-based microgrids," *IEEE Transactions on Smart Grid*, vol. 5, no. 1, pp. 394–395, 2013.

[22] M. S. Annakkage, C. Karawita, and U. D. Annakkage, "Frequency scan-based screening method for device dependent sub-synchronous oscillations," *IEEE Transactions on Power Systems*, vol. 31, no. 3, pp. 1872–1878, 2016.

[23] C. Collados-Rodriguez, M. Cheah-Mane, E. Prieto-Araujo, and O. Gomis-Bellmunt, "Stability analysis of systems with high vsc penetration: Where is the limit?" *IEEE Transactions on Power Delivery*, vol. 35, no. 4, pp. 2021–2031, 2020.

[24] M. Cheah-Mane, A. Egea-Alvarez, E. Prieto-Araujo, H. Mehrjerdi, O. Gomis-Bellmunt, and L. Xu, "Modeling and analysis approaches for small-signal stability assessment of power-electronic-dominated systems," *Wiley Interdisciplinary Reviews: Energy and Environment*, vol. 12, no. 1, p. e453, 2023.

[25] R. Roesser, "A discrete state-space model for linear image processing," *IEEE transactions on automatic control*, vol. 20, no. 1, pp. 1–10, 1975.

[26] R. H. Park, "Two-reaction theory of synchronous machines generalized method of analysis-part i," *Transactions of the American Institute of Electrical Engineers*, vol. 48, no. 3, pp. 716–727, 1929.

[27] Z. Cheng, J. Duan, and M.-Y. Chow, "To centralize or to distribute: That is the question:

A comparison of advanced microgrid management systems," *IEEE Industrial Electronics Magazine*, vol. 12, no. 1, pp. 6–24, 2018.

[28] J. Miret, J. L. García de Vicuña, R. Guzmán, A. Camacho, and M. Moradi Ghahderijani, "A flexible experimental laboratory for distributed generation networks based on power inverters," *Energies*, vol. 10, no. 10, p. 1589, 2017.

[29] A. Tuladhar, H. Jin, T. Unger, and K. Mauch, "Parallel operation of single phase inverter modules with no control interconnections," in *Proceedings of APEC 97-Applied Power Electronics Conference*, vol. 1. IEEE, 1997, pp. 94–100.

[30] D. B. Rathnayake, M. Akrami, C. Phurailatpam, S. P. Me, S. Hadavi, G. Jayasinghe, S. Zabihi, and B. Bahrani, "Grid forming inverter modeling, control, and applications," *IEEE Access*, vol. 9, pp. 114 781–114 807, 2021.

[31] Y. A.-R. I. Mohamed and E. F. El-Saadany, "Adaptive decentralized droop controller to preserve power sharing stability of paralleled inverters in distributed generation microgrids," *IEEE Transactions on Power Electronics*, vol. 23, no. 6, pp. 2806–2816, 2008.

[32] C. Collados-Rodriguez, M. Cheah-Mane, E. Prieto-Araujo, and O. Gomis-Bellmunt, "Stability analysis of systems with high vsc penetration: Where is the limit?" *IEEE Transactions on Power Delivery*, vol. 35, no. 4, pp. 2021–2031, 2019.

[33] X. Gao, D. Zhou, A. Anvari-Moghaddam, and F. Blaabjerg, "Stability analysis of grid-following and grid-forming converters based on state-space model," in *2022 International Power Electronics Conference (IPEC-Himeji 2022-ECCE Asia)*. IEEE, 2022, pp. 422–428.